Faculty of Science and Engineering
Department of Petroleum Engineering

Designing Laminate Composites to House Electronic Sensors for Drill Pipe Applications

Ben Ameri

This thesis is presented for the Degree of
Doctor of Philosophy
of
Curtin University

November 2016

Declaration

To the best of my knowledge and belief this thesis contains no material previously published by any other person except where due acknowledgment has been made.

This thesis contains no material which has been accepted for the award of any other degree or diploma in any university.

Signature: 

Date: 28,11,2016

Abstract

Drilling operations, for both mining and oil and gas industries, require the use of electronic systems for borehole logging. Ideally, if the logging were performed while drilling, by embedding the electronics in the drill pipe, the logging operation would be more efficient and cost-effective. Physical properties and the weight of steel drill pipe have vital roles on such activities. By contrast, composite materials have advantages over conventional steel drill pipes. Composite materials are known for their high mechanical properties, strength while being lighter in weight. Filament winding composites consist of multiple layers of fibres layered at different angles of orientation to achieve specific mechanical properties. The knowledge of the fibre orientation and number of layers are not pre-set. In this thesis, optimising the type of composite and method of fabrication are addressed to develop a smart composite drill pipe with embedded sensors for mineral exploration applications.

Composite material properties are a function of the number of laminated layers and their orientation, which are based on the loading direction application. Numerical simulation and experimental work were performed to understand the stress distribution on each of the laminate layers and the overall strength of different composite structural design, with and without an embedded sensor. Five different symmetric multi-angled laminated lay-ups were evaluated using eight plies. The laminate angles $[(\pm 75)_C/(\pm 10)_{FG}]_S$ maintained the higher Margin of Safety (MoS) values, compared to other evaluated laminate design angles. Finite element analysis (FEA) simulation runs were applied on hybrid composite flat laminates with and without an embedded sensor/circuit board (CB). The numerical study was extended to a tube geometry to simulate drill pipe. The tube geometry was then converted to a flat geometry and the results of both models were compared to demonstrate that the flat geometry model could represent the tube geometry under similar conditions.

Experiments were then done involving tensile testing of carbon-glass/epoxy (hybrid composite) flat specimens with and without the CB to validate the FEA results. The numerical modelling showed good agreement with the experiments. The CB was embedded into the hybrid composites with minimal deterioration of

the composite's structural strength.

The relationship between the size of an embedded circuit board and the host material was numerically evaluated, using the ratio of the CB area to the area of the host material (area sensitivity). The effect of thickness variation of the embedded CB within the hybrid composite (thickness sensitivity) was also addressed. The results of stress and failure analysis indicated that the area of the CB does not affect the strength of the host material, however the thickness of the CB does have a tangible effect on the strength of the host material.

This research demonstrated through technical evaluation and testing, that there is an optimum material and fabrication method that if considered during filament winding of electronic sensors housed within drill pipes, the sensor efficiency and the housing composite material strength will not be compromised. This research thesis provides a unique design and material selection analysis that meets the challenges of the composite filament winding process with embedded electronic components for future 'smart' composite drill pipes, for borehole logging operations.

Acknowledgements

Firstly, I would like to express my sincere gratitude to my thesis committee: my advisor Dr. Reem Roufail, for the continuous support of my PhD study and related research, for her patience, motivation, and immense knowledge. Her feedback helped me all the time of research and writing of this thesis. My sincere thanks also goes to Professor Brian Evans, Faculty director of oil and gas Initiatives at Department of Petroleum Engineering, Curtin University for his fruitful comments and his precious help in correcting this manuscript. I also express my acknowledgement of Professor Vamegh Rasouli, now the Department Chair at the Department of Petroleum Engineering, University of North Dakota, USA who provided me with this opportunity as a PhD candidate with all his support. I am also very much indebted to Gordon Stewart, marketing director at Globaltech Corporation Pty Ltd, for giving me an opportunity to develop my professional career as a Materials Scientist, and his valuable guidance.

I would like to thank all my colleagues at Globaltech Corporation Pty Ltd, especially Brett Wilkinson and Raymond Hill for their generous advise and cooperation. I am grateful to Dr Philip Teakle Director of Teakle Composites Australia Pty for providing composite materials and equipment.

I am grateful to Robert Cutter and Dr Arne Bredin at the Civil Engineering department, Curtin University, who provided me with their laboratory testing facilities. I am greatly thankful to my colleagues at the Department of Petroleum Engineering, particularly, Christopher Kipchumba Lagat and Siamak Mishani for their support.

My thanks to all whose names I do not know or have failed to mention for their support.

Last but not the least, I would like to thank my family, my brother Dr Omid Ameri and I can never thank enough Irene Nykrem for being so supportive, understanding and patient during the whole time of my thesis.

The work has been supported by the Deep Exploration Technologies Cooperative Research Centre whose activities are funded by the Australian Government's Cooperative Research Centre Programme. This is DET CRC Document 2016/913.

To

My family

Contents

List of Figures

List of Tables

Nomenclature

MoS/MS	Margin of safety
FEA	Finite element analysis
CB	Circuit board
LWD	Logging-while-drilling
MWD	Measurement-while-drilling
RC	Reversed circulation
IR	Infra-red
CAE	computer-aided engineering
ACP	ANSYS Composite ‘PrepPost’
CMP	Condition Monitoring Pad
PMCs	Polymer matrix composites
MMCs	Metal matrix composites
CMCs	Ceramic matrix composites
CCCs	Carbon/carbon composites
V_f	Fibre volume fraction
E_1	Longitudinal modulus
E_2	Transverse modulus
G_{12}	In-plane shear modulus
υ_{12}	Major Poisson's ratio
υ_{23}	Through thickness Poisson's ratio

X_T	Longitudinal tensile strength
X_c	Longitudinal compressive strength
Y_T	Transverse tensile strength
Y_c	Transverse compressive strength
S_{12}	In-plane shear strength
ε_{1T}	Longitudinal tensile failure strain
ε_{1C}	Longitudinal compressive failure strain
ε_{2T}	Transverse tensile failure strain
ε_{2C}	Transverse compressive failure strain
γ_{12u}	In-plane shear failure strain
G_{IC}	Strain energy release rate
α_1	Longitudinal thermal coefficient
α_2	Transverse thermal coefficient
FWC	Filament-wound composites
FG	Fiberglass
C	Carbon
CLT	Classical Laminate Theory
N	Force resultant
M	Bending moment resultant
σ	Stress
τ	Shear stress

k	Curvature
LSS	Laminate stacking sequence
RF	Reserve factor
IRF	Inverse reserve factor
F	Force
A	Area

1 INTRODUCTION

1.1 Background

While the use of composites has increased dramatically over recent years (particularly in the aviation industry for the wings of aeroplanes), the cost and performance of composite structures has kept them from being widely used. Confidence in using composite materials has increased significantly in the marine, military, aerospace as well as the oil and gas industry more recently as composites offer mechanical properties competitive to steel, at less than half the weight (James, 2011). Composites have excellent resistance to chemicals and corrosion, low mass and cost, they can be manufactured with a complex shape and the ability to embed electronics within the material.

The Deep Exploration Technologies Cooperative Research Centre (DET CRC) was established in 2010 under the Australian Government's CRC program. "The CRC program for mineral exploration provides funding to build critical mass in research ventures between end users and researchers to deliver significant economic, environmental and social benefits across Australia" (CRC, 2010). DET CRC, as a component of its research, undertook the world's first mineral exploration drilling research program using composite drill rods. Figure 1-1 shows different composite rods (using fibre glass and carbon fibre) which are less than half the weight of conventional rods but with greater strength. Composite drill rods offer better occupational health and safety (OH&S), easier carriage to remote locations, smaller rigs (less hoisting issues) and lower consumable requirements as well as sensors that can be embedded in composite rods for real-time data transmission up the rods to the surface of exploration holes (CRC, 2013). This PhD study was focussed on investigating the mechanical aspects resulting in changes in material properties when embedding a sensor into composite drill rods for logging-while-drilling purposes.

Figure 1-1: Composite drill rods (CRC, 2010)

Composites can offer reduced maintenance, they enhance on safety because of less weight, save weight on structures and pipes and have good electrical and thermal insulation properties. For example, various electrical sensors could be integrated into the composite structure to deliver data from remote or downhole locations. Smart structures can be formed with sensors embedded in the material or bonded to the surface. Piezoelectric transducers, strain gauges, optical fibres and acoustic wave sensors make up the most common sensors in smart composite structures. However, the focus of this Ph.D. thesis is on embedding an electrical circuit board (CB) within a composite structure and observing its effect. As the mechanical properties and fabrication of the composites can be modified to provide the desired mechanical response required to maintain the sensors intact, these materials are well suited to the concept of embedded components. Due to the low temperatures and pressures needed to make the composites, the embedding of fragile sensors will not affect the sensor's ability to operate well, so the embedding approach can be robust and realistic (Baker et al., 2004).

Two ways are feasible to embed a sensor into a composite material. Some researchers such as Moulin et al. (1997), Hagood et al. (1989) and Warkentin et

al. (1991) cut the composite plies surrounding the embedded sensor. Others such as Shen et al. (1996) and Bourasseau et al. (1996) along with this study, embedded the sensor directly into composite layers to avoid cutting the fibre .

Logging-while-drilling (LWD) or measurement-while-drilling (MWD) and directional drilling have important roles in the process of drilling rock. A vital feature of composite drill rods is that they can be built of fibre layers between which power and/or real time communications can be carried through lines embedded between the composite walls, where sensitive electrical and data transmission is a significant requirement for success. In fact, a multi-function drill pipe can be achieved by embedding electronics into the composite pipe that causes significant savings in cost and time to the drilling operation. This type of performance rating often exceeds the overall capabilities of conventional materials such as thermosets, aluminium and steel.

1.2 Application of an embedded sensor within a composite drill rod

After the initial successful testing of a composite drill rod manufactured by an industry partner of the DET CRC (Figure 1-2), that project then reviewed embedding the sensors into the composite layers of the drill rod. In this research, the primary application of the embedded sensor/circuit board within the composite material was for downhole surveying of any drill hole, to monitor the drill hole position and direction (bore-hole path) at specific intervals during the drilling operation. As drilling activities are one of the most expensive costs in mineral exploration, so it is vital to gather as much geological information as possible from each borehole to avoid both drilling risks and any additional costs that may occur such as drilling offset holes where they may not be needed (if adequate geological strata information had been gathered in the first place).

Figure 1-2: Drilling action with a composite carbon fibre rod (CRC, 2013)

Downhole surveying is mainly used by exploration drilling to confirm or define the actual drill-hole path and identify the exact original position of core samples extracted from exploration drill-holes. It's a process designed to determine, which minerals are present at the subsurface site, the grade and quality of the minerals, exact location and shape of any discovered ore body. Also, in order to facilitate, feasibility study of a site for mine development and overall planning of a mining project.

Drilling achieves extraction of core samples for analysis. Surveying achieves positioning of these samples to determine size, shape and position of the target. It is therefore often economically unfeasible to achieve these objectives of exploration drilling without surveying (Globaltech, 2009).

Single-shot surveying and *multi-shot* surveying are two common ways of surveying in exploration drilling. Single-shot surveying is typically conducted by the driller while drilling a hole to give the driller an indication that the correct drill path is being followed. The driller stops the drilling process at certain intervals (normally 30m when the drill bit comprises of diamonds known as 'diamond drilling' and at 50m for reversed circulation drilling known as 'RC drilling') and

inserts the survey tool to obtain the hole azimuth (compass angle) and dip (inclination from horizontal) at that depth. These measurements are necessary to correct any hole deviation that may have occurred. Multi-shot surveying is typically done by a surveyor after the hole is completed, normally in intervals of 10m (depending on the straightness of the hole) where the intervals may vary from 2m to 15m. In most cases after completion of the hole, the drillers case the holes as they take the drill rods out so that the surveyor can come at a later stage and perform the multi-shot survey (Globaltech, 2009).

For example, one of the advanced pieces of digital equipment used in wireline surveys is the Pathfinder® which is manufactured by Globaltech Corporation Pty in Australia. Pathfinder® parts include brass housing tubes, an electronic module, a battery module and a handheld (data receiver device). The brass housing tubes protect the electronic and battery modules from mechanical loading such as vibration and shock. The electronic module is an electronic circuit board which includes temperature, magnetometer and accelerometer sensors which measure the depth, downhole temperature and direction of any magnetic and gravity fields. The battery module provides the power for the electronics. The handheld device receives the survey data by infer-red communication from the Pathfinder®. It has a USB port which allows transferring the data to a USB memory stick.

Figure 1-3: Details of Pathfinder® parts (Limited, 2015)

Figure 1-3 shows the parts of a Pathfinder®, in which the data is retrieved from downhole to surface and sent to the handheld device via an infra-red (IR) port.

One of the objectives of this study was to embed a thin circuit board (CB) within a composite material which could have electronic functions with a CB that would be similar to the downhole surveying equipment. Some advantages of embedding such sensors into a composite drill rod compared with conventional surveying

tools are as follows:

- There is no concern about any magnetic interference caused by the drilling equipment such as the bit, rod string or landing collar since it is very important to use non-magnetic materials around the sensors in a surveying tool.
- Saving time and cost of drilling because the electronics and the battery can be embedded permanently within the layers of the composite drill rod. Therefore, after completion of the hole when the rods are retrieved to the surface, the drillers will already have the data and they would not need to run the surveying tool, so it causes significant saving in time and cost. The efficiency of the drill crew would also increase as logging of the hole is performed in less time.
- The power for the electronics circuit board would be provided by an embedded rechargeable battery which could be charged using an inductive charger wirelessly, as an electromagnetic field can readily travel through composite layers.

A rechargeable Lithium Polymer battery can have a thickness of 420 micrometre as shown in Figure 1-4a. The electronic sensors can be placed on an ultra-thin circuit board having a thickness of 0.1mm (Figure 1-4b). However, the CB that was used in this research did not include the electronic components on the CB since the functions of the electronics were not related to the topic of the thesis. The physical and mechanical aspects of the CB such as stress concentrations in the host material, dimensions, and thickness variation were to be studied.

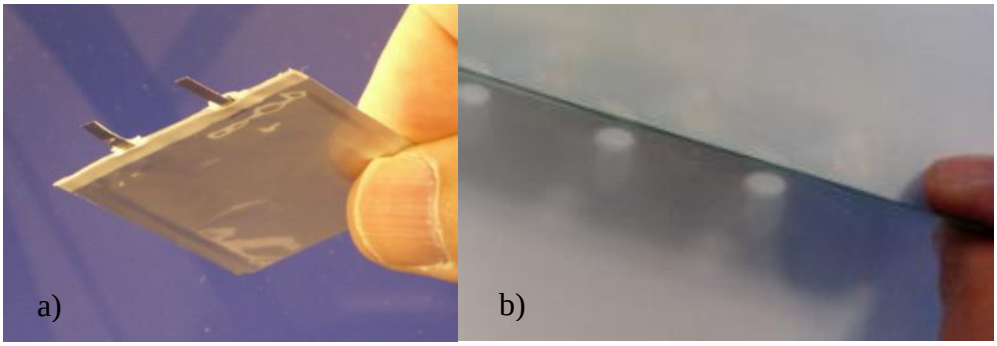

Figure 1-4: a) Ultrathin rechargeable Lithium Polymer Battery (Stream, 2016), b) Circuit board with 0.1mm thickness

1.3 Research objective

The focus of this research was on evaluation of stress concentration around an embedded circuit board (CB) within a hybrid laminated composite both experimentally and numerically. The thesis's aim was to achieve the following objectives:

- To improve mechanical and physical properties of the host material that can protect the embedded CB from the harsh external environment and fluid leakage during applications downhole.
- To create an optimum design (multi-angle fibres) to allow a laminated composite to host a CB.
- To compare the results of a flat laminated geometry with a tube geometry to allow modification of the methodology of CB placement. In other words, to investigate if the geometry shapes of the host material affect the CB or not under uniaxial tensile load.
- Attempt to minimise stress concentrations around any embedded CB at the interface between the CB and the host material, which would reduce fatigue on the embedded CB.

1.4 Thesis overview

To investigate and minimize the effect of stress concentrations around the embedded sensor within the composite material (host material), two research approaches were used – one was performing numerical simulations and the other was doing experimental tests to confirm the numerical modelling.

Chapter 2 is a literature review which will discuss the material selection and manufacturing methods of composite materials, the fundamental theories behind the composite design, the failure theories and the primary stress classification in composites.

To embed the sensor/circuit board within laminate composites, one optimum numerically modelled laminated design methodology was selected by using a computer-aided engineering (CAE) software package known as *HyperSizer*®. As explained in Chapter 3.

Chapter 4 presents the composite laminate analysis. The fabrication method for manufacturing composite drill rods is that of 'filament winding', which is not a manufacturing method that can easily produce test specimens - it is a difficult and complicated process not suited to research, especially at the laboratory scale. Therefore, this study was based on manufacturing in the lab a simple flat laminated specimen. In order to minimise the testing time and risk such as physical harm, cost and delay to the research, the Finite Element Analysis (FEA) method (ANSYS Composite 'PrepPost' software) was used. The first FEA model was based on a flat hybrid composite model with and without an embedded CB.

Then to validate the FEA analysis the experimental work was based on a relative comparison of hybrid laminate samples that had no CB versus a hybrid sample that had an embedded CB. The specimens were fabricated by the hand lay-up technique with the characteristic of a filament winding rhomboid pattern and subjected to a unidirectional tensile load in the lab.

The study then focused on numerical analysis. Two tube geometries were created with and without an embedded CB, assuming the same criteria used as those for the flat hybrid composite model. Similar analysis was then performed on the flat geometries with the same cross-sectional dimensions and laminate lay-up. Finally, the results of the tube and the flat geometry were compared.

Two sensitivity analyses were performed using the physical dimensions of the CB and the host material finalised in Chapter 5. The first sensitivity analysis was the area ratio of the CB to the area of the host material (area sensitivity). The second sensitivity analysis was the thickness variation effect of the embedded CB versus the host material (thickness sensitivity).

The final Chapter of the thesis (Chapter 6) reviews the research conclusions and recommendations.

A study has also been done on an analysis of fibre-glass/epoxy material as a host material, by numerical simulation and experimental work which is discussed in Appendix A. The purpose of the study was to confirm or otherwise, that the hybrid composite material has more strength over other types of composite materials.

Appendix B provides the details of the two Condition Monitoring Pads (CMP) which were developed and fabricated by me in addition to my PhD research.

2 LITERATURE REVIEW

This chapter explained the material selection, composite manufacturing methods which were used in the experimental work and the fundamental theories behind the composite design.

2.1 Material selection

2.1.1 Composite classification

A composite is considered to be a material consisting of two or more distinct phases, combined in a structural unit. The type of material used for the matrix classifies the composite. There are four primary categories of composites polymer matrix composites (PMCs), metal matrix composites (MMCs), ceramic matrix composites (CMCs), and carbon/carbon composites (CCCs) (Kutz, 2002). This study focuses on PMCs which is the most widely used class of composites.

2.1.2 Matrix materials

There are two major classes of polymers used as matrix materials: thermosets and thermoplastics. Thermosets are materials that undergo a curing process during part fabrication, after which they are rigid and cannot be reformed. Thermoplastics, on the other hand, can be repeatedly softened and reformed by the application of heat (Kutz, 2002).

Thermosets are more suitable for this research because of the vital advantages that they have over thermoplastics such as being relatively inexpensive, easy to process, and corrosion resistant. The key types of thermosetting resins used in composites are epoxies, bismaleimides, thermosetting polyimides, cyanate esters, thermosetting polyesters, vinyl esters, and phenolics (Zweben, 2007). Based on design requirements, as well as manufacturing and cost considerations, epoxies are considered as being preferred for this project as the composite material (Kutz, 2002).

Epoxies currently are the dominant resins used for low and moderate temperatures (up to 275 °F /135 °C), since they are the most common matrix material for high-performance composites and adhesives. They have an excellent combination of

strength, adhesion, low shrinkage, and processing versatility. Commercial epoxy matrices and adhesives can be as simple as one epoxy and one curing agent (Campbell, 2010).

The largest application for reinforced epoxy resins in laminate sheets, which is about 25% of the total of all epoxies produced, is electrical circuit boards. Epoxies are especially useful for these boards because of their inherent low conductivity and high dielectric strength. Also, epoxies have a low tendency to emit gases even when subjected to an electrical discharge. Many other thermoset resins emit gases from unreacted crosslinking agents/solvents or from unreacted monomers. Another advantage of epoxies in this application is their thermal stability which, although not among the highest of thermoset materials, is higher than polyester thermosets and most other low-cost thermosets that might compete with them in the electrical circuit board market. The relatively good thermal stability of epoxies, their excellent adhesive properties, and their good mechanical properties have led to their widespread use as the principal resin in most high-performance composites (chiefly those using carbon or graphite fibres as the reinforcement). The markets that most often use high-performance composites are aerospace, sporting goods, and medical devices (Strong, 2008).

Epoxies, the preferred resin for composites used in electrical applications, is best in terms of performance and cost. They have better electrical properties than the cheaper polyesters and are lower priced than the high-performance resins (Strong, 2008).

2.1.3 Reinforcement materials

The main types of reinforcements used in composite materials are aligned continuous fibres, discontinuous fibres, whiskers (elongated single crystals), particles, and numerous forms of fibrous architectures produced by textile technology, such as fabrics and braids (Zweben, 2006).

I focus on composites reinforced with continuous fibres because they are the most efficient structural materials as well as the most common reinforcement in filament winding and especially in high-performance applications. The most common fibre reinforcements for PMCs are fibre glass and carbon fibres.

Glass fibres are used primarily to reinforce polymers. The leading types of glass fibres for mechanical engineering applications are E-glass and high-strength S-glass. E-glass fibres, the first major composite reinforcement to be used, were originally developed for electrical insulation applications (Zweben, 2007). Due to their low cost and early development compared to other fibres, E-glass fibres are the most widely used of all fibrous reinforcements. They are often used as thermal and electrical insulators, the characteristics of which are of considerable interest in this thesis.

Carbon fibres are popular for properties such as high stiffness, strength, and low density. They have excellent resistance to creep, stress rupture, fatigue, and corrosive environments, although they oxidize at high temperatures. Some carbon fibres also have extremely high thermal conductivities—many times that of copper. This characteristic is of considerable interest in electronic packaging and other applications where thermal control is important (Kutz, 2002). Highly conductive carbon fibre surfaces produce an undesirable capacitance relative to sensors, electronics and cables (Hill, 2003). However, this characteristic conflicts with the use of embedded sensors. So to achieve more efficiency and to cover the electronics with non-conductive fibres like E-glass fibres which are suitable for that purpose, hybrid composites may be used that combine different types of reinforcements.

Hybrid composite is the incorporation of two or more reinforcements within a single matrix. A variety of reinforcing fibres and matrices are used to form hybrid composites. However this research focuses on carbon fibres and glass fibres in an epoxy resin matrix. Carbon fibres provide high strength, are stiff and are of low density reinforcement but are relatively expensive, while glass fibres are relatively cheap and have better fracture strain, fracture stress and are electronically friendly but lack stiffness (Summerscales & Short, 1978). By using E-glass fibres (to protect the electronic sensor within the composite material) and carbon fibres (to give better mechanical properties to the composite material), it is possible to design the material to suit particular requirements, especially where properties are required for this study.

2.1.4 Properties of composite materials

In this section, I discuss the mechanical and the physical properties of E-glass/epoxy and carbon/epoxy which was used in finite element analysis (FEA).

Composites are anisotropic material systems, their properties are affected by many variables such as their reinforcement form, volume fraction and geometry; properties of the interphase, the region where the reinforcement and matrix are joined (also called the interface); and void content. The process by which the composite is made affects many of these variables. The same matrix material and reinforcements when combined by different processes may result in composites with very different properties.

Another critical issue is that composite properties are sensitive to the test methods by which they are measured, and there are many different test methods used throughout the industry. Further, test results are very sensitive to the skill of the technician performing the test. Because of these factors, it is very common to find significant differences in reported properties of what may nominally be the same composite material (Kutz, 2002) .

Table 2-1 Mechanical and thermal properties of two selected unidirectional laminae (Soden, Hinton, & Kaddour, 1998)

Fibre type	T300	Silenka E-Glass 1200tex
Matrix	BSL914C epoxy	MY750/HY917/ DY063 epoxy
Specification	Filament winding	Filament winding
Manufacturer	DFVLR	DRA
Fibre volume fraction, V_f	0.6	0.6
Longitudinal modulus, E_1 (GPa)	138	45.6
Transverse modulus, E_2 (GPa)	11	16.2
In-plane shear modulus, G_{12} (GPa)	5.5	5.83
Major Poisson's ratio, υ_{12}	0.28	0.278
Through thickness Poisson's ratio, υ_{23}	0.4	0.4
Longitudinal tensile strength, X_T (MPa)	1500	1280
Longitudinal compressive strength, X_C (MPa)	900	800
Transverse tensile strength, Y_T (MPa)	27	40
Transverse compressive strength, Y_C (MPa)	200	145
In-plane shear strength, S_{12} (MPa)	80	73
Longitudinal tensile failure strain, ε_{1T} (%)	1.087	2.807
Longitudinal compressive failure strain ε_{1C} (%)	0.652	1.754
Transverse tensile failure strain ε_{2T} (%)	0.245	0.246
Transverse compressive failure strain, ε_{2C} (%)	1.818	1.2
In-plane shear failure strain, γ_{12u} (%)	4	4
Strain energy release rate, G_{IC} (Jm-2)	220	165
Longitudinal thermal coefficient, α_1 (10^{-6}/°C)	-1	8.6
Transverse thermal coefficient, α_2 (10^{-6}/°C)	26	26.4
Stress free temperature (°C)	120	120

Soden et al. (1998) investigated properties of four unidirectional laminae, four epoxy resin matrices and four types of E-glass or carbon fibres which the properties of one E-glass fibre and carbon fibre between them are close to the properties of the composite material in this study as shown in Table 2-1.

2.1.5 Composite manufacturing methods

Continuous fibre-reinforced PMCs can be fabricated by various techniques. It is very important to align the fibres in the same direction as well as uniformly be distributed within the matrix. The following manufacturing techniques are the most common methods (Aljibori, 2009):

- Autoclave
- Automated Tape Placement
- Bulk Molding Compound

- Filament Winding
- Hand Lay-Up
- Injection Molding
- Pultrusion
- Resin Transfer Molding
- Sheet Molding Compound
- Vacuum Bagging Technique

I discuss the filament winding, hand lay-up and vacuum bagging techniques, since they were the main techniques applied in this study.

2.1.5.1 Filament winding

Filament winding is the lowest cost and the fastest technique for manufacturing of fibre reinforced cylindrical components which is preferred for subsurface activities such as drill holes in the oil and mining industries.

In a filament winding process (Figure 2-1), a band of continuous resin impregnated rovings or monofilaments is wrapped around a rotating mandrel and then cured either at room temperature or in an oven to produce the final product. The technique offers a high speed and precise method for laying many composite layers. The mandrel can be cylindrical, round or any shape that does not have a re-entrant curvature. Among the applications of filament winding are cylindrical and spherical pressure vessels, pipe lines, oxygen and other gas cylinders, rocket motor casings, helicopter blades, large underground storage tanks. The mechanical strength of the filament wound parts not only depends on the composition of component material but also on the process parameters like the winding angle, fibre tension, resin chemistry and curing cycle (Muttana Suresh Babu, 2009).

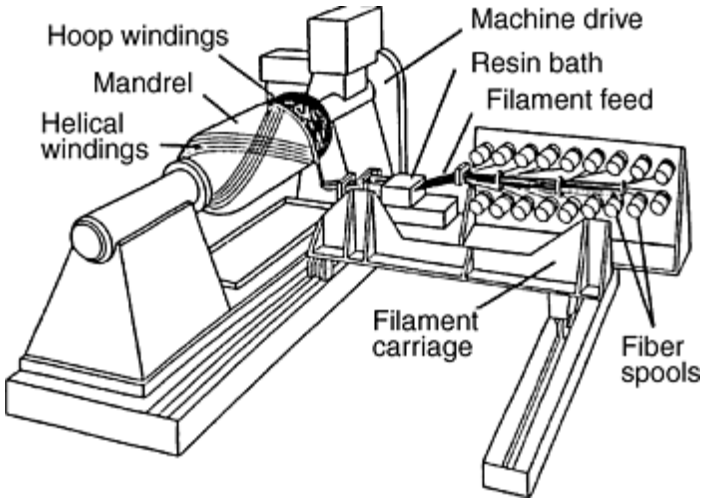

Figure 2-1: Typical filament-winding machine (Miracle et al., 2001)

There are different winding methods if the fibres are passing through a resin bath before reaching the mandrel known as “wet winding”. If prepreg fibres are used it is called “dry winding”. Finally, there is a winding process post-impregnation which is used rarely and depends on the application like embedding electronic sensors. The fibres are wound without any resin application and later the fibres on the mandrel are impregnated with resin.

One of the advantages of the filament winding process is that continuous fibres can be oriented easily in the load direction which simplifies the fabrication of the structures. Secondly, the high fibre volume of a composite is manufactured.

Mertiny et al. (2004) investigated the effect of multi-angle filament winding on the strength of tubular composite structures. The study concluded that multi-angle windings provided considerable advantages over pure angle-ply lay-ups, as well as an overall better performance in resisting damage when subjected to a variety of loading conditions.

Figure 2-2 shows test specimens and techniques for filament-wound composites (FWC). The specimen can be organised in three geometries (I) flat panel, (II) ring, and (III) tubular specimens and how they may be tested.

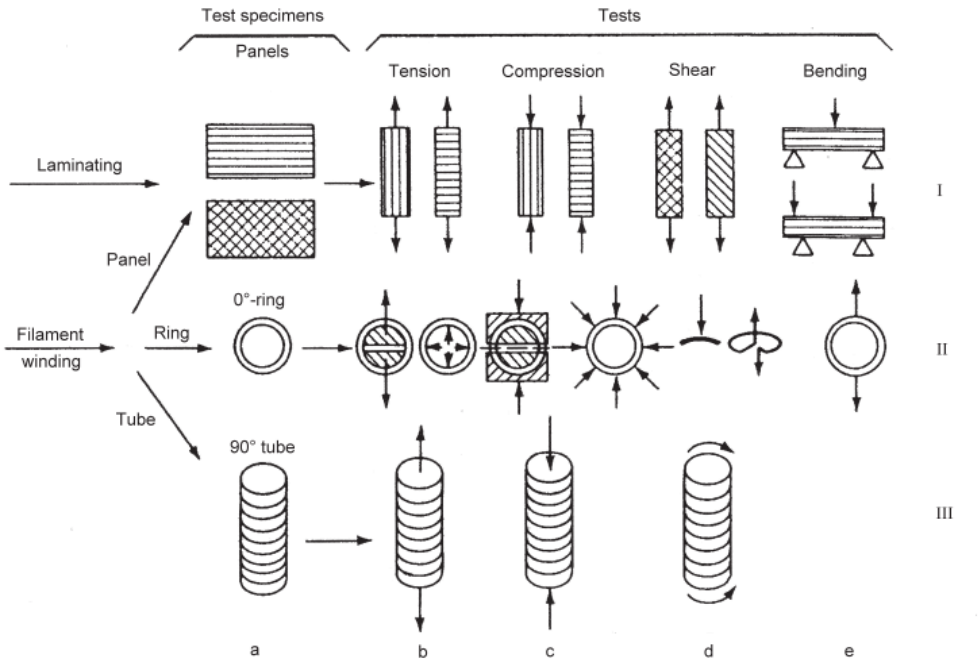

Figure 2-2: Test specimens and test techniques for filament-wound composites (Peters, 1998).

Filament winding is not a manufacturing method that can easily produce test specimens. Designers have been consistently more confident with data derived from test specimens that parallel the configurations of the laminate lay-up. These are the test specimens that support confidence in the filament winding manufacturing process (Peters, 2011).

The structural behaviour of FWC with flat specimens has been studied by others in order to generalize the mechanical response of FWC structures. Torres et al. (2010) investigated the strain field of an FWC pattern at ±55° using flat specimens by measuring the displacement field via digital image correlation. One of the objectives of their study was to relate the failure mechanisms of FWC flat specimens with FWC cylinders. They concluded that the failure mechanisms were similar for both FWC flat cells and FWC cylinders.

Shalom et al. (1997) studied fatigue behaviour of flat filament wound polyethylene composites. Their research showed that the fibre continuity in the filament wound strips resulted in higher failure strains, better fracture toughness and longer fatigue lives.

As filament wound composites are a complicated structure for research, this research focused on simple flat laminated specimens which were fabricated by the hand lay-up technique with the characteristic of a filament winding rhomboid pattern as shown in Figure 2-3.

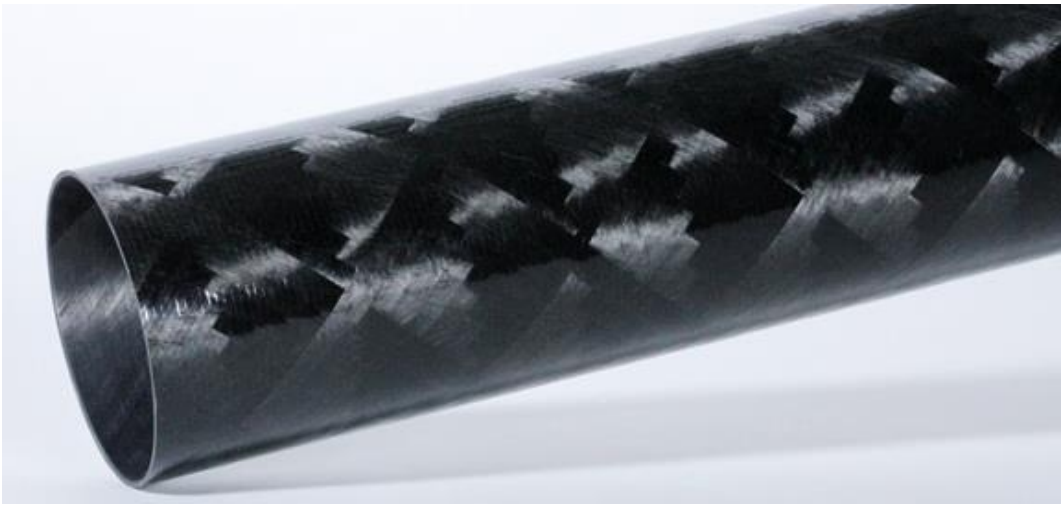

Figure 2-3: Carbon fibre tube manufactured by filament winding method (Composites, 2016)

2.1.5.2 Hand lay-up

The wet hand lay-up method is one of the basic methods of the composite production process. Hand lay-up is a procedure by which plies are manually assembled onto a tool or into an open mold. For the wet lay-up method, hand impregnates resins into fibres, and it is important to distribute the resin fully through the fibres by a brush or rollers or spray guns. Figure 2-4 shows the simple method of a hand lay-up process in which the flat surface is used as a mold, then a release agent is utilized on the surface to prevent laminates from bonding to the surface. The advantage of this technique over others is that the orientation of fibres can be from 0° to 90°.

Most of the time laminates are cured at room temperature using the vacuum bagging technique. The experimental work of this research is based on the vacuum bagging process, so the next section is about vacuum bagging theory and equipment.

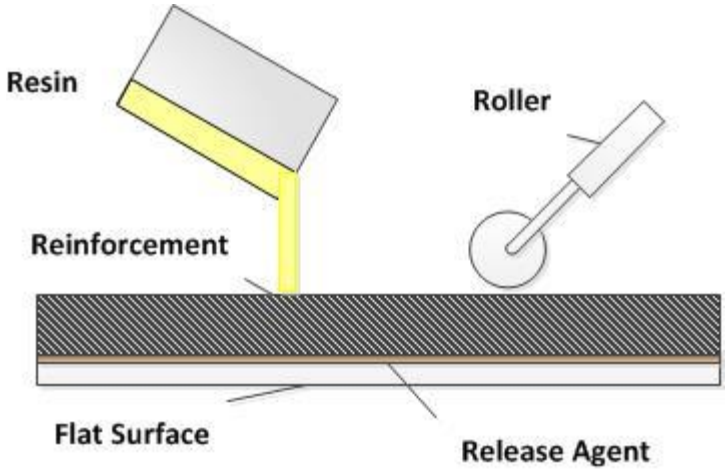

Figure 2-4: Schematic of hand lay-up process

2.1.5.3 Vacuum bagging process

Vacuum Bagging is a clamping method that uses atmospheric pressure to hold the resin in place with fibres until the resin cures. A bag is placed over the curing composite and forced down onto it by vacuum, giving dense materials with better properties (Ashby, 2010). The laminate is sealed within an airtight envelope. The envelope is an airtight flat surface on one side and an airtight bag on the other. Pressure on the inside and outside of this envelope is equal to atmospheric pressure, when the bag is sealed to the mold. The air is evacuated by a vacuum pump from inside the envelope so the result is that it causes air pressure outside of the envelope to remain constant while air pressure inside of the envelope is decreased (Essays, 2013). Atmospheric pressure then applies force on the sides of the envelope and everything within the envelope, putting equal and even pressure over the surface of the envelope as shown in Figure 2-5. The pressure differential between the outside and inside of the envelope is the clamping force on the laminate. A realistic pressure differential is usually between 6 and 12.5 psi.

.

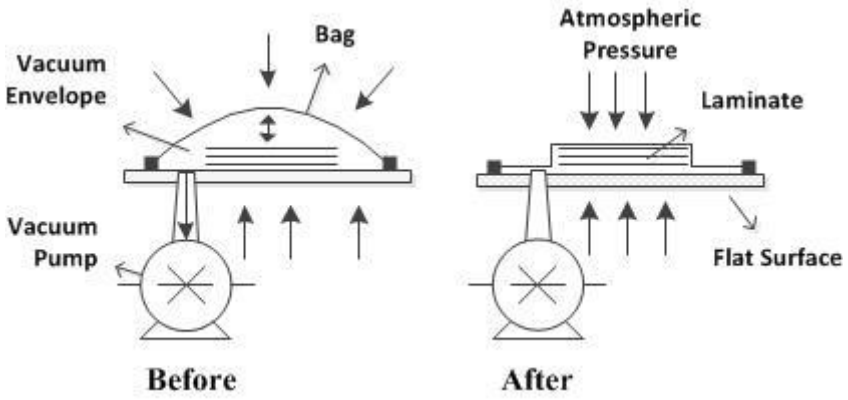

Figure 2-5: A typical vacuum bagging set-up before and after applying vacuum pressure

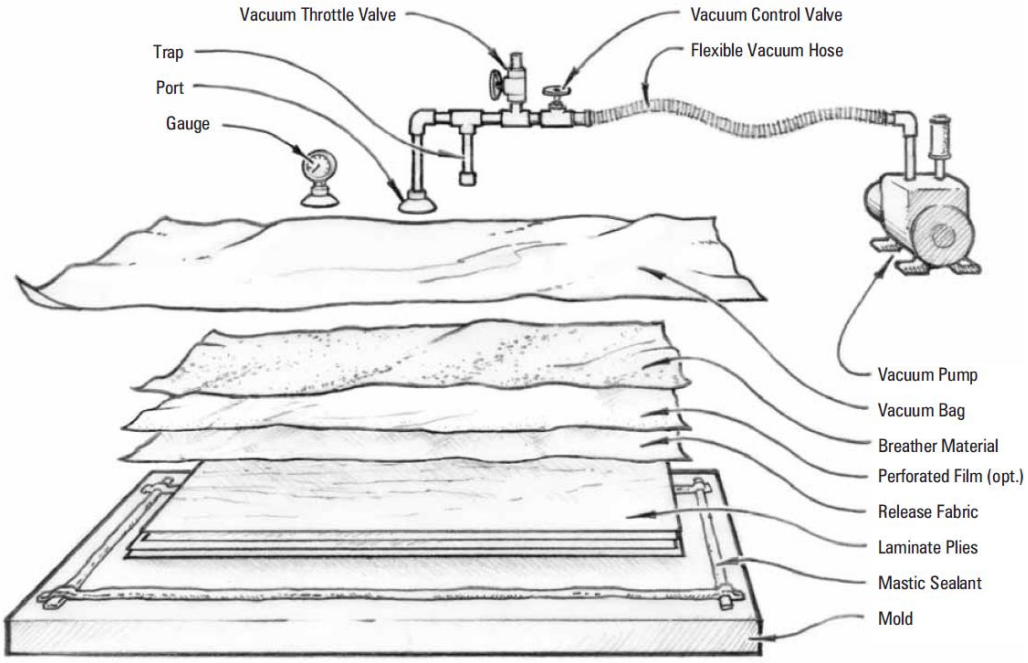

Figure 2-6: Typical components of a vacuum bagging process (Brothers, 2010)

Figure 2-6 shows a typical vacuum bagging method. The following components are the most common parts of the vacuum bagging process.

- Vacuum pumps
- Release fabric
- Perforated film
- Breather material

- Vacuum bag
- Mastic sealant
- The plumbing system
- Mold release

Vacuum pumps play a vital role in this system so it is very important to select the right pump to get a good result. Release fabric, perforated film and breather material are utilized to give a good finish on the surface. A vacuum bag and mastic sealant provide airtight sealing between the bag and the mold. The plumbing system usually consists of a hose, a trap to collect any excess resin before it reaches the pump and a port that connects the envelope to the hose. The mold release or release agent is used to prevent bonding the laminate to the mold.

The vacuum bagging method produces a higher quality result than the hand lay-up method because it removes air bubbles in the resin and the void content is reduced. Higher fibre-to-resin ratios are achieved when excess adhesive in the laminate is controlled which provide higher strength-to-weight ratios. The method also provides control of part thickness by compressing the laminate during cure.

2.2 Composite structural analysis

Composite materials are more complicated in their structures than conventional materials such as most metals, plastics, and ceramics. The purpose of this section is to explain fundamental theory of composite structure and their design. There are many parameters in the design of composite structures that need to be understood and addressed. The structures of isotropic materials are the same in all directions. However, composites are non-isotropic or anisotropic because fibres are not oriented equally in all directions.

The material is called orthotropic when the fibres are oriented in all directions. In addition, the material is pseudo-isotropic when the fibres are directed in specific directions in a plane (Strong, 2008)

2.2.1 Laminate composite

A laminate is made by bonding two or multiple layers of fibre reinforced composite materials together and a lamina is a layer in a laminated composite or a

single ply. Each layer includes fibre reinforcement such as glass, carbon and boron embedded in a thermoplastic or thermosetting resin matrix. Each lamina is thin while not all single plies has the same material and fibre orientation. Some layers may have glass fibres while others may use carbon fibres. Some laminates may consist of a few layers and some of more than a hundred layers. Therefore, each lamina can show a different behaviour.

To analyse laminate composite, it is important to describe a coordinate system for specifying locations through the thickness, along the length and across the width. There are two common coordinate systems to describe a laminate (Hyer & White, 1998):

The 1-2-3 coordinate system or principal material coordinate system which has one axis aligned with the fibre direction (axis 1 is aligned with the fibre direction) and two axes that are perpendicular to the plane of the fibre (axes 2 and 3 are called matrix directions). To make the analysis easier, it is assumed that the two-material fibre-matrix system is replaced by a single homogenous material. Although directions 2 and 3 are both perpendicular to the fibre direction, their properties are not necessarily equal to each other. The 1-2-3 coordinate system is usually used to explain the lamina or layer direction of the laminate.

The second coordinate system is an x-y-z Cartesian coordinate system or global coordinate system which describes the geometry of the laminate structure. If we are to accommodate multiple layers in a laminate with different fibre orientation then it is essential to use multiple 1-2-3 coordinate systems, each with its own orientation with respect to the global coordinate system.

Figure 2-7 (b) shows two coordinate systems which are related to each other through the simple rotation angle θ about the z axis. The fibres are directed at angle θ with respect to + x axis, as it can be seen the x-y plane is parallel to the fibres, and the z axes and 3 coincide. The angle θ is considered positive when the fibres orient counter clockwise from +x axis toward the +y axis and is negative when the fibres orient counter clockwise from –x axis toward the –y axis.

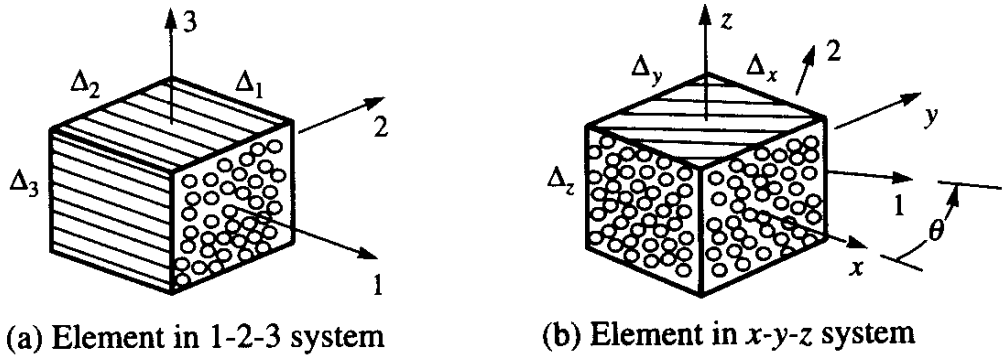

Figure 2-7: Elements of laminate composite in 1-2-3 and x-y-z coordinate system (Hyer & White, 1998).

In this research the origin of the thickness coordinate, designated z, is located at the laminate geometric mid-plane (Voyiadjis, 2005). Figure 2-8 illustrates a global Cartesian coordinate system with a generally flat laminate including N layers. Figure 2-8 (a) shows a cross-sectional view in the x-z plane, the thickness of laminate is shown as H and the thickness of each ply is denoted by h. The bottom of the laminate starts with Layer 1 and finishes at Layer N at the top in the most positive z location. As mentioned, each lamina or layer can have different thickness, material and fibre orientation. Figure 2-8 (b) indicates the top view of the laminate with layer N that is the closest lamina to the viewer in the x-y plane. The fibre orientation relative to the +x axis of each lamina identifies the fibre angle of various layers.

Lay-up notation is important to ensure that the lay-up orientation achieved in manufacture of the laminate is similar to the engineering requirements. There are different methods to show the ply lay-up orientations but I selected the most common way that is popular in the aerospace industry for this research.

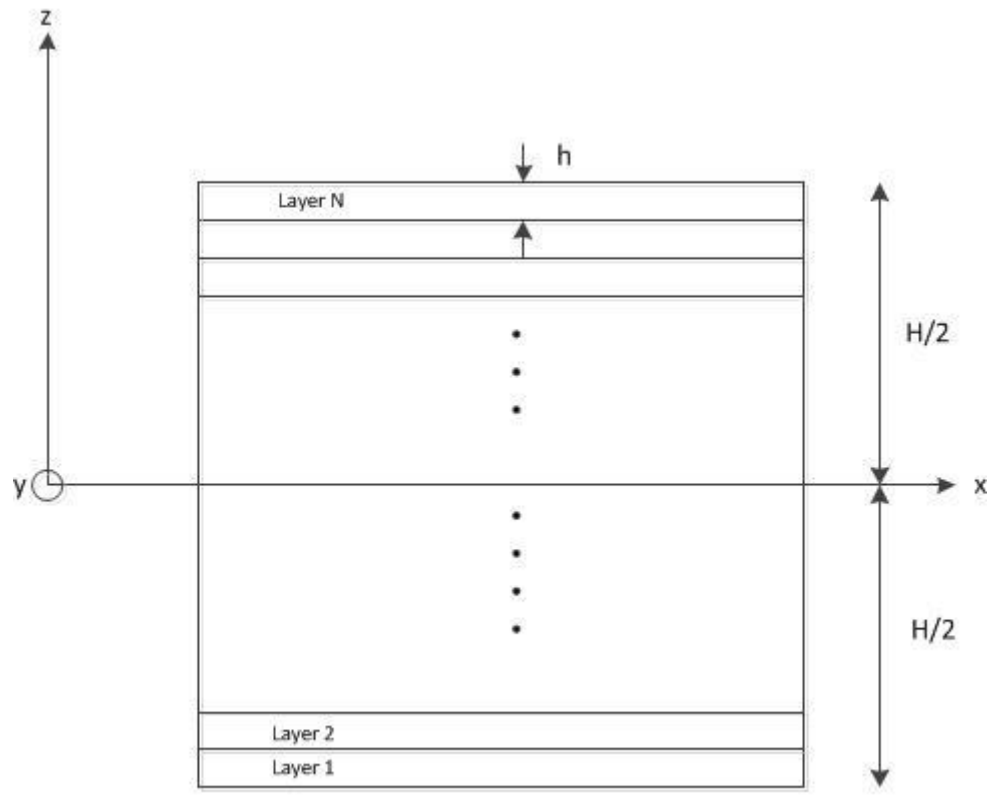

a) x-z plane view

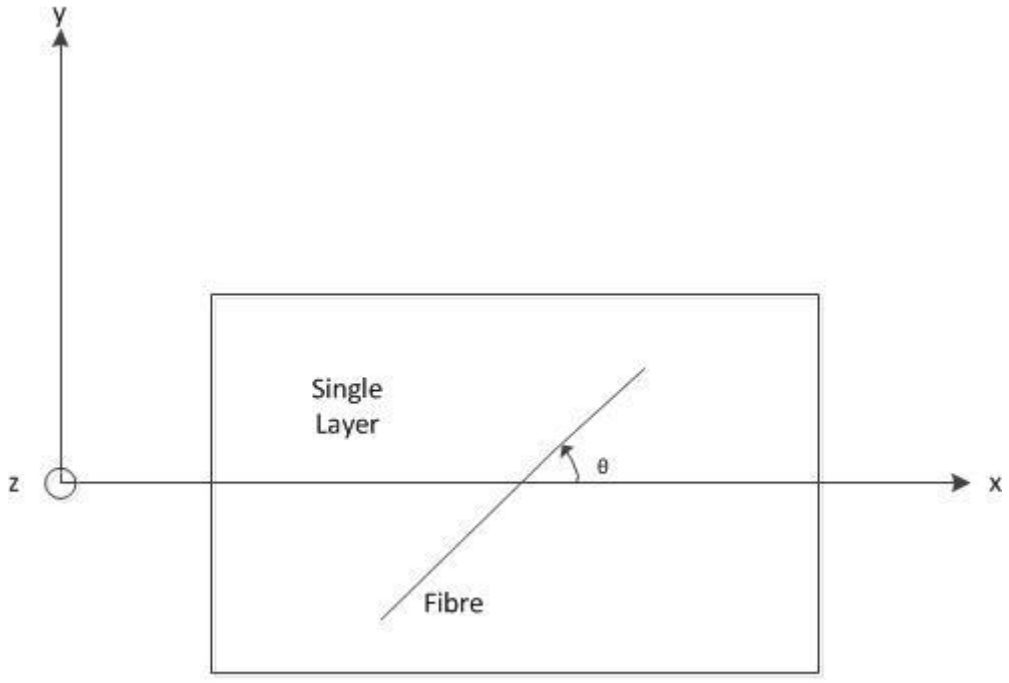

b) x-y plane view

Figure 2-8: Laminate lay-up from two different views

To specify the laminate patterns, there are basic rules as follows below (Strong, 2008):

- Laminate notation is written between square brackets. For example [notation]
- The left most entry in the notation is the fibre angle of layer 1
- A slash separates each layer for example: [layer1/layer2/layer3]
- Fibre angles of equal but opposite direction (plus/minus orientation) can be shown as: [+75/–75] → [±75]
- Multiple angle plies can be written with a subscript for example [0/0/0/90/90] → $[0_3/90_2]$
- A laminate with mid-plane symmetry uses an "s" subscripted outside the brackets:
  [+75/-75/+10/-10/-10/+10/-75/+75] → $[\pm 75/\pm 10]_s$
- For hybrid laminate lay-ups, the individual plies are coded with the material of that ply (FG = fiberglass and C = carbon): $[(\pm 75)_C/(\pm 10)_{FG}]_s$

Figure 2-9 shows an example of a symmetric laminate structure with unidirectional continuous fibres and various angle ply for each layer.

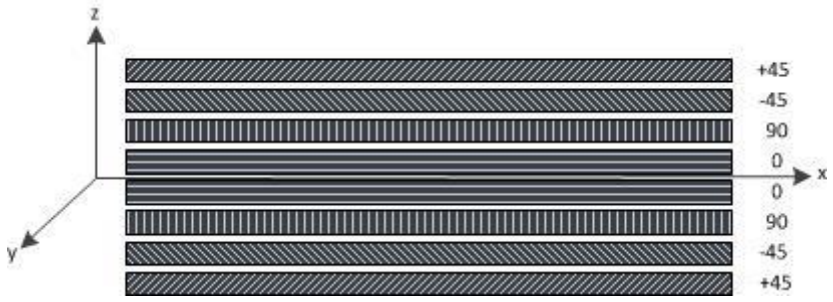

Figure 2-9: Symmetric laminate $[\pm 45/90/0]_s$

In summary, to design composite laminates three main variables should be considered: the number of layers, the angle of each lamina, and, the stacking sequence of the laminate which is the through-the-thickness order of how the layers are laid-up in the laminate (Cousigné et al., 2013).

The mechanical properties of a laminate can be changed significantly by changing

the stacking sequence of the laminate and the orientation of individual layers in the laminate.

2.2.2 Laminate theory

The basic theory of laminate analysis is referred to as Classical Laminate Theory (CLT) which calculates the mechanical response of a laminate by the following assumptions (Baker, et al., 2004):

- For two-dimensional plane stress analysis, the strain is constant through the thickness.
- For bending, the strain varies linearly through the thickness.
- The laminate is thin compared with its in-plane dimensions.
- Each layer is quasi-homogeneous and orthotropic.
- Displacements are small compared with the thickness.
- The behaviour remains linear.

To determine the response of a composite laminate, it is necessary to know the elastic properties or stiffness of the material. The stiffness of an orthotropic material can be determined by four elastic constants below:

E_1, E_2, G_{12} and ν_{12}

Where, E_1= Longitudinal stiffness

E_2 = Transverse stiffness

G_{12} = Shear stiffness

ν_{12} = Poisson's ratio

The stress-strain law for a single ply (an orthotropic material) under plane stress conditions, in the material axes is described as:

$$\begin{Bmatrix} \sigma_1 \\ \sigma_2 \\ \tau_{12} \end{Bmatrix} = \begin{bmatrix} Q_{11} & Q_{12} & 0 \\ Q_{12} & Q_{22} & 0 \\ 0 & 0 & Q_{66} \end{bmatrix} \begin{Bmatrix} \varepsilon_1 \\ \varepsilon_2 \\ \gamma_{12} \end{Bmatrix} \qquad (2.1)$$

Where Q_{ij}, is called the "reduced stiffness", given:

$$Q_{11} = \frac{E_1}{1-\nu_{12}\nu_{21}}$$

$$Q_{22} = \frac{E_2}{1-\nu_{12}\nu_{21}} \qquad (2.2)$$

$$Q_{12} = \frac{\nu_{21}E_1}{1-\nu_{12}\nu_{21}}$$

$$Q_{66} = G_{12}$$

As mentioned earlier, when a ply is accommodated in a laminate with fibres at an angle of θ (Figure 2-7 (b)) it is called an "off-axis" ply. Therefore, it is necessary to transform the stress-strain law from the material coordinate system to the global coordinate system (the laminate axes). Figure 2-9 shows the stresses (σ_x, σ_y, and τ_{xy}) and strains (ε_x, ε_y, and γ_{xy}) in the laminate axes.

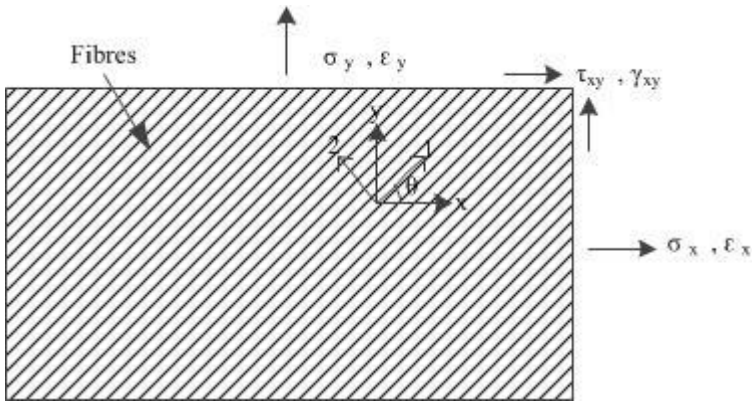

Figure 2-10: Laminate axes for a single ply

After transforming the stresses and strains the Q_{ij}, reduced stiffnesses are changed to $\bar{Q}_{ij}$ which are termed the "transformed reduced stiffnesses" or the off-axis reduced stiffnesses, and the result is equation (2.3):

$$\begin{Bmatrix} \sigma_x \\ \sigma_y \\ \tau_{xy} \end{Bmatrix} = \begin{bmatrix} \bar{Q}_{11} & \bar{Q}_{12} & \bar{Q}_{16} \\ \bar{Q}_{12} & \bar{Q}_{22} & \bar{Q}_{26} \\ \bar{Q}_{16} & \bar{Q}_{26} & \bar{Q}_{66} \end{bmatrix} \begin{Bmatrix} \varepsilon_x \\ \varepsilon_y \\ \gamma_{xy} \end{Bmatrix} \qquad (2.3)$$

The $\bar{Q}_{ij}$ matrix is changed significantly with θ and defined by (Udar & Datta, 2007):

$$\bar{Q}_{11} = Q_{11}m^4 + 2(Q_{12} + 2Q_{66})n^2m^2 + Q_{22}n^4$$

$$\bar{Q}_{12} = (Q_{11} + Q_{22} + 4Q_{66})n^2m^2 + Q_{12}(n^4 + m^4)$$

$$\bar{Q}_{16} = (Q_{11} - Q_{12} - 2Q_{66})nm^3 + (Q_{12} - Q_{22} + 2Q_{66})n^3m \qquad (2.4)$$

$$\bar{Q}_{22} = Q_{11}n^4 + 2(Q_{12} + 2Q_{66})n^2m^2 + Q_{22}m^4$$

$$\bar{Q}_{26} = (Q_{11} - Q_{12} - 2Q_{66})n^3m + (Q_{12} - Q_{22} + 2Q_{66})nm^3$$

$$\bar{Q}_{66} = (Q_{11} + Q_{22} - 2Q_{12} - 2Q_{66})n^2m^2 + Q_{66}(n^4 + m^4)$$

Where, m= Cosθ, and n= Sinθ

Equations (2.3) and (2.4) are very important equations in the analysis of fibre-reinforced composite material. The laminate stresses are functions of the thickness (z) as well as the material properties in each layer which can change due to different fibre orientation and materials. In conclusion, the variation of stresses through the thickness of the laminate is discontinuous and completely different from the variation through the thickness of an isotropic material as shown in Figure 2-11.

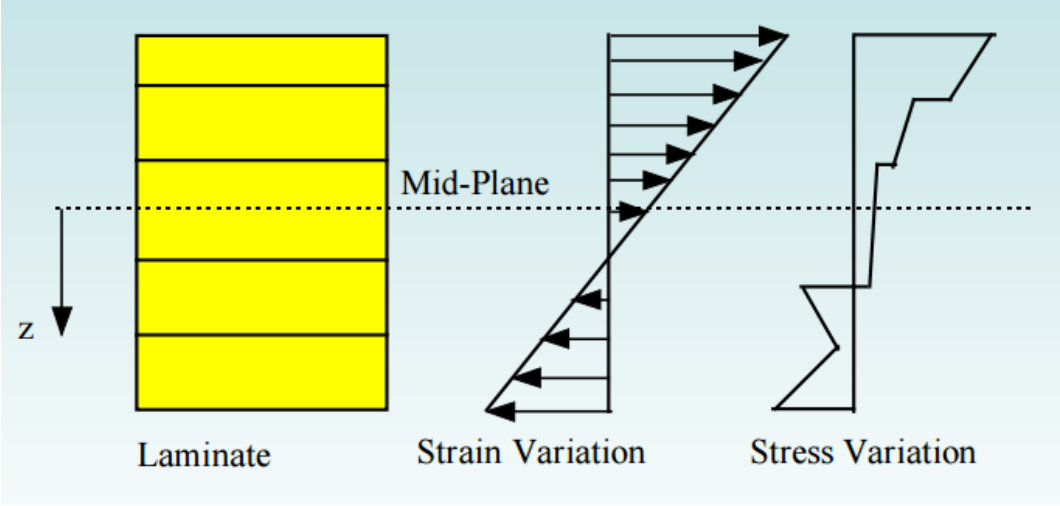

Figure 2-11: Stress-strain variation through the thickness of a laminate (Kaw, 2006).

The result (Figure 2-12) of integrating the stresses through the thickness of the laminate, is three force and moment resultants (N_x and M_x in the x direction, N_y M_y in the y direction, N_{xy} and M_{xy} in the shear direction) which are defined by:

$$N_x = \int_{-\frac{H}{2}}^{\frac{H}{2}} \sigma_x dz$$

$$N_y = \int_{-\frac{H}{2}}^{\frac{H}{2}} \sigma_y dz \qquad (2.5)$$

$$N_{xy} = \int_{-\frac{H}{2}}^{\frac{H}{2}} \tau_{xy} dz$$

$$M_x = \int_{-\frac{H}{2}}^{\frac{H}{2}} \sigma_x z dz$$

$$M_y = \int_{-\frac{H}{2}}^{\frac{H}{2}} \sigma_y z dz \qquad (2.6)$$

$$M_{xy} = \int_{-\frac{H}{2}}^{\frac{H}{2}} \tau_{xy} z dz$$

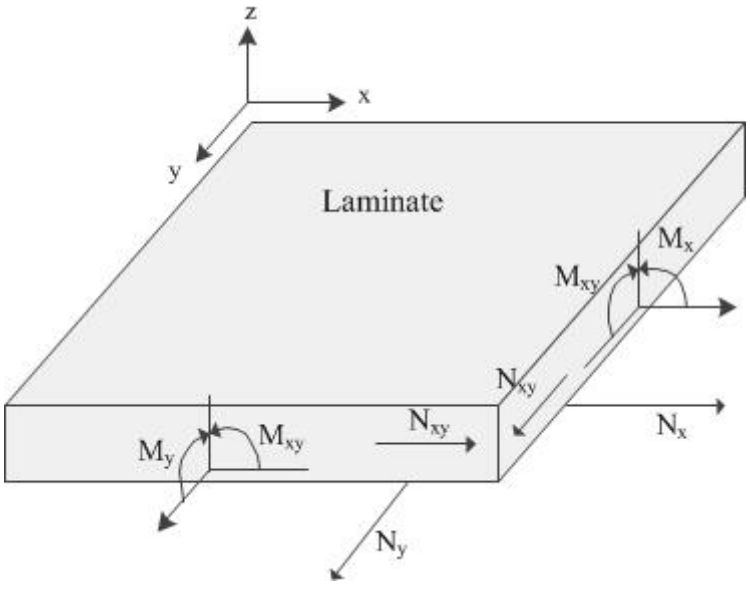

Figure 2-12: Force and moment resultants in three directions of a laminate axis

Figure 2-12 illustrates the directions of the normal force resultants (N_x and N_y) and the shear force resultant, N_{xy}, as well as bending moment resultants (M_x, M_y) and the twisting moment resultant M_{xy}. The force and moment resultants also involve the stresses σ_x, σ_y, τ_{xy}. From the stress-strain relations the stresses can be written in terms of strain. Therefore, the ABD matrix which is a 6x6 matrix that serves as a connection between the stress resultants (i.e., loads) applied to a laminate, and the associated reference surface strains and curvatures (i.e., deformations) defines the elastic properties of the entire laminate. The laminate stiffness matrix involves everything that is used to define the laminate such as layer material properties, location, thickness, and fibre orientation (Hyer and White, 1998).

Laminate loading-deformation relations are defined by (Birman, 2011):

$$\begin{Bmatrix} N_x \\ N_y \\ N_{xy} \end{Bmatrix} = \begin{bmatrix} A_{11} & A_{12} & A_{16} \\ A_{12} & A_{22} & A_{26} \\ A_{16} & A_{26} & A_{66} \end{bmatrix} \begin{Bmatrix} \varepsilon^\circ_x \\ \varepsilon^\circ_y \\ \gamma^\circ_{xy} \end{Bmatrix} + \begin{bmatrix} B_{11} & B_{12} & B_{16} \\ B_{12} & B_{22} & B_{26} \\ B_{16} & B_{26} & B_{66} \end{bmatrix} \begin{Bmatrix} k^\circ_x \\ k^\circ_y \\ k^\circ_{xy} \end{Bmatrix} \qquad (2.7)$$

$$\begin{Bmatrix} \mathrm{M_x} \\ M_y \\ M_{xy} \end{Bmatrix} = \begin{bmatrix} B_{11} & B_{12} & B_{16} \\ B_{12} & B_{22} & B_{26} \\ B_{16} & B_{26} & B_{66} \end{bmatrix} \begin{Bmatrix} \varepsilon^\circ_x \\ \varepsilon^\circ_y \\ \gamma^\circ_{xy} \end{Bmatrix} + \begin{bmatrix} D_{11} & D_{12} & D_{16} \\ D_{12} & D_{22} & D_{26} \\ D_{16} & D_{26} & D_{66} \end{bmatrix} \begin{Bmatrix} k^\circ_x \\ k^\circ_y \\ k^\circ_{xy} \end{Bmatrix} \qquad (2.8)$$

To form one matrix relationship between the six stress resultants and the six reference surface deformations, equations (2.7) and (2.8) are combined and the result is (Voyiadjis, 2005).

$$\begin{Bmatrix} N_x \\ N_y \\ N_{xy} \\ M_x \\ M_y \\ M_{xy} \end{Bmatrix} = \begin{bmatrix} A_{11} & A_{12} & A_{16} & B_{11} & B_{12} & B_{16} \\ A_{12} & A_{22} & A_{26} & B_{12} & B_{22} & B_{26} \\ A_{16} & A_{26} & A_{66} & B_{16} & B_{26} & B_{66} \\ B_{11} & B_{12} & B_{16} & D_{11} & D_{12} & D_{16} \\ B_{12} & B_{22} & B_{26} & D_{12} & D_{22} & D_{26} \\ B_{16} & B_{26} & B_{66} & D_{16} & D_{26} & D_{66} \end{bmatrix} \begin{Bmatrix} \varepsilon^\circ_x \\ \varepsilon^\circ_y \\ \gamma^\circ_{xy} \\ k^\circ_x \\ k^\circ_y \\ k^\circ_{xy} \end{Bmatrix} \qquad (2.9)$$

Where,

the quantities ε°_x, ε°_y, γ°_{xy} are referred to as the "reference surface strain" in the x, y and shear direction, and

the quantities k°_x, k°_y, k°_{xy} are referred to as the "reference surface curvature" in

the x, y, and twisting curvature.

The A-matrix is also called the "laminate extensional stiffness" matrix and its components are defined as:

$$A_{ij} = \sum_{k=1}^{N} \bar{Q}_{ijk} \left(Z_k - Z_{k-1}\right) \tag{2.10}$$

The B-matrix is called the "laminate coupling stiffness" matrix and its components are defined as:

$$B_{ij} = \frac{1}{2} \sum_{k=1}^{N} \bar{Q}_{ijk} \left({Z^2}_k - {Z^2}_{k-1}\right) \tag{2.11}$$

The D-matrix is called the "laminate bending stiffness" matrix and its components are defined as:

$$D_{ij} = \frac{1}{3} \sum_{k=1}^{N} \bar{Q}_{ijk} \left({Z^3}_k - {Z^3}_{k-1}\right) \tag{2.12}$$

If the loads are known, the deformation can be determined by inverting equation (2.9) as (Hyer & White, 1998):

$$\begin{Bmatrix} {\varepsilon^\circ}_x \\ {\varepsilon^\circ}_y \\ {\gamma^\circ}_{xy} \\ {k^\circ}_x \\ {k^\circ}_y \\ {k^\circ}_{xy} \end{Bmatrix} = \begin{bmatrix} a_{11} & a_{12} & a_{16} & b_{11} & b_{12} & b_{16} \\ a_{12} & a_{22} & a_{26} & b_{12} & b_{22} & b_{26} \\ a_{16} & a_{26} & a & b_{16} & b_{26} & b_{66} \\ b_{11} & b_{12} & b_{16} & d_{11} & d_{12} & d_{16} \\ b_{12} & b_{22} & b_{26} & d_{12} & d_{22} & d_{26} \\ b_{16} & b_{26} & b_{66} & d_{16} & d_{26} & d_{66} \end{bmatrix} \begin{Bmatrix} N_x \\ N_y \\ N_{xy} \\ M_x \\ M_y \\ M_{xy} \end{Bmatrix} \tag{2.13}$$

where,

$$\begin{bmatrix} a_{11} & a_{12} & a_{16} & b_{11} & b_{12} & b_{16} \\ a_{12} & a_{22} & a_{26} & b_{12} & b_{22} & b_{26} \\ a_{16} & a_{26} & a & b_{16} & b_{26} & b_{66} \\ b_{11} & b_{12} & b_{16} & d_{11} & d_{12} & d_{16} \\ b_{12} & b_{22} & b_{26} & d_{12} & d_{22} & d_{26} \\ b_{16} & b_{26} & b_{66} & d_{16} & d_{26} & d_{66} \end{bmatrix} = \begin{bmatrix} A_{11} & A_{12} & A_{16} & B_{11} & B_{12} & B_{16} \\ A_{12} & A_{22} & A_{26} & B_{12} & B_{22} & B_{26} \\ A_{16} & A_{26} & A_{66} & B_{16} & B_{26} & B_{66} \\ B_{11} & B_{12} & B_{16} & D_{11} & D_{12} & D_{16} \\ B_{12} & B_{22} & B_{26} & D_{12} & D_{22} & D_{26} \\ B_{16} & B_{26} & B_{66} & D_{16} & D_{26} & D_{66} \end{bmatrix}^{-1}$$

(2.14)

To determine the stresses and strain distribution in each layer we need to know the reference surface strains and curvatures. Therefore, equations (2.9) and (2.13) play a vital role in analysis of composite structures.

As we work with symmetric balanced laminates, it is necessary to mention that a symmetric laminate does not possess coupling between in-plane and flexural behaviour. As a result, all the components of the B matrix are identically zero. Also the components A_{16} and A_{26} are always zero in a balanced laminate.

2.3 Failure theories of composite materials

Failure of conventional materials such as metals is predictable when comparing stresses or strains caused by applied loads and is a function of allowable strength or the strength of the material. Some isotropic materials have yielding behaviour so a few failure theories such as the von Mises theory and the maximum shear stress theory (Tresca theory) are utilized, while others fail as a result of brittle fracture and theories like maximum normal stress theory and Mohr theory can be used. However, composite materials are anisotropic and they do not yield. Therefore, investigation of the failure mechanisms can be complicated and research in to failure is an ongoing activity.

Clearly, to investigate the failure of composite material, many mechanisms and criteria should be considered because one criterion cannot predict failure for all loading conditions and composite materials. However, none of the failure theories currently available are considered accurate enough to be used as a sole performance predictor of design (Staab, 2015). If failure theories are considered as indicators of failure rather than as predictors then having those theories available becomes an acceptable situation (Hyer and White, 1998).

Several failure theories have been proposed for composite materials which are shown below:

- Maximum stress
- Maximum strain
- Tsai-Hill
- Tsai-Wu

- Hoffman
- Hashin
- Puck

In this research, I explain the maximum stress, the maximum strain, Tsai-Hill and Tsai-Wu theories. These approaches are selected because they are among the most commonly used for composite materials. Consequently, the simplified form of these four theories is presented below.

2.3.1 Maximum stress criterion

The maximum stress theory states that the failure occurs when the stresses in the principal material directions are more than the corresponding allowable or ultimate strengths. This criterion can be described by the following equations:

For Tension, $\sigma_1 > X_t$, $\sigma_2 > Y_t$, $\sigma_{12} > S$ (2.15)

For Compression, $\sigma_1 > X_c$, $\sigma_2 > Y_c$ (2.16)

where, X_t is the tensile strength in the longitudinal (1) direction, X_c is the compressive strength in the longitudinal (1) direction, Y_t is the tensile strength the transverse (2) direction, Y_c is the compressive strength in the transverse (2) direction, and S is the in-plane shear strength (Enke & Sandor, 2009).

2.3.2 Maximum strain criterion

Maximum strain theory states that the failure will happen when any strain in the principal material directions is greater than the corresponding allowable or ultimate strains. Thus, the criterion is expressed as:

For Tension, $\varepsilon_1 > \varepsilon^{ut}_1$, $\varepsilon_2 > \varepsilon^{ut}_2$, $\gamma_{12} > S_\varepsilon$ (2.17)

For Compression, $\varepsilon_1 > \varepsilon^{uc}_1$, $\varepsilon_2 > \varepsilon^{uc}_2$ (2.18)

In these inequalities, ε^{ut}_1, ε^{uc}_1 are the maximum tensile strain and compressive strain at failure, respectively. For loading in the longitudinal (1) direction, ε^{ut}_2, ε^{uc}_2 are the maximum tensile strain and compressive strain, respectively. Failure for loading in the transverse (2) direction, S_ε is the shear strain at failure for an in-plane shear test of the lamina.

It should be mentioned that in the case of multiaxial stress and strain or the interaction between them, the simple relationships just given are no longer valid. Maximum stress and strain theories are often used because of their simplicity and are not very consistent (Staab, 2015).

2.3.3 Tsai–Hill criterion

Tsai-Hill theory is based on an extension to von Mises yield criterion. It says that failure occurs when the following inequality is satisfied:

$$(\frac{\sigma_1}{X})^2 - (\frac{\sigma_1\sigma_2}{X^2}) + (\frac{\sigma_2}{Y})^2 + (\frac{\sigma_{12}}{S})^2 \geq 1 \quad , \qquad (2.19)$$

where, σ_1 and σ_2 are both tensile stresses, X is the ultimate tensile strength in the longitudinal (1) direction, Y is the ultimate tensile strength in the transverse (2) direction, and S is the in-plane shear strength of the lamina. When the state of stress is compression rather than in tension, the ultimate compression strength X and Y as well as compressive stresses σ_1 and σ_2, are used in equation (2.19).

Tsai-Hill criterion considers the interaction between strengths and failure modes which gives an advantage over maximum stress and strain theories as well as gives reasonably good results for many kinds of composite lamina and experimental data (Eshbach and Kutz, 2009).

2.3.4 Tsai–Wu criterion

According to the Tsai-Wu criterion (Tsai and Wu, 1971) failure is imminent when the following inequality has occurred:

$$\left(\frac{1}{X_t} - \frac{1}{X_c}\right)\sigma_1 + \left(\frac{1}{Y_t} - \frac{1}{Y_c}\right)\sigma_2 + \left(\frac{1}{X_tX_c}\right)\sigma_1^2 + 2f_{12}\sigma_1\sigma_2 + \left(\frac{1}{Y_tY_c}\right)\sigma_2^2 + \frac{1}{S^2}\sigma_{12}^2 \neq 1 \qquad (2.20)$$

where, the coefficient f_{12} should be determined by a biaxial tensile test. However, it is not that easy to set up the biaxial test in the lab. One researcher (Forde, 2009) suggested that f_{12} can be zero or calculated by the following equation:

$$f_{12} = -\frac{1}{2}\sqrt{\frac{1}{X_tX_cY_tY_c}} \qquad (2.21)$$

As can be seen from equation (2.20), Tsai-Wu theory accounts for the stresses

interaction the same as Tsai-Hill but it is easier to use computationally.

Figure 2-13 represents failure envelopes and a comparison of maximum stress, maximum strain, Tsai-Hill and Tsai-Wu theories for a glass-fibre lamina when S=0 (Forde, 2009). It shows that different theories are reasonably close under positive stresses and big differences occur when compressive stresses are present. In conclusion, a conservative approach is to consider all available theories.

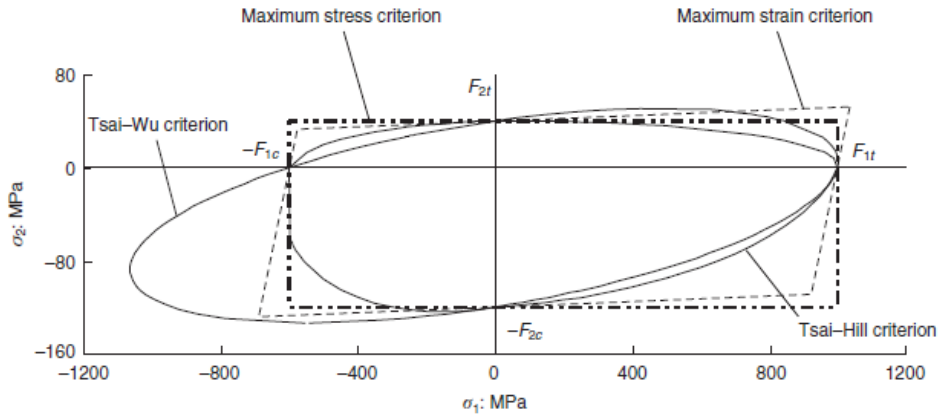

Figure 2-13: Failure envelops for different failure criteria (Forde, 2009)

2.4 Primary stress classification

To design composite laminates, it is necessary to know the types of stresses that affect the laminates so the four basic stress categories which are usually considered in composite structure design are (Strong, 2008) :

- Axial and transverse in-plane tensile stresses (1–2 plane)
- Axial and transverse in-plane compressive stresses (1–2 plane)
- In-plane shear stresses (1–2 plane)
- Interlaminar stresses (1–3 and 2–3 planes)

2.4.1 Axial and transverse in-plane tensile stresses

This type of stress occurs along the principal material directions of a composite material and is dependent upon the response of the fibres in directions 1 (axial direction) and 2 (transverse direction). Tensile stresses in the axial and transverse in-plane directions are shown by σ_1 and σ_2 respectively.

2.4.2 Axial and transverse in-plane compressive stresses

Compressive stresses in the principal directions of a composite material act similarly to tensile stresses but in the opposite direction so they are designated by $-\sigma_1$and $-\sigma_2$ (Kaw, 2006).

2.4.3 In-plane shear stresses (1–2 plane)

The shear stress can be converted into biaxial compressive and tensile stresses along the direction of ±45° in the 1-2 planes. When a composite structure is supporting shear stresses (torque), plies in ±45° direction carry the loads.

2.4.4 Interlaminar stresses

Through-the-thickness stresses or interlaminar stresses are divided into three normal stresses σ_3, and two shear stresses τ_{13}, τ_{23}. They are also called 'out-of-plane' stresses. In composite materials, the high strength and modulus of reinforcements (fibres) provide their stiffness and strength, and thus, because there are no fibres in those plane directions (σ_3, τ_{13}, τ_{23}), the matrix (resin) has responsibility to absorb the stresses which is not a desirable attribute for designing laminates. Interlaminar stresses usually appear at free edges, hole (notch), ply-drop-off, bonded joint and delamination buckle as shown in Figure 2-14 (b). We must decrease interlaminar stresses to get an optimum laminate design.

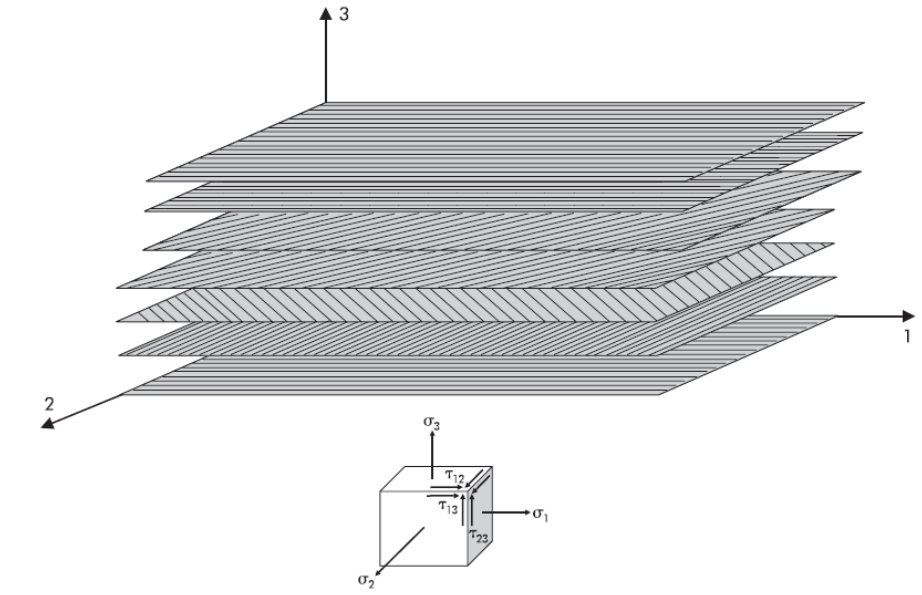

a)

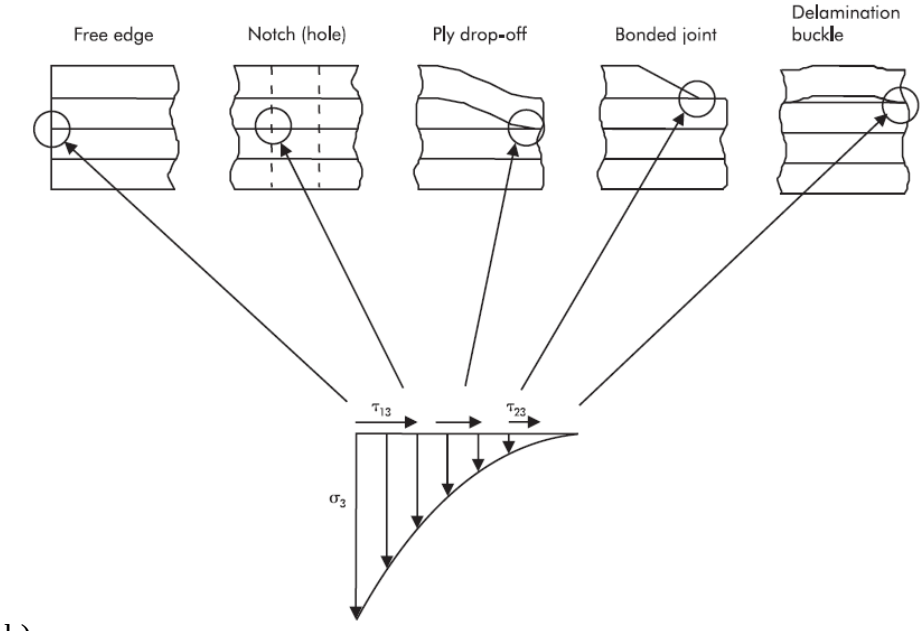

b)

Figure 2-14: a) Four basic stress types, b) Typical locations of interlaminar stresses (Strong, 2008)

Embedding a sensor within a composite material can cause changes in the microstructure that would be expected to have a vital influence on the stresses in the composite materials. Interlaminar stresses appear at, or around the material interfaces. As a result these may lead to a depletion of the load carrying capability of the composite structure (Herrero, 2007). On the other hand, failure initiation may occur due to interlaminar stresses between the interface of an embedded

sensor and the housing material. Thus, it is important for the composite laminate to have an optimum design to compensate for the strength reduction due to embedded sensors.

2.5 Chapter conclusions

From amongst the different types of matrix materials for possible use, epoxy was selected as the bonding agent because of excellent properties such as high strength, adhesion, and low shrinkage. The second phase of a composite material is the reinforcement material. Fibre glass and carbon fibre in the form of continuous fibres, are the most efficient type of reinforcing materials. I have explained that by combining reinforcing material in the form of carbon fibre and fibreglass in a common matrix of epoxy could offer the benefits provided by both fibres. The hybrid composite was proposed as a host material for embedding the CB. The mechanical and physical properties of E-glass/Epoxy and Carbon/Epoxy (which were used in the finite element analysis) were presented.

Among the various composite manufacturing methods, the filament winding and hand lay-up with a vacuum bagging process were explained in detail as they were the focus of this research. It was stated that since a filament wound composite is a complicated structure for research, this study was based on developing a simple flat laminated specimen which would be fabricated by the hand lay-up technique with the characteristic of a filament winding rhomboid pattern.

The primary theory behind the numerical analysis in the research is Classical Laminate Theory which was explained in some detail. Failure theories of composite materials were described and it was explained that one failure criterion alone cannot predict the failure for all loading conditions and composite materials in contrast with the failure of conventional materials such as metals. The Tsai–Hill criterion was selected for analysis of the failure using FEA which gives reasonably good results for many kinds of composite lamina and experimental data.

Four types of stresses affect laminates when structural designing composites. Failure may initiate due to interlaminar stresses between the interface of an embedded sensor and the host material.

3 COMPOSITE LAMINATE DESIGN

In order to embed a sensor/circuit board within a laminate composite, an optimum laminate design should be selected from the other possible designs. This chapter explains how an optimum laminate design was selected.

3.1 Laminate stacking sequence

Arrangement of ply orientations and material components through the laminate thickness is called the 'stacking sequence'. The quantity of the stacking sequence is based on the number of plies, so that by increasing the number of plies a greater stacking sequence is possible. For instance a symmetrical eight-ply laminate with four various ply orientations has 24 different stacking sequences. Pagano (Pagano & Pipes, 1994) noted that the structural properties of laminate such as stiffness and strength can be influenced by the laminate stacking sequence (LSS).

To select the optimum laminate design between different LSS, this study has followed the recommendations from the military industry (MIL-HDBK-17-3F, 2002) as the general environment sustained by military actions (harsh environment) can be similar to a drilling activity. A summary of the recommendations is as follows:

- A LSS should have at least four distinct ply angles with a minimum of 10% of the plies oriented at each angle. Ply angles should be selected such that fibres are oriented with principal load axes.
- Minimize groupings of plies with the same orientation
- If possible, LSS should be balanced and symmetric about the midplane. (A LSS is considered symmetric if plies positioned at an equal distance above and below the midplane are identical (i.e., material, thickness, and orientation). Balance is defined as having equal numbers of $+\theta$ and $-\theta$ plies, where θ is measured from the primary load direction.

Laminate design starts by selecting the number of plies and ply angles required for a given application. Therefore, it is necessary to discuss now the amount of load and stresses that we expect to apply to the manufactured composite.

For the majority of logging tools that are used by borehole wireline systems which hang from a cable in a hole, gravity is the main load which causes axial tensile stress. The other load which is considered relatively negligible is hydrostatic pressure applied by the residual mud wrapped around the logging tool, which as the tool travels to deeper depth in the borehole, a transverse compressive stress is applied on the outside periphery of the pipe. Section 3.1.1 explained that fibres in the axial (0°) and transverse (90°) directions respond to such stresses (tensile and compressive stresses) in the principal directions.

Before embedding an electronic sensor within a composite material, it is necessary to achieve the optimum laminate design. By considering the appropriate recommendations and the applications, five different symmetric balanced multi-angle laminated lay-ups were selected using eight plies (Ameri et al., 2014):

Table 3-1: Five different LSS in 8-plies (Ameri et al., 2014)

Ply	**$[\pm45/\pm10]_s$**	**$[\pm55/\pm10]_s$**	**$[\pm65/\pm10]_s$**	**$[\pm75/\pm10]_s$**	**$[\pm85/\pm10]_s$**	**Material**
8	+45	+55	+65	+75	+85	Carbon Fibre
7	-45	-55	-65	-75	-85	Carbon Fibre
6	+10	+10	+10	+10	+10	Fibre Glass
5	-10	-10	-10	-10	-10	Fibre Glass
4	-10	-10	-10	-10	-10	Fibre Glass
3	+10	+10	+10	+10	+10	Fibre Glass
2	-45	-55	-65	-75	-85	Carbon Fibre
1	+45	+55	+65	+75	+85	Carbon Fibre

It is difficult during filament winding fabrication to wind 0° fibres around the mandrel, so ±10° was considered as a base line for all five LSS which as the closest fibre angle to 0° (axial direction) that could be fabricated by a local manufacturing company. Yang (Yang, 2013) suggested in that study when laminates have angle plied as $[\theta/-\theta]s$, an angle is suggested between 60° and 90° to lower the free edge effect (interlaminar stresses). Due to the electrical

conductivity of carbon fibre, a sensor's performance may be anticipated to deteriorate. Consequently a hybrid structure was designed. Glass fibre was located in the middle for isolation of the sensor from the carbon-fibre plies (Ameri et al., 2014) as shown in Table 3-1.

The fibre angles in the transverse directions were selected as a result of their being popular in industry applications. For example ±55° is very common when used in pressure vessels and pipe applications (Rosenow, 1984). Kaddour et al. (1996) investigated the burst behaviour of ±75 ° filament-wound Kevlar/epoxy and carbon/epoxy tubes at high loading rates. Gemi et al, (2009) studied the fatigue failure behaviour of glass/epoxy $[\pm 75]_2$ filament-wound pipes under pure internal pressure. Kaddour et al. (2003) analysed the behaviour of ±45° glass/epoxy filament wound composite tubes under quasi-static equal biaxial tension–compression loading. It is also recommended by filament winding manufacturers that for optimum resistance of external pressure and buckling the use of approximately ± 65°is preferred. In summary, to embed an electronic sensor, an optimally designed LSS needs to be chosen by using computer-aided engineering (CAE) software, of which Hypersizer is one option.

3.2 Hypersizer®

Computer-aided engineering (CAE) software HyperSizer® was used for design and lay-up optimization of the laminate's structure. HyperSizer® performs design, stress analysis, and detail sizing optimization for aircraft and space launch vehicles which are fabricated with composite or traditional metallic materials (Beam, 2008). The reliability of the software has been proven by various researchers and NASA (National Aeronautics and Space Administration).

Bednarcyk et al. (2012) investigated multiscale fatigue analysis of composite panels. They incorporated fatigue life prediction capabilities of the composite panels into the HyperSizer® as well as models with experimental fatigue life data. In conclusion, the model matched well with the experimental data.

Hrinda (2008) utilized Hypersizer® to optimize the composite structure of an aerospace vehicle at NASA's Langley Research Centre. He analysed three conceptual vehicle designs and concluded that the software enabled the structure

of the three vehicles to be quickly investigated against many candidate structural systems and materials while providing the lightest design.

For a better understanding of the software, it is necessary to explain some details. Hypersizer® reports all analyses results in terms of margins of safety (MS) which is defined as:

$$MS = \frac{P_{allow}}{P_{applied}} - 1 \qquad (3.1)$$

where P_{allow} is the generic allowable load defined by the type of fibre, matrix, number of layers, angle of fibre and $P_{applied}$ is the applied load. MS is a non-dimensional quantity and is used for entering test data within HyperSizer® (Corp, 2014).

"HyperSizer® optimizes structures by generating a finite domain of candidate panels for each component. The pool of candidate panels is sorted by weight and then analysed sequentially to find the lightest panel(s) that pass all margin checks" (Corp, 2011).

HyperSizer® analyses the laminate by extending the classical lamination theory (CLT) to stiffened panels. The main method is a constitutive relation that relates panel-level strains to panel-level loads. This relation is referred to as the ABD matrix which was explained in the previous Chapter on laminate theory and by equation (2.9).

The quadratic failure theory of Tsai-Hill was used for the laminate design in this research, which attempts to account for the interaction between different components of stress and strain (Figure 3-1). The Margin of Safety will be computed for each ply in a laminate, but only the lowest margin of safety will be reported.

Tsai-Hill theory was described in Chapter 2 and equation (2.19) shows the general form of the interaction equation. HyperSizer® rewrites the interaction equation as a margin of safety and performs for each ply in the laminate.

If X≥Y:

$$MS = \frac{1}{\sqrt{(\frac{\sigma_1}{X})2 - (\frac{\sigma_1\sigma_2}{X^2}) + (\frac{\sigma_2}{Y})2 + (\frac{\sigma_{12}}{S})2}} - 1 \quad (3.2)$$

If X<Y:

$$MS = \frac{1}{\sqrt{(\frac{\sigma_1}{X})2 - (\frac{\sigma_1\sigma_2}{Y^2}) + (\frac{\sigma_2}{Y})2 + (\frac{\sigma_{12}}{S})2}} - 1 \quad (3.3)$$

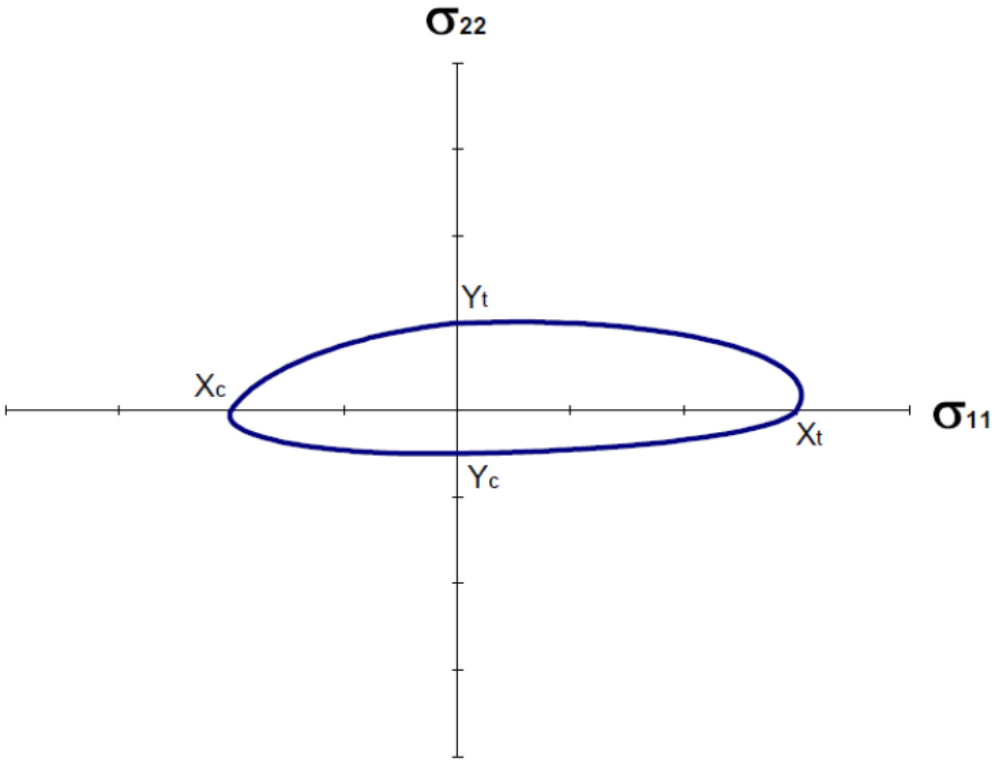

Figure 3-1: Tsai-Hill failure envelope with differently allowable compression/tension values (Corp, 2012)

The Tsai-Hill criterion converts to the maximum stress criterion under uniaxial loading conditions. However, all three in-plane stress components affect the failure of the ply in the presence of a multi-axial stress field. An important

advantage of the Tsai-Hill criterion is that the interaction of the stress components allows the Tsai-Hill criterion to correlate significantly better with experimental composite ply level failure data. In addition, the fact that the failure envelope is smooth is more realistic, and the fact that it entails one equation rather than five is also advantageous as shown in Figure 3-2. These advantages come while the Tsai-Hill criterion is no more difficult to characterize than the maximum stress criterion (only the uniaxial composite strengths are required) (Corp, 2012).

3.2.1 Hybrid laminates model

Five different hybrid lay-up configurations in 8-plies (Table 3-1) were modelled and subjected to in-plane normal loading of N_x. Accordingly no twisting and bending moments are considered in the analysis because the laminate is only subject to in-plane load and its symmetric, curvature terms become zero. Therefore, the laminates remain flat.

Two fibre materials (Carbon-fibre T300 and Silenka E-Glass 1200tex) were considered in the lay-up sequence optimization as shown in Table 2-1. The laminates consist of plies with fibre-glass having the same fibre orientation as a baseline and plies with carbon-fibres of different fibre orientations which are chosen as the design variables.

As discussed before, Tsai-Hill failure theory was used in the analysis. The applied loading is uniaxial (N_x=1000lbf/in). The thickness of the laminates is constant for all LSS designs. The strengths and weaknesses of the laminate models were determined by the software's interactive reporting of margins-of-safety.

Five lay-up configurations were simulated as shown in Figure 3-3 which shows only the laminate model for $[(\pm 75)_C/(\pm 10)_{FG}]_S$ with three variables in fibre angle, density and thickness of each ply. The laminates were analysed to achieve the highest MS and to determine the optimum laminate design.

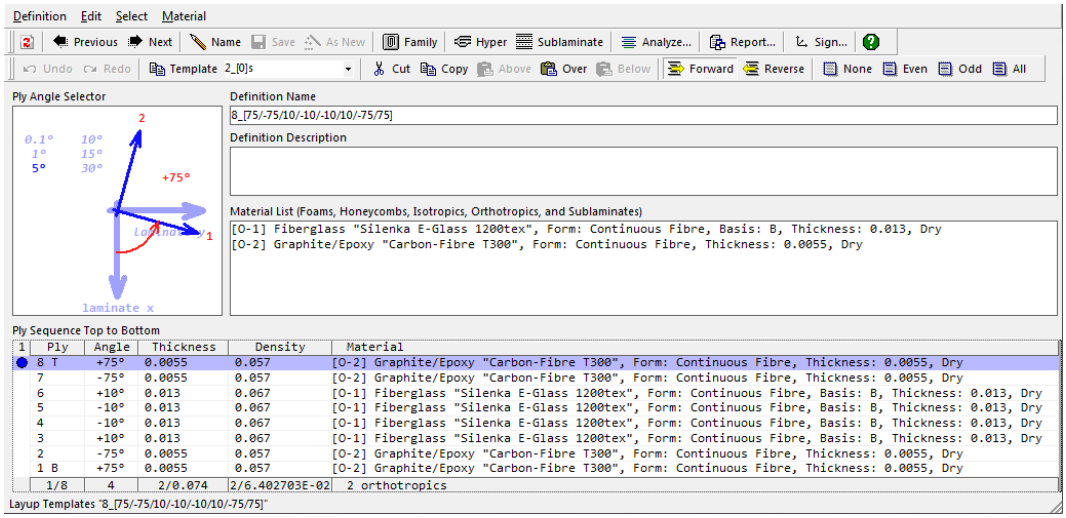

Figure 3-2: $[(\pm75)_C/(\pm10)_{FG}]_S$ was modelled by HyperSizer®

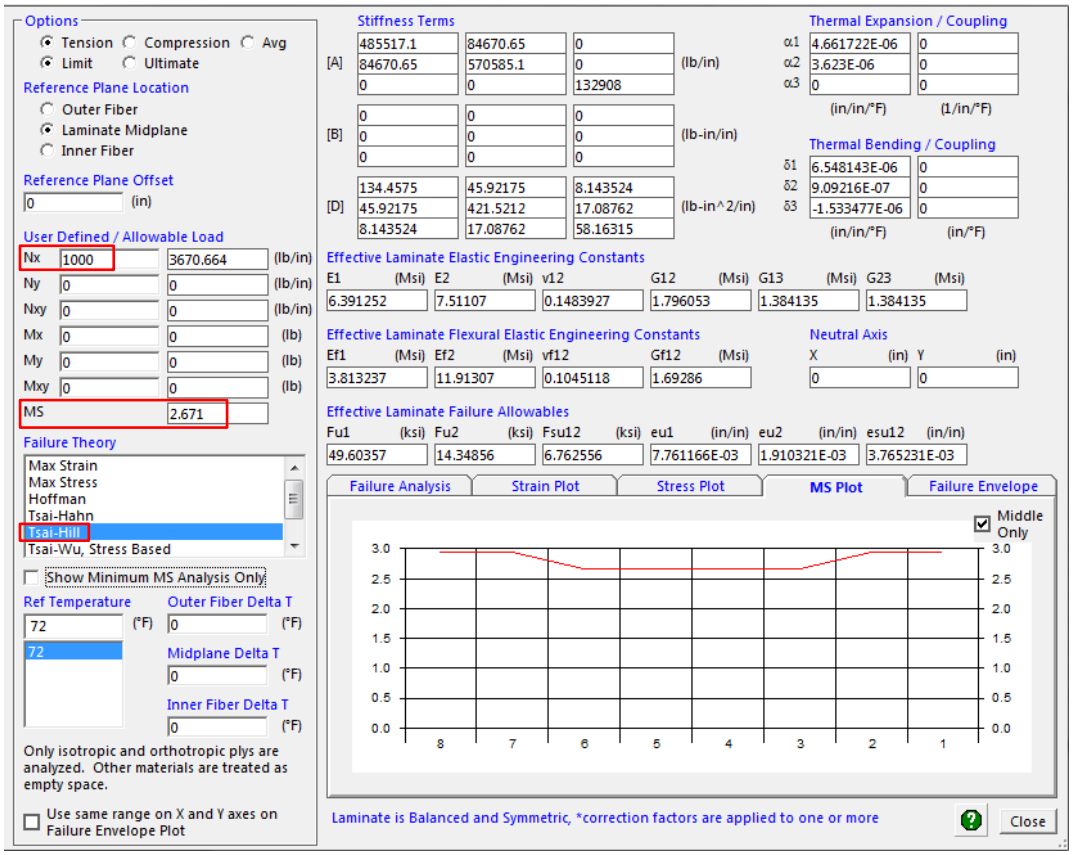

Figure 3-3: Laminate analysis of $[(\pm75)_C/(\pm10)_{FG}]_S$ based on applied uniaxial load N_X, margin of safety (MS) and Tsai-Hill theory.

Figure 3-4 shows that by selecting Tsai-Hill failure theory and 1000 lb/in applied uniaxial load, the minimum MS for $[(\pm 75)_C/(\pm 10)_{FG}]_S$ would be 2.671. The ABD matrix was calculated to get the laminate stiffness properties. Simulation runs were performed for the other laminate designs and the results indicated that the $[(\pm 75)_C/(\pm 10)_{FG}]_S$ laminate angles maintained the higher MS values, compared to the other laminate design angles (Ameri et al., 2014), as presented in Figure 3-5.

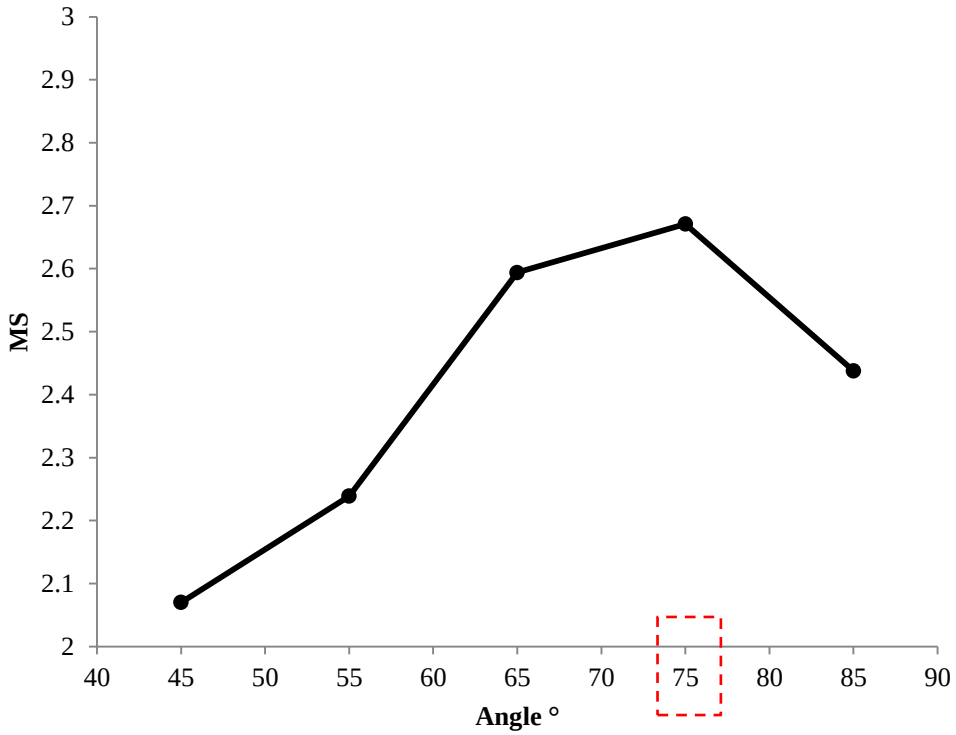

Figure 3-4: Margin of safety VS various multi-angle laminates (Ameri et al., 2014)

3.3 Chapter conclusions

To achieve the optimum design, five different symmetric multi-angle laminated lay-ups were evaluated in eight plies. In order to detect the optimum design over the multi-angle laminates, a constant uniaxial load of 1000 lb/in was applied at 0 degrees (N_X) on the eight layer laminates. It was assumed that the load in the hoop and shear directions were zero (N_Y and N_{XY}). Based on Tsai-Hill theory, simulation runs were performed for each laminate design and the results indicated that the $[(\pm 75)_C/(\pm 10)_{FG}]_S$ laminate angles maintained higher MS values, compared to the other laminate design angles.

Table 3-2: Information of hosing laminate to embed the sensor

$[\pm 75/\pm 10]_s$	Material	Thickness (mm)
+75	Carbon Fibre	0.15
-75	Carbon Fibre	0.15
+10	Fibre Glass	0.3
-10	Fibre Glass	0.3
-10	Fibre Glass	0.3
+10	Fibre Glass	0.3
-75	Carbon Fibre	0.15
+75	Carbon Fibre	0.15

The $[(\pm 75)_C/(\pm 10)_{FG}]_S$ design became the benchmark for further studies. Table 3-2 shows the details of the laminate to house the electric sensor/circuit board.

4 COMPOSITE LAMINATE ANALYSIS

In order to minimise testing time and risk such as physical harm, cost and delay to the research, the Finite Element Analysis (FEA) method was used in this research. FEA provides detailed stress and deformation solutions for understanding stress applied to complex shapes. Composite flat hybrid laminates with and without an embedded sensor/circuit board (CB) were modelled using ANSYS Composite PrepPost (ACP) software. Input and output of models are discussed in this chapter. Model validation results via experimental and mechanical test studies that are performed on flat hybrid composite will be discussed.

The numerical study was initially carried out using a tube geometry. The tube geometry was converted to a flat geometry and the results of both models were compared to demonstrate that the flat geometry model can represent the tube geometry.

4.1 FEA of flat hybrid laminate

4.1.1 Introduction

ACP software provides all necessary functions for the analysis of layered composite structures. The challenge is to predict how well the designed model will perform under real-world working conditions. This involves considering stresses and deformations as well as a range of failure criteria. ACP has a pre- and post-processing mode. In the pre-processing mode, all composite definitions can be created and are mapped to the geometry (FEA mesh). These composite definitions are transferred to the FEA model and the solver input file. In the post-processing mode, after a solution is completed and result file(s) are imported, post-processing results (failure, strains and stresses) can be evaluated and visualised (ANSYS, 2013).

ACP is used to analyse the composite laminate by using Classical Laminate Theory (CLT), which was described in Section 2.2.2. The following assumptions were made by the software (ANSYS, 2013):

- Layers are perfectly bonded together.
- The material properties of each layer are constant through the thickness.
- Linear-elastic stress-strain behaviour.
- Lines originally straight and normal to the mid-plane, remain straight and normal in extension and bending.
- Plane stress state.
- In-plane strains and curvature are small compared to all other dimensions.

ACP reports the failure analysis based on three terms as follows:

- Reserve factor (RF)
- Inverse reserve factor (IRF)
- Margin of safety (MoS)

The RF indicates margin to failure. RF values greater than one indicates a positive margin to failure and values less than one indicates a negative margin. The values of reserve factors are always greater than zero (Sahin, 2012).

$$\mathrm{RF} = \frac{\text{Ultimate Strength}}{\text{Ultimate load}} \qquad \begin{cases} \mathrm{RF} > 1 \ \text{Safe} \\ \mathrm{RF} < 1 \ \text{Failure} \end{cases} \tag{4.1}$$

IRF is often preferred in practice due to greater accuracy than RF.

$$\mathrm{IRF} = \frac{\text{Ultimate load}}{\text{Ultimate Strength}} \qquad \begin{cases} \mathrm{IRF} > 1 \ \text{Failure} \\ \mathrm{IRF} < 1 \ \text{Safe} \end{cases} \tag{4.2}$$

MoS is an alternative for the reserve factor in indicating margin to failure. The margin of safety is obtained from the corresponding formula (Sahin, 2012).

$$\mathrm{MoS} = \frac{\text{Material Strength}}{\text{Design load}} - 1 \qquad \begin{cases} \mathrm{MoS} < 0 \ \text{Failure} \\ \mathrm{MoS} > 0 \ \text{Margin to Failure} \end{cases} \tag{4.3}$$

4.1.2 Flat hybrid composite model

Two composite material properties (Carbon-fibre T300 and Silenka E-Glass 1200tex) were imported into ACP using the same data as the Hypersizer® model (shown in Table 2-1). The second step was to create the flat laminate geometry. The dimensions of the models were based on the specimens to be used in the experimental work. A flat rectangular shape of 8-ply hybrid laminate composite $[(\pm 75)_C/(\pm 10)_{FG}]_S$ with a length of 300mm and 50mm in width was created. The thickness of the laminate was that of the laminate thickness in Hypersizer® which was 1.8mm. The dimensions of the embedded sensor/CB were 75x31x0.1mm. The material of the CB was made of thin copper coated by a thin layer of epoxy.

After determining the geometry of the specimens, the laminate hybrid composite was based on the stacking sequence of $[(\pm 75)_C/(\pm 10)_{FG}]_S$. Table 4-1 shows the fibre orientation and material of each ply in the flat hybrid composite laminate for two models with and without an embedded CB . The CB was located right in the middle of the laminate. The mesh element size of the geometry and relevance centre were selected 3mm and coarse, respectively.

Table 4-1: Summary of hybrid composite model with and without embedded Circuit Board (Ameri et al., 2014)

With CB		
Ply	**$[\pm 75_C/\pm 10_{FG}]_s$**	**Material**
Top 9	+75	Carbon Fibre
8	-75	Carbon Fibre
7	+10	Fibre Glass
6	-10	Fibre Glass
5	0	Copper (CB)
4	-10	Fibre Glass
3	+10	Fibre Glass
2	-75	Carbon Fibre
Bottom 1	+75	Carbon Fibre
Without CB		
Ply	**$[\pm 75_C/\pm 10_{FG}]_s$**	**Material**
Top 8	+75	Carbon Fibre
7	-75	Carbon Fibre
6	+10	Fibre Glass
5	-10	Fibre Glass
4	-10	Fibre Glass
3	+10	Fibre Glass
2	-75	Carbon Fibre
Bottom 1	+75	Carbon Fibre

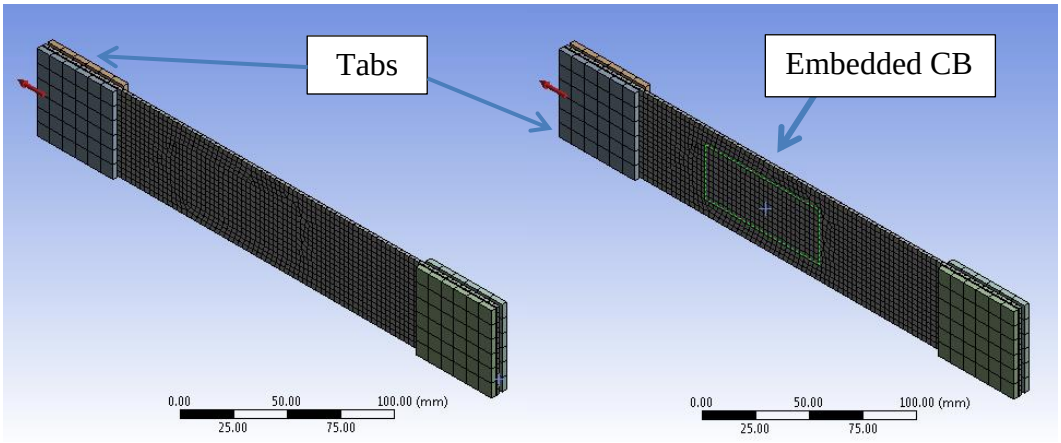

Figure 4-1: Flat laminate specimen model with and without embedded CB subjected to applied tensile load

The specimens were subjected to a uniaxial tensile load of 44 kN applied on one end of the specimen and the other end was fixed. The applied load in Y and Z directions was zero to avoid bending and rotation of the model. Figure 4-1 shows the 3-D geometry of the flat laminate composite model specimens with and without an embedded CB and four tabs in each end-side to distribute the load from the grips into the specimen with a minimum of stress concentration, the boundary condition between the specimen and tabs were selected bonded. The red arrow in Figure 4-1 shows the direction of the applied load. The green dashed line represents the boundary condition of the embedded CB and the host material.

4.1.3 Stress analysis of flat laminate

The simulation study was to evaluate the ply-by-ply stress distribution through the laminate, boundaries of an embedded CB with the host material and comparison of the structural strength between the two (with and without embedded CB) models. ACP is capable of showing the stress distribution for each ply using a contour plot that is actually a vector in the form of element/node.

As can be seen in Figures 4-2 and 4-3, the fibre-glass layers in ±10° mostly share the applied tensile load. The negative stress values represent compression which occurs at the carbon fibres ±75° due to the Poisson effect. When the models were subjected to a normal tensile stress, in one direction, it caused extension of the laminate in direction x and due to the Poisson effect, contraction in directions y

and z. The model without CB shows that the maximum stress is located in the boundary between the tabs and the composite laminate. Therefore, the failure was anticipated to take place close to the tabs. On the other hand, the model with embedded CB showed that the inter-laminar stress concentration increased in the interface between the CB and fibre-glass ply in layers ±10° which would cause matrix crack initiation or delamination.

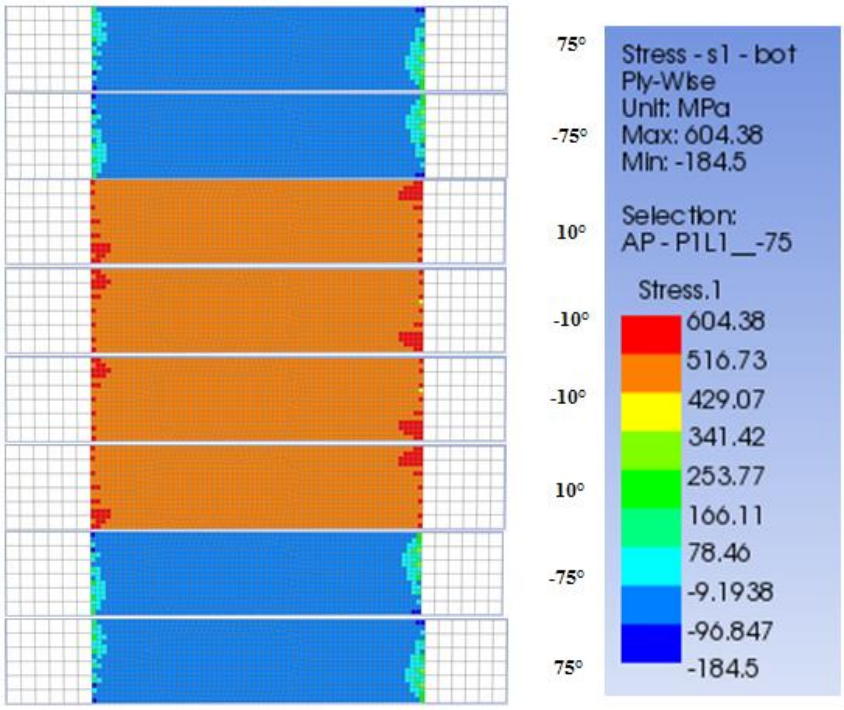

Figure 4-2: Contour plot in flat hybrid composite laminate without embedded CB after applied load for each ply

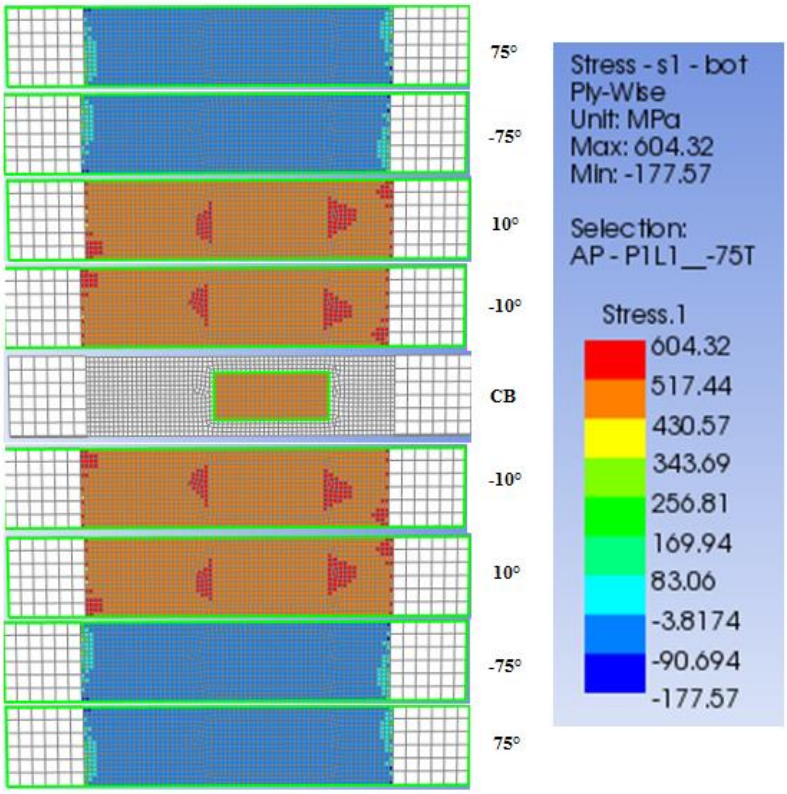

Figure 4-3: Contour plot in flat hybrid composite laminate with embedded CB after applied load for each ply

Two areas were studied in the counter plot- the area of the embedded CB and the interface area between the CB and the host material as shown in Figure 4-3 by the green dashed line.

1.A.1.1 Area of the location of embedded CB

By selecting the sampling element (SE) on the nodes of the models, we are able to see the stress distribution through the thickness of the laminate. Sampling element is a good tool to evaluate the structural strength between the two (with and without) embedded CB models. Figure 4-4 indicates the location of the sampling element in both models that were selected at even positions.

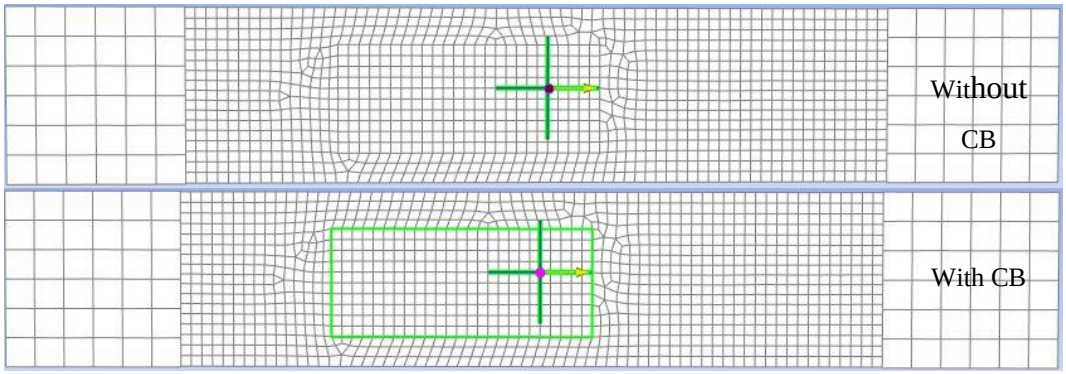

Figure 4-4: Location of sampling elements for models with and without CB

Figure 4-5 illustrates the distribution of the stress through the thickness of the laminate for the model with and without an embedded CB. The stress is constant within each layer but varies from ply to ply. When a laminate is subjected to a unidirectional tensile load, directions of the fibres will govern the distribution of the stresses in the layers. The layers with fibres aligned with the load, bear most of the load and the layers that are not aligned with the load direction will be affected by Poisson factor that will demonstrate negative stresses (compression).

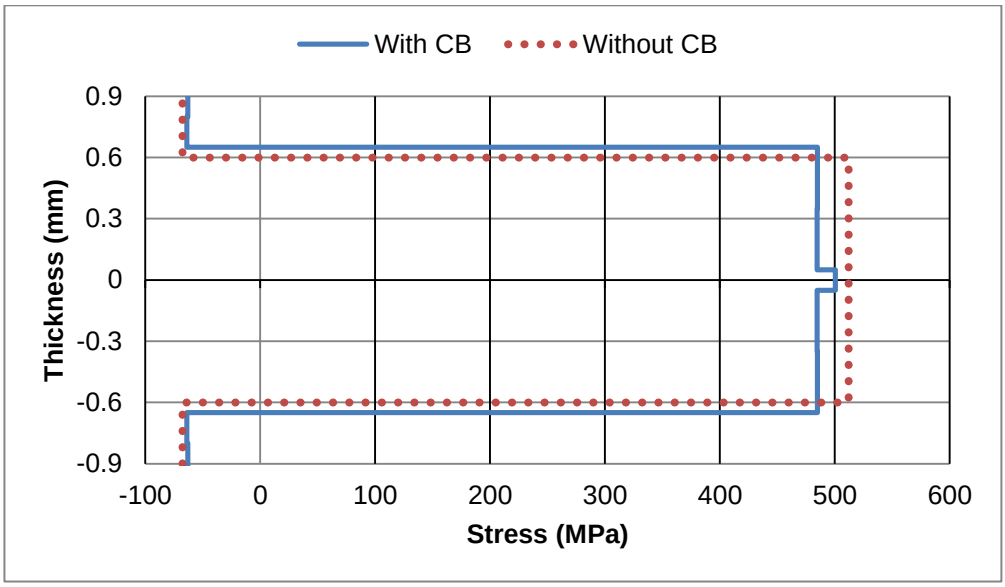

Figure 4-5: Ply-by-ply stress distribution through the thickness of $[\pm 75_C/\pm 10_{FG}]_s$ hybrid laminate for with and without CB models within the embedded CB zone

A comparison between the two models shows that the ultimate stress (485 MPa) on the area over which the CB was embedded, was 5% less than the ultimate stress (512 MPa) in the model without the embedded CB. Figure 4-6 shows the IRF distribution through the thickness of the laminate. As can be seen, the overall IRF in the model with the embedded CB is less than the model without the CB which indicates that the failure occurs slightly sooner in the model without the CB.

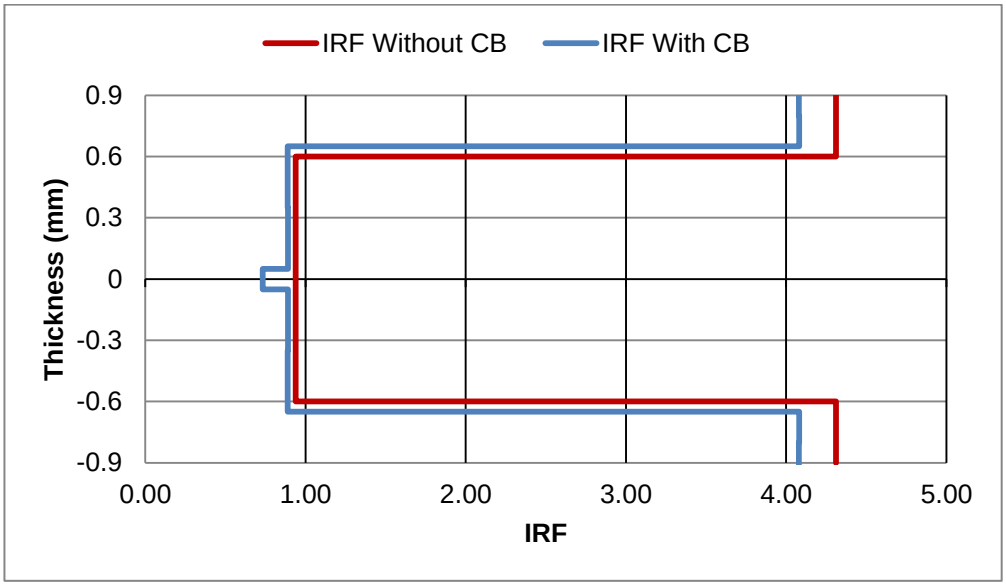

Figure 4-6: IRF distribution through the thickness of $[\pm 75_C/\pm 10_{FG}]_s$ hybrid laminate with and without CB models in the embedded CB zone

The reason for that result is because by adding 0.1mm thickness of CB to the layers of the laminate, the area increased and the stress decreased according to the stress equation:

$$\sigma = \frac{F}{A} \qquad (4.4)$$

Where,

σ = Stress (Pa)

F= applied load (N)

A= Area (m^2)

It can be argued from the results that most of the applied load would be shared by the fibre-glass, which in turn would protect the CB from failing.

4.1.3.1 Area on the interface between embedded CB and the host material

As can be seen in Figure 4-3 the red colour zones in the interface between the embedded CB and the host material have the highest stress zone than the rest of the sample. Therefore, the stress distribution, through the thickness of the laminate at the highest stress zone, is analysed by selecting the sampling element on the red zone as shown in Figure 4-7.

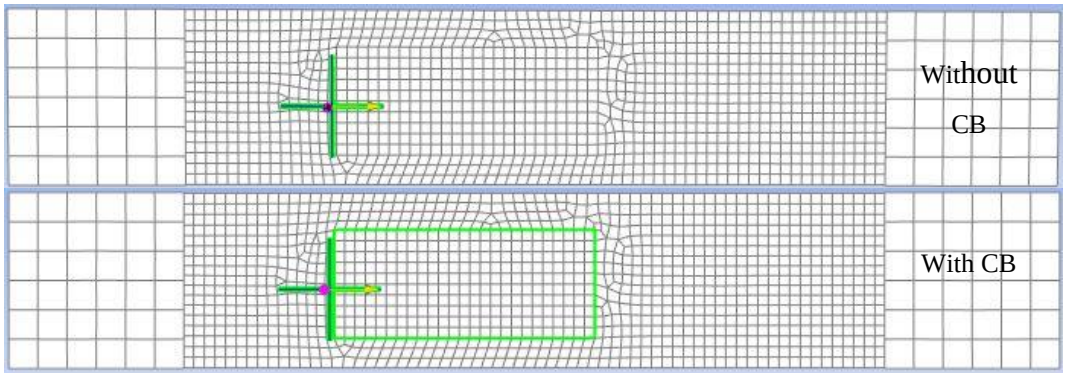

Figure 4-7: Selected sampling element on the models without and with embedded CB in the interface with the embedded CB

The results in Figure 4-8 indicates that the stress in the model with the CB increased 1.37% compared to the model without the CB. It is anticipated that the fibre angles of ±10° carried the primary load while the carbon fibre layers at ±75° carried the compressional load due to the Poisson effect. Figure 4-9 illustrates that there is 2% more chance to have a failure using glass-fibre layers compared to 1% using carbon fibre layers after embedding the CB.

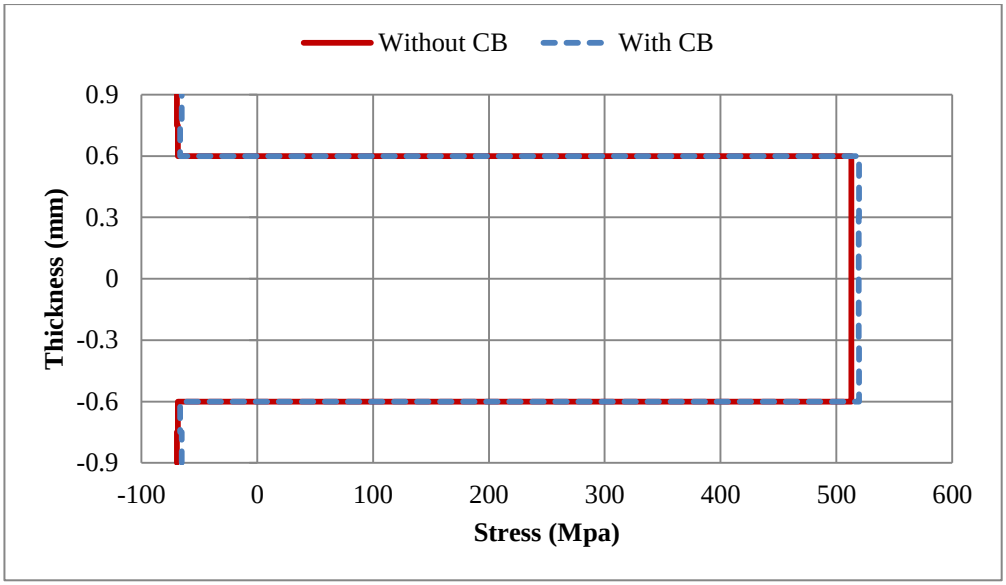

Figure 4-8: Ply-by-ply stress distribution through within the thickness $[\pm 75_C/\pm 10_{FG}]_s$ of hybrid laminate - with and without CB models in the interface with embedded CB

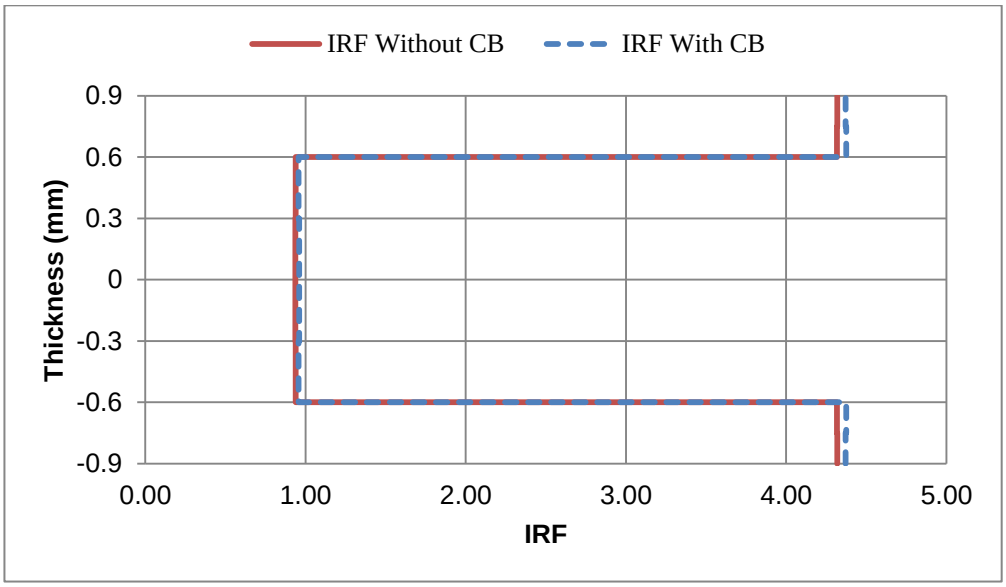

Figure 4-9: IRF distribution the thickness $[\pm 75_C/\pm 10_{FG}]_s$ of hybrid laminate with and without CB models on the interface with the embedded CB zone

In conclusion, a comprehensive comparison between the analyses of both models is shown in Table 4-2. According to ACP software manual, Interlaminar stresses are computed with the approach presented by Rohwer (1988) and Rolfes (1997). Inter-laminar stresses were described in the previous chapters and the main goal was to decrease the inter-laminar stresses to achieve an optimum laminate design.

The outcome of the analysis shows that S3 is zero since there is no load in the direction of 3. S13 and S23 (interlaminar stresses in plane directions of 13 and 23), the two main interlaminar stresses in the composite laminate, have values very close to zero after embedding the CB within the laminate. As was expected, by embedding the CB, the inter-laminar stresses appear at the edge of the CB but upon choosing a thin CB (0.1mm thickness), the negative effect of the CB on the mechanical properties of the host material becomes negligible.

Table 4-2: Details of each ply $[\pm 75_C/\pm 10_{FG}]_s$ flat hybrid composite subjected to tensile load for models with and without CB

Without CB										
			SE on embedded CB				**SE on the interface of CB**			
Material	**Angle (°)**	**Thickness (mm)**	**S1 (MPa)**	**S13 (MPa)**	**S23 (MPa)**	**IRF**	**S1 (MPa)**	**S13 (MPa)**	**S23 (MPa)**	**IRF**
Carbon/Epoxy	75	0.15	-68	0	0.E+00	4.32	-69	0.E+00	0.E+00	4.32
Carbon/Epoxy	-75	0.15	-68	3.E-26	5.E-26	4.32	-68	-7.E-27	5.E-26	4.32
Eglass/Epoxy	10	0.3	512	9.E-26	-5.E-26	0.94	513	9.E-26	2.E-26	0.94
Eglass/Epoxy	-10	0.3	512	3.E-25	2.E-26	0.94	513	2.E-25	9.E-26	0.94
Eglass/Epoxy	-10	0.3	512	3.E-25	2 E-26	0.94	513	2.E-25	9.E-26	0.94
Eglass/Epoxy	10	0.3	512	9.E-26	-5.E-26	0.94	513	9.E-26	2.E-26	0.94
Carbon/Epoxy	-75	0.15	-68	3.E-26	5.E-26	4.32	-68	-7.E-27	5.E-26	4.32
Carbon/Epoxy	75	0.15	-68	-2.E-42	-5.E-41	4.32	-69	2.E-41	-3.E-41	4.32
With CB										
			SE on embedded CB				**SE on the interface of CB**			
Material	**Angle (°)**	**Thickness (mm)**	**S1 (MPa)**	**S13 (MPa)**	**S23 (MPa)**	**IRF**	**S1 (MPa)**	**S13 (MPa)**	**S23 (MPa)**	**IRF**
Carbon/Epoxy	75	0.15	-63	0.E+00	0.E+00	4.08	-65	0.E+00	0.E+00	4.37
Carbon/Epoxy	-75	0.15	-64	-1.E-26	-1.E-25	4.08	-67	-2.E-25	-6.E-26	4.37
Eglass/Epoxy	10	0.3	485	-2.E-25	-1.E-27	0.89	520	-1.E-25	5.E-25	0.96
Eglass/Epoxy	-10	0.3	485	-7.E-25	-1.E-25	0.89	519	-9.E-25	3.E-25	0.96
Copper	0	0.1	501	-1.E-24	-4.E-26	0.73	-	-	-	-
Eglass/Epoxy	-10	0.3	485	-7.E-25	-1.E-25	0.89	519	-9.E-25	3.E-25	0.96
Eglass/Epoxy	10	0.3	485	-2.E-25	-1.E-27	0.89	520	-1.E-25	5.E-25	0.96
Carbon/Epoxy	-75	0.15	-64	-1.E-26	-1.E-25	4.08	-67	-2.E-25	-6.E-26	4.37
Carbon/Epoxy	75	0.15	-63	5.E-41	-2.E-40	4.08	-65	1.E-40	1.E-40	4.37

4.2 Experimental study of flat hybrid laminate

The objective of the experimental work was to validate the FEA analysis. This work was based on the relative comparison of hybrid samples that has no CB versus hybrid sample that has an embedded CB.

4.2.1 Specimen preparation

In order to avoid specimen preparation error, one large sample was fabricated which would allow multiple specimens to be cut from it. This will allow sample consistency, since the examined specimens will have the same preparation conditions, accordingly will possess similar physical properties. So the large sample was cut into smaller specimens for mechanical testing (Ameri et al., 2014). Each specimen had the dimensions of (300 x 50 x1.8mm). The CB was selected with a dimension of (75x31x0.1mm) without any electric component attachments to allow a match with FEA analysis. An axial strain gauge was attached to the CB as well. Figure 4-10 shows the details of the CB.

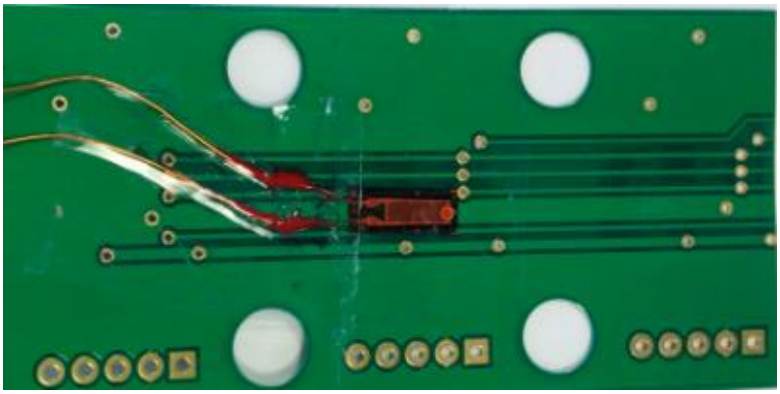

Figure 4-10: Details of the embedded circuit board within the hybrid laminate.

To obtain representative specimens of filament wound composite (FWC) with unit cells, a flat hybrid composite was fabricated by embedding a circuit board in the middle of the laminate. E-glass rovings SE1200, carbon-fibre T700s and Kinetix R246 epoxy resin were applied by hand lay-up in eight layers that are symmetrically balanced $[\pm 75_C/\pm 10_{FG}]_s$, as shown in Table 4-1. To hold the fibres in place, double sided sticky tape was used to apply tension on the fibre, in the same manner as applied during the filament winding process (Figure 4-11).

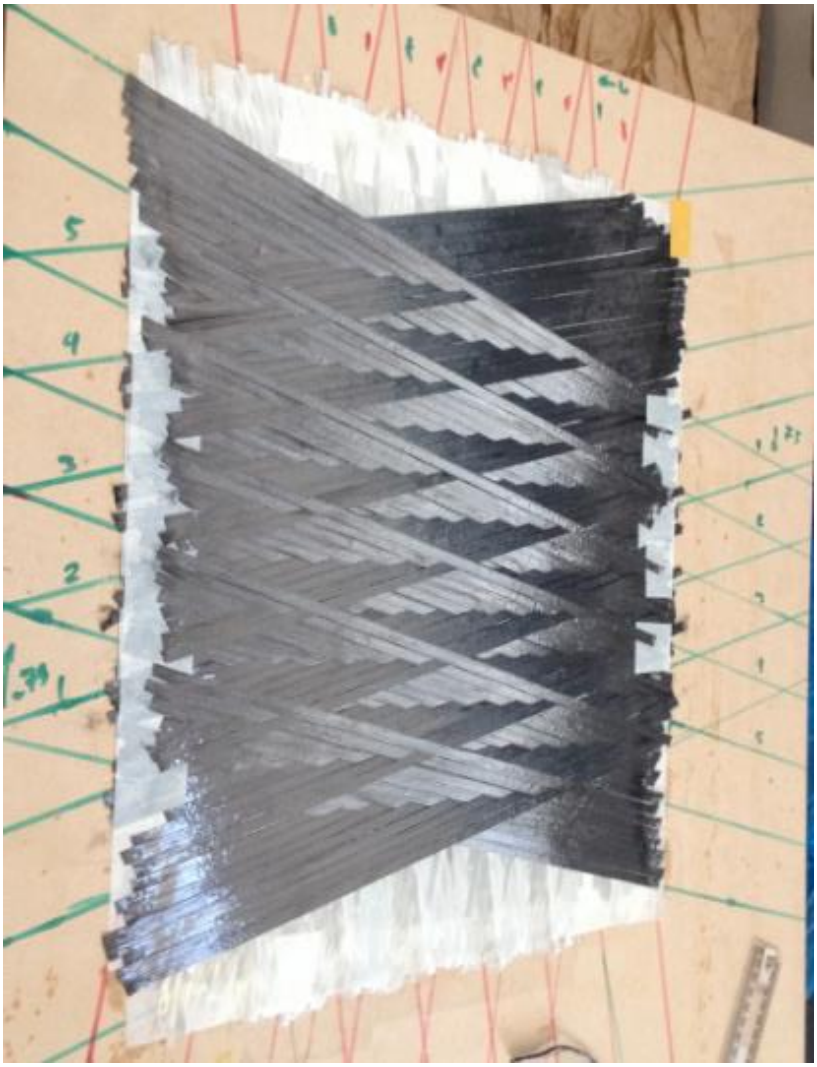

Figure 4-11: Using double sided tape to create $[\pm 75_C/\pm 10_{FG}]_s$ hybrid laminate before applying epoxy resin.

Each laminate ply was laid up by hand without using epoxy. Each unit cell included 16 and 20 roving fibres using carbon and glass fibres, as illustrated in Figure 4-12.

Figure 4-13 shows each layer contained two plies of negative and positive angles. The CB was placed in the middle of the laminate. The epoxy resin was applied on top of the last layer of the lay-up. Then a vacuum bagging technique was utilised to reduce the voids with a fixed vacuum pressure of -16 KPa for 6 hrs at 25° C. The hybrid composite panel was post-cured at room temperature for 48 hours. The final specimen panel is shown in Figure 4-14 which provides the location of the embedded CB as well.

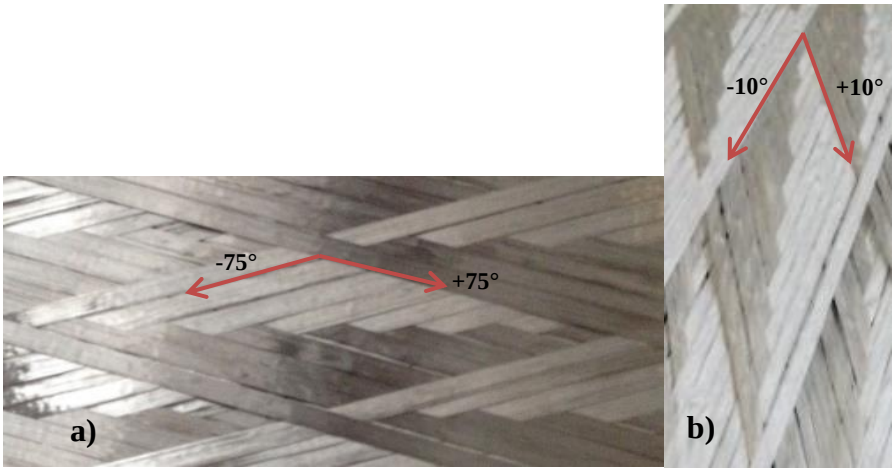

Figure 4-12: A flat specimen with a unit cell, a) Carbon fibre in ±75° direction, b) Glass fibre in ±10° direction

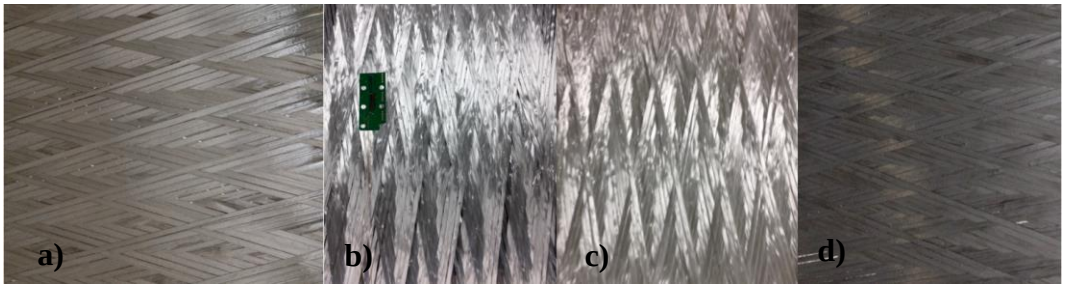

Figure 4-13: Dry flat specimens with FWC pattern in [$\pm75_C/\pm10_{FG}$] lay-up, a) Carbon fibres in ±75° b), Fibre-glass with embedded CB in ±10° c) Fibre-glass in ±10° d) Carbon fibres in ±75°

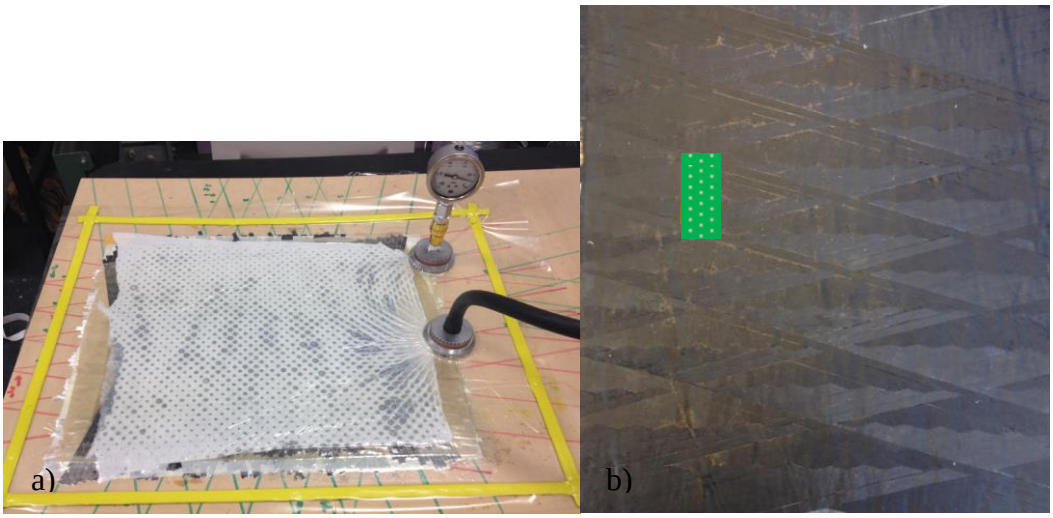

Figure 4-14: Final flat hybrid specimen a) vacuum bagging technique, b) the final specimen with embedded CB after the vacuum bagging process.

4.2.2 Tensile testing of a flat hybrid laminate

The specimens were cut using a water jet process to avoid delamination on the free edges, 50mm width and 300mm length following the axial direction (0°) of the unit cells, as shown in Figure 4-15. The cut specimens were prepared according to ASTM D3039 standard (ASTM, 2014a). Two specimens were selected for the tensile test, one with an embedded CB and the other without a CB.

Wedge grips were used to prevent gripping damage on the specimens. The aluminium tabs were prepared (50mm by 50mm and 3mm thickness) and attached to the specimen by a high-elongation (tough) epoxy adhesive.

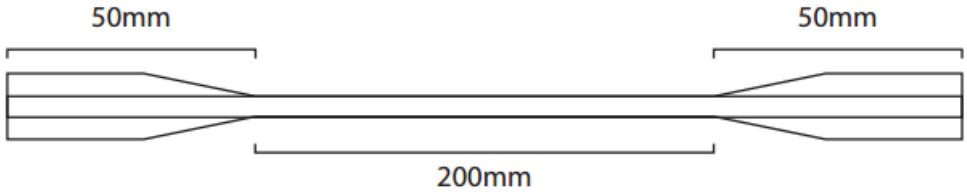

Figure 4-15: Tension test specimen drawing with aluminium tabs

In order to record the strain data, TML strain gauges were attached on the middle section of each specimen. The gauge length and resistance were 5mm and 350±1.0 Ω respectively. Surface preparation of flat hybrid specimens was done according to (ASTM, 2014b). The gauge locations for each specimen are shown in Figure 4-16.

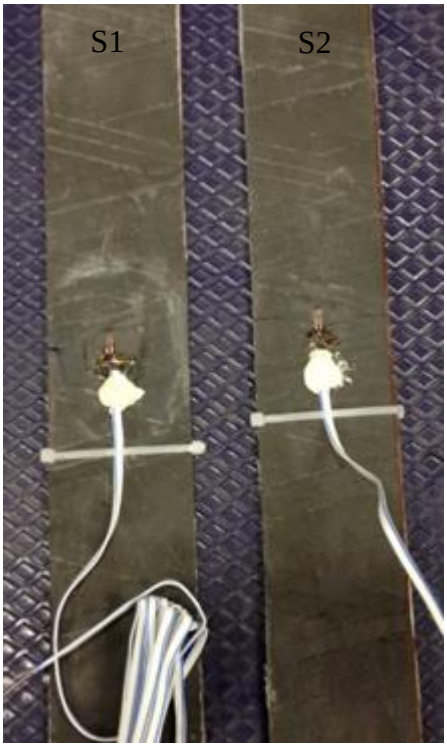

Figure 4-16: Strain gauge location for flat hybrid specimens

Table 4-3 shows the measured physical properties of hybrid composites such as fibre and matrix volume fraction. The specimen density of the hybrid composites was determined using method II of the American Society for Testing and Materials (ASTM) D3171-11 (ASTM, 2013) and it was assumed that void fraction was zero. The mechanical properties of hybrid composite specimens are shown in Table 4-3. The tensile tests were performed according to the ASTM D3039 standard (Figure 4-17) (ASTM, 2014a). The load was applied at a rate of 1.27 mm/min.

Figure 4-17: The front and side view of tensile machine during application of tensile load on a specimen

Table 4-3: Physical and mechanical properties of flat hybrid composite specimens

	Specimen	**S1-with CB**	**S2**
Physical properties	**Composite density ρ (gr/cm^3)**	1.53	1.53
	Matrix volume fraction V_m	0.299	0.299
	Fibre volume fraction V_f	0.701	0.701
	Thickness(mm)	1.8	1.8
Mechanical properties	**Ultimate tensile strength σ (N/mm^2)**	488	512
	Strain Ɛ (με)	17168.85	16026.18
	Elastic modulus E (MPa)	0.028	0.031
	Ultimate tensile load (KN)	44.5	46.1

4.2.3 Tensile test results

The stress-strain plot for specimens, with and without a CB, is shown in Figure 4-18. The ultimate tensile strength of specimen S2 (the specimen without the CB) is approximately 4.7% more than S1 (the one with the CB). The trends of graphs are linear and represent fibres with a rigid matrix. This suggests that the applied load may be shared mostly across the fibres rather than the matrix so when the stresses on the fibres reach the fibre's tensile strength, failure will occur (Harris, 1999).

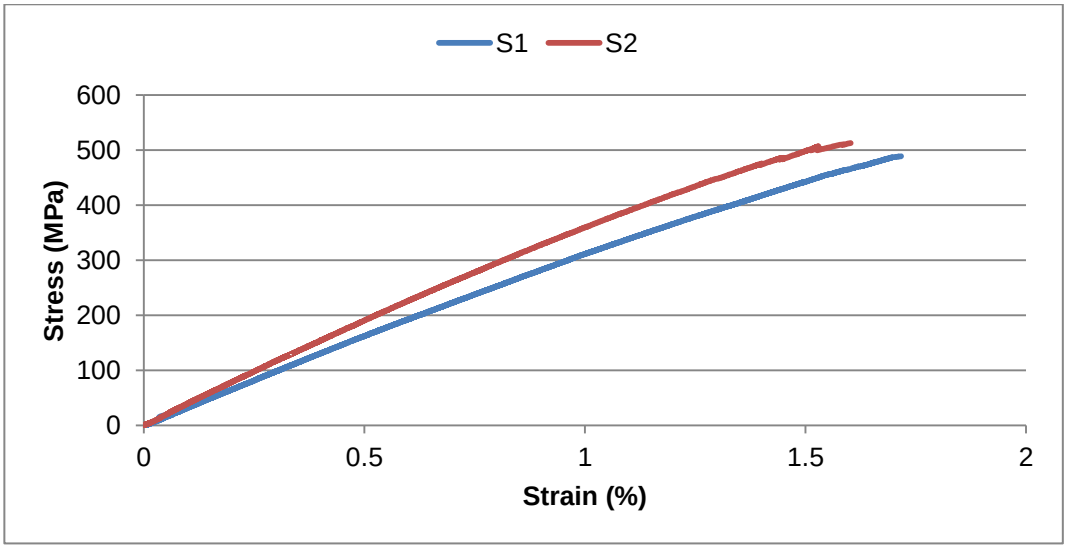

Figure 4-18: Stress –strain graph of two specimens with CB (S1) and without CB (S2)

Specimen S1 with CB had two strain gauges. One strain gauge was attached to the CB on the mid-layer of the specimen. Figure 4-19 shows that the ultimate tensile strain on the outer layer (17168.85με) was 11% more than the ultimate tensile strain on the CB (15254.83με).

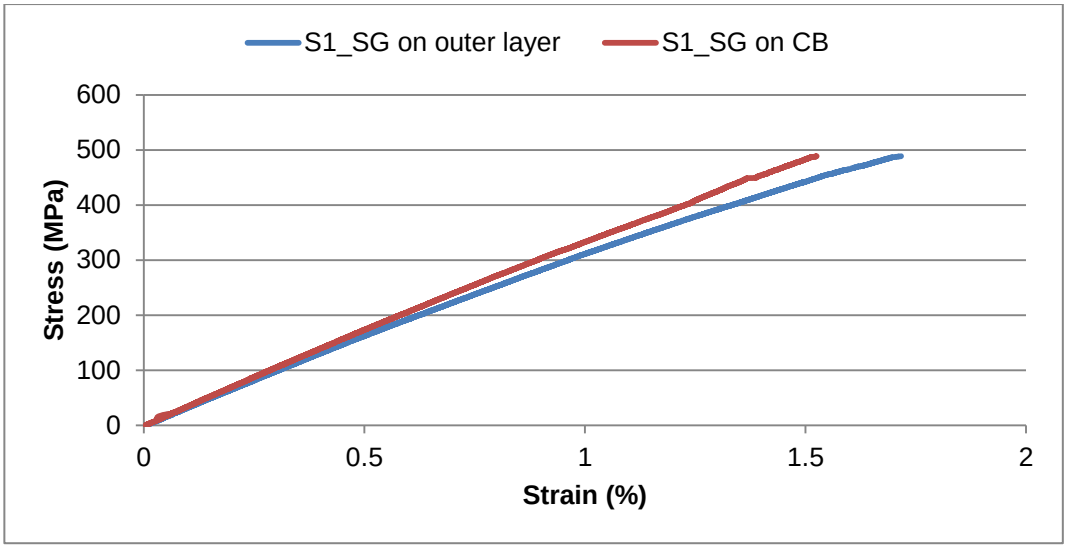

Figure 4-19: Specimen with CB and two strain gauges (SG) on outer layer and on CB

It was observed that when the tensile load was applied to the specimen, the carbon fibre layers in ±75° direction started matrix cracking before the final failure occurred. Both specimens' failure mode was visually examined. Figures 4-20 and 4-21 show delamination at the interface between the carbon fibre and glass fibre rather than at the centre of the glass fibre. The kink effect on both specimens demonstrates that the carbon fibre was orienting itself towards the direction of the loading and rotating along the glass fibre angle (±10°) of orientation. The kink effect indicates that the fibre-glass was carrying the primary load at the beginning of the test until the carbon fibres give way and fail in the kink direction due to the Poisson effect (Ameri et al., 2014).

The experimental study indicated that most of the applied load was shared by the fibre-glass layers, which in turn would protect the CB from failing.

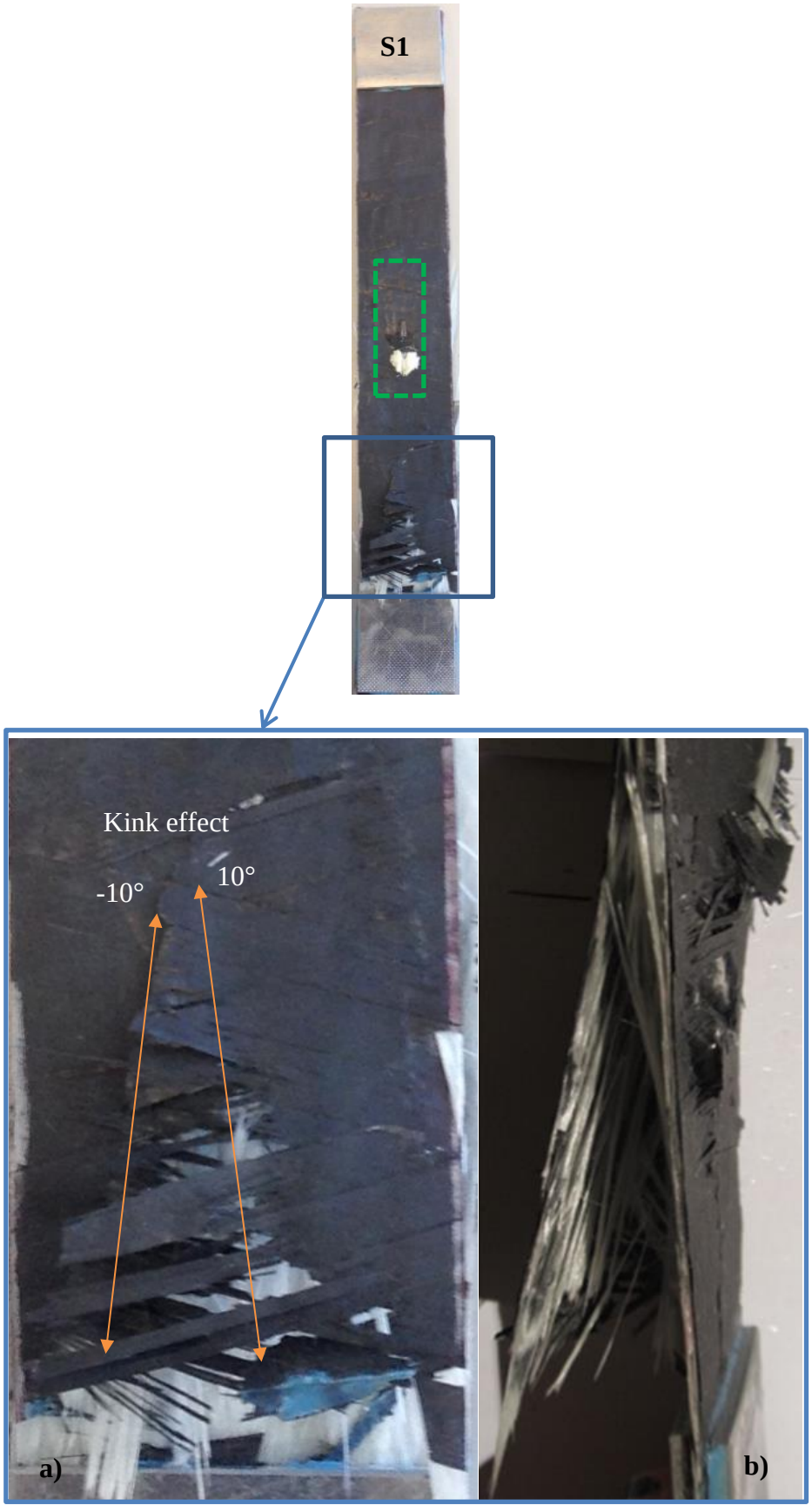

Figure 4-20: Specimen with CB and zoomed failure section, a) Kink effect in front side, b) Delamination in side view

Figure 4-21: Specimen without CB and zoomed failure section, a) Kink effect in front side, b) Delamination in side view.

4.3 FEA and experimental results

By comparing the results between FEA analysis and experimental work, it can be noted that they have good agreement. Tables 4-2 and 4-3 indicate that the ultimate tensile strength for the specimen without the CB is matched and for a specimen with a CB the difference is only 0.6%, which can be within acceptable experimental tolerance.

Since the initial failure occurred in carbon fibre layers for both specimens, the experimental work validated the results obtained by FEA analysis, in terms of IRF, as shown in Figures 4-6 and 4-9. It can also be observed from the results that the fibre-glass layers were bearing the primary load.

The results show that the CB was embedded into these hybrid composites with minimal deterioration to the hybrid composite's structural strength.

4.4 FEA of tube hybrid composite

The good agreement between the FEA of a flat hybrid composite and experimental work proved the reliability of the ACP simulation. Therefore the rest of the study focused on numerical analysis. One of the significant questions that can be raised is, whether analysis of a flat specimen model can represent the cylindrical or tube models? To answer this question, two tube geometries with $[(\pm 75)_C/(\pm 10)_{FG}]_S$ laminate lay-up in eight plies were created with and without an embedded CB, assuming the same criteria used as that for the flat hybrid composite model. Then, a unidirectional load was applied in the axial direction of the tube, with zero loads in Y and Z directions. Similar analysis was performed on flat geometry with the same cross-sectional dimensions and laminate lay-up. Finally, the results of the tube and the flat geometry were compared.

4.4.1 Tube hybrid composite model without CB

4.4.1.1 Tube geometry without embedded CB

The tube geometry was created using the dimensions shown in Table 4-4. The dimensions were based on the most common tube size used in exploration diamond drilling (NQ size). The tube consists of a lay-up $[(\pm 75)_C/(\pm 10)_{FG}]_S$ using eight plies without the CB. A unidirectional tensile load of 136KN was applied in

the axial direction of the tube as shown in Figure 4-22. The loads in the hoop direction were zero as the model was only subjected to unidirectional tensile load.

Table 4-4: The dimensions of the tube geometry

OD (mm)	ID (mm)	Thickness (mm)	Length (mm)	Cross-section Area (mm^2)
70.3	66.7	1.8	800	387.36

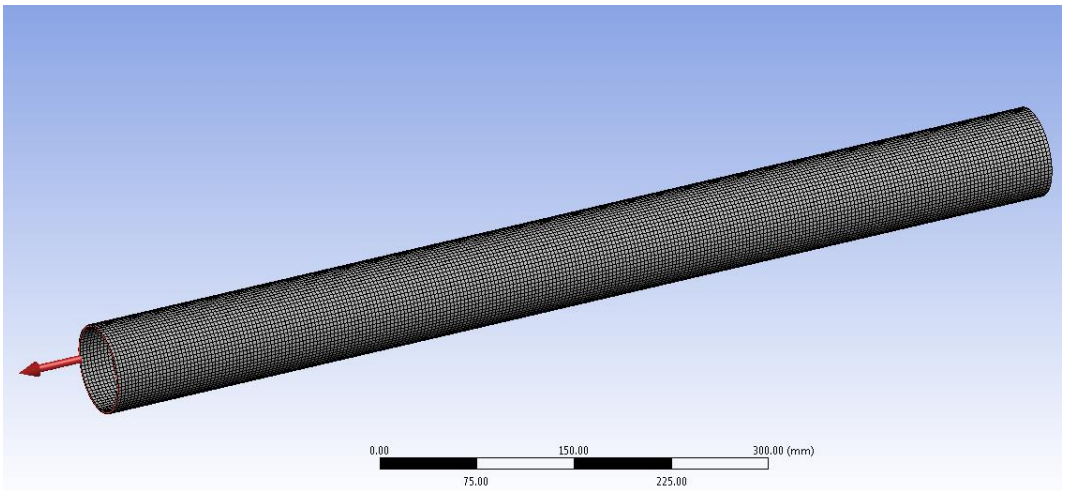

Figure 4-22: Tube model without embedded CB subjected to applied tensile load

4.4.1.2 Stress Analysis and results

The stress distribution was analysed ply-by-ply through the tube hybrid laminate. The contour plots illustrating the stress distribution for each ply after applying the load on the tube geometry are shown in Figure 4-23. The details of each ply are shown in Table 4-5, where it was noted that the fibre-glass layers carried the primary tensile load, while the carbon-fibre layers were subjected to compressional load due to the Poisson effect. The IRF for each ply demonstrates that carbon fibre layers failed before the final failure occurs in the model. Results are in agreement with ACP simulation and experimental work observations.

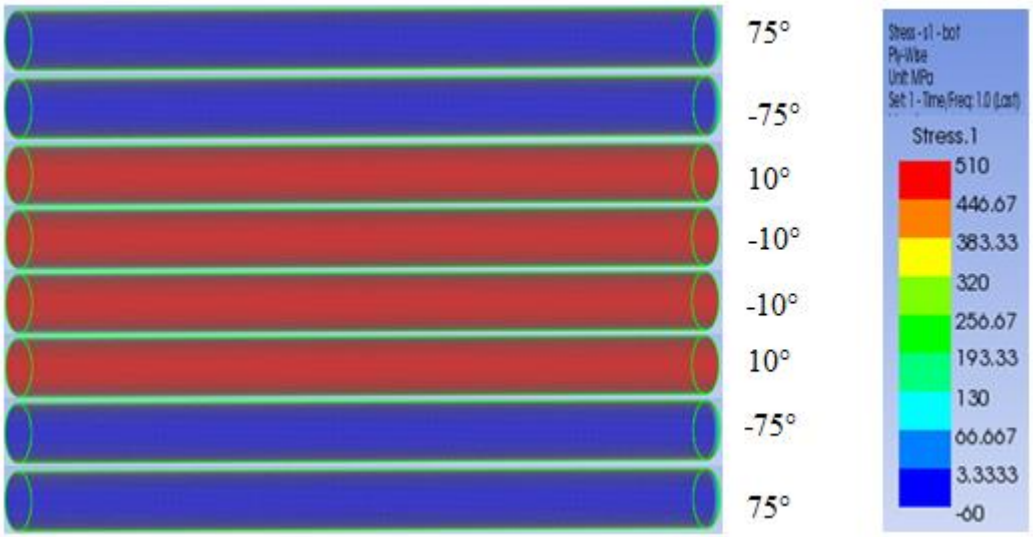

Figure 4-23: Contour plot in of tube hybrid composite without embedded CB after applied load for each ply

Table 4-5: Details of each ply $[\pm 75_C/\pm 10_{FG}]_s$ tube hybrid composite

Fibre	Thickness (mm)	Angle (°)	Stress (Mpa)	IRF
Carbon	0.15	75	-63	3.9
Carbon	0.15	-75	-63	3.9
Glass	0.3	10	476	0.7
Glass	0.3	-10	476	0.7
Glass	0.3	-10	476	0.7
Glass	0.3	10	476	0.7
Carbon	0.15	75	-63	3.9
Carbon	0.15	-75	-63	3.9

4.4.2 Tube converted to the flat model without CB

4.4.2.1 Flat geometry without embedded CB

The tube geometry was converted to a flat shape using the dimensions in Table 4-6, in which the cross-sectional area is constant for both geometries of the tube and the flat model. Since the thickness is fixed, the lay-up $[(\pm 75)_C/(\pm 10)_{FG}]_S$ hybrid laminate creates a width of 215.2mm.

Table 4-6 Dimensions of the flat geometry

Length mm	Width mm	Thickness mm	Cross-section Area mm^2
800	215.2	1.8	387.36

Figure 4-24 shows the cross-sectional view of the tube compared to the flat geometry. Following equation (4.4), the stress applied to the laminate is the force per unit area applied to the laminate. The objective of this simulation was to prove that by selecting the constant unidirectional tensile load and constant cross-sectional area, the stress distribution through the hybrid laminate should be equal for both tube and flat, geometries.

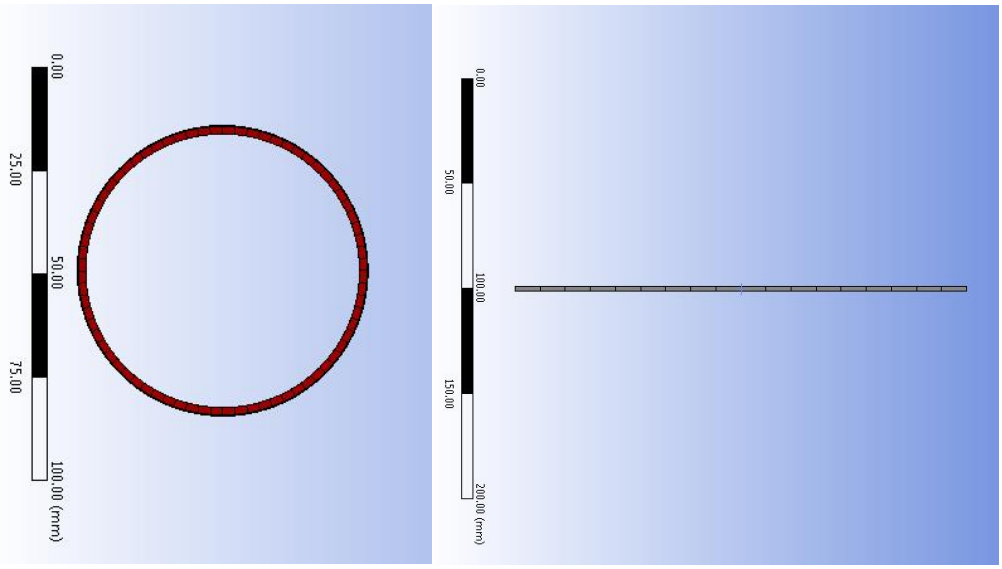

Figure 4-24: Converting the tube geometry to the flat geometry by keeping the cross-sectional area equal for both

The flat geometry was based on the $[(\pm 75)_C/(\pm 10)_{FG}]_S$ hybrid laminate composite. A unidirectional tensile load of 136KN was applied in the axial direction of the flat geometry as shown in Figure 4-25. Y and Z directions were not subjected to any loads.

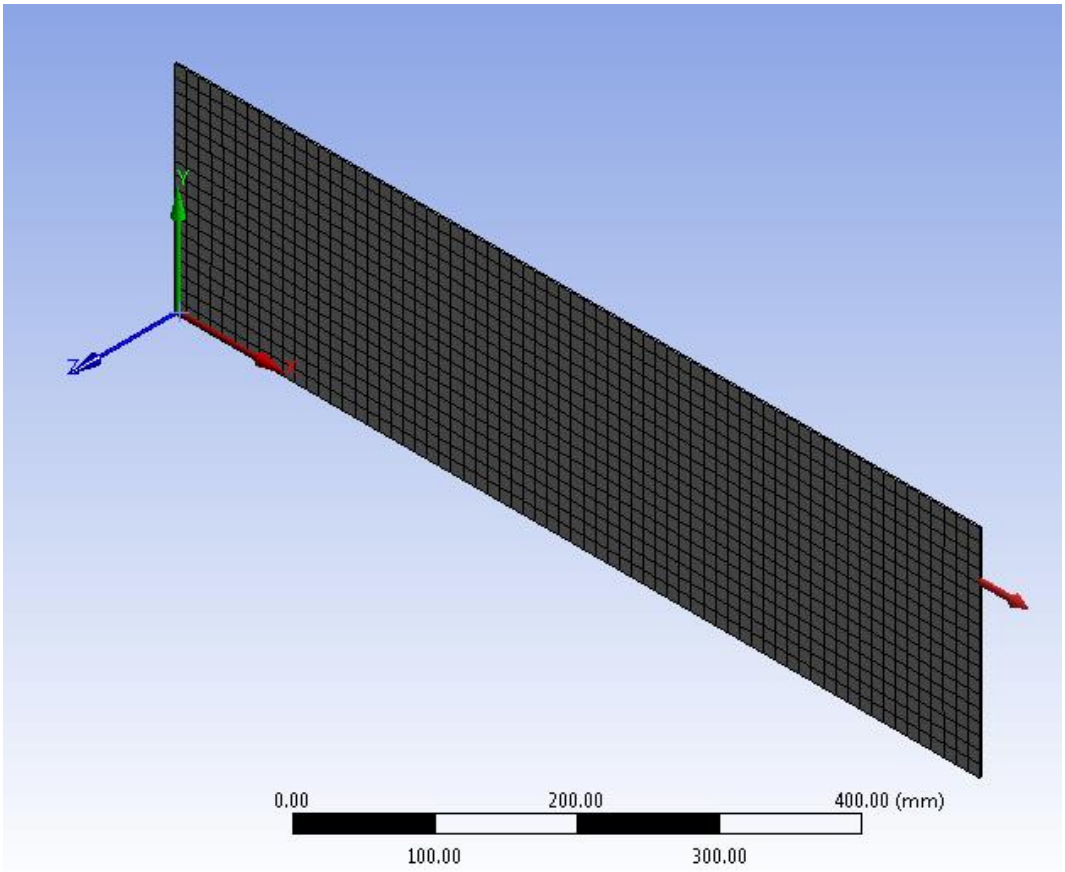

Figure 4-25: Geometry of flat hybrid composite subjected to a unidirectional tensile load

4.4.2.2 Stress analysis and results

The stress distribution through a hybrid flat laminate was simulated ply-by-ply, and the results were the same as the previous simulations. The fibre-glass layers were carrying the primary tensile load while the carbon fibres layers were subjected to compressional load because of the Poisson effect. The counter plot demonstrates the results as shown in Figure 4-26. The details of each ply are listed in Table 4-7, with IRF values for each ply showing that the failure started within the carbon fibre layers.

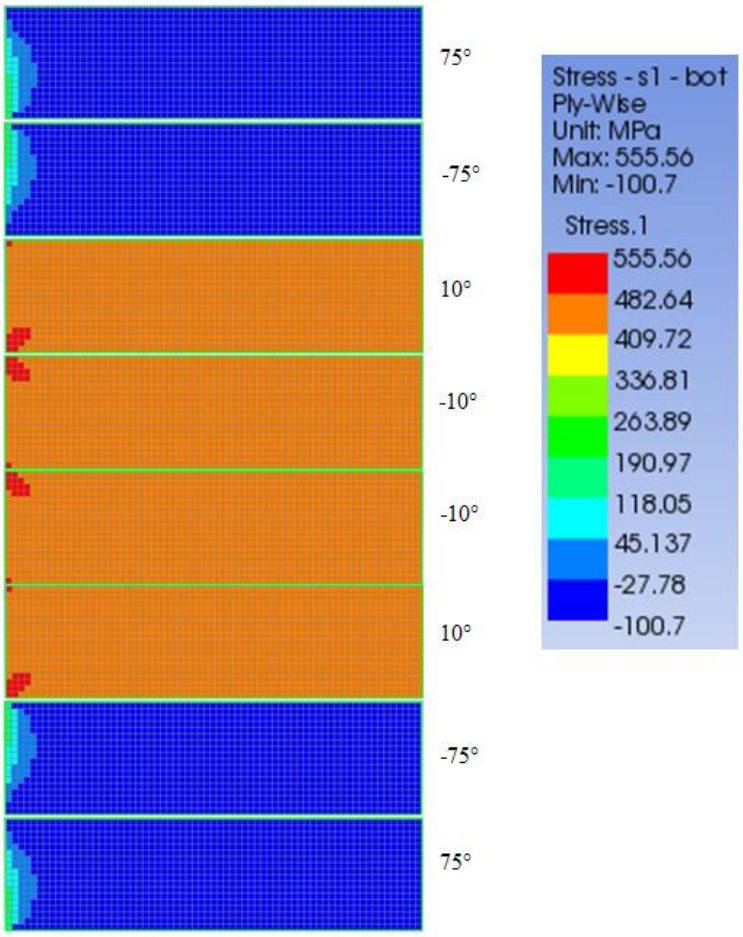

Figure 4-26: Contour plot in flat hybrid composite without embedded CB subjected to tensile load

Table 4-7: Details of each ply in [±75C/±10FG]s tube converted to flat hybrid composite

Fibre	Thickness (mm)	Angle (°)	Stress (MPa)	IRF
Carbon	0.15	75	-63	4.0
Carbon	0.15	-75	-63	4.0
Glass	0.3	10	476	0.9
Glass	0.3	-10	476	0.9
Glass	0.3	-10	476	0.9
Glass	0.3	10	476	0.9
Carbon	0.15	75	-63	4.0
Carbon	0.15	-75	-63	4.0

4.4.3 Results comparison between tube and flat models without CB

Figure 4-27 describes the stress distribution through the thickness of $[(\pm 75)_C/(\pm 10)_{FG}]_S$ laminate subjected to 136KN unidirectional tensile load for both tube and flat models. It is obvious from the graphs that when the tube geometry was converted to a flat geometry, the stress distribution through the hybrid laminate remained unchanged. In addition, the role of carbon fibre layers and fibre-glass layers for both tube and flat geometry was the same. The carbon fibre layers carry the compressional stresses and the fibre-glass layers bear the tensile stresses.

The Tsai-Hill criterion (section 2.3.3) was utilised to analyse the failure of both tube and flat models as the results through the thickness are demonstrated in Figure 4-28. When analysing the results, it was noted that the chance of failure of carbon fibre layers in a flat geometry was 2.5% more than for the tube geometry as well as the fact that the failure rate occurred in fibre glass layers with the flat geometry 22% higher than the tube geometry. It was mentioned in Chapter 2 that the free edge may lead to a depletion of the load carrying capability of the composite structure. The flat geometry has free edges, which increase the stress concentration due to interlaminar structure and leads to failure. On the other hand, the tube geometry does not have those free edges. Therefore, the tube geometry has an advantage over the flat geometry due to less interlaminar stress concentrations. However, both tube and flat geometries had failure initiation through the carbon fibre layers due to compressional stresses while the final failure was because of tensile stress through fibre glass layers.

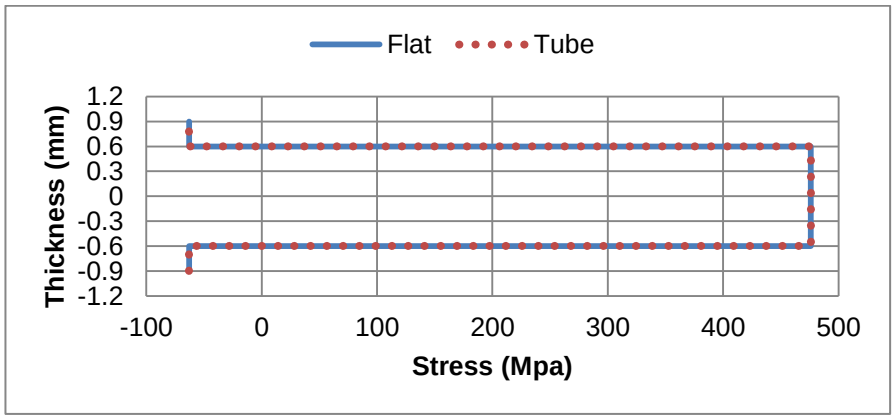

Figure 4-27: Ply-by-ply stress distributions through tube and flat hybrid composite models

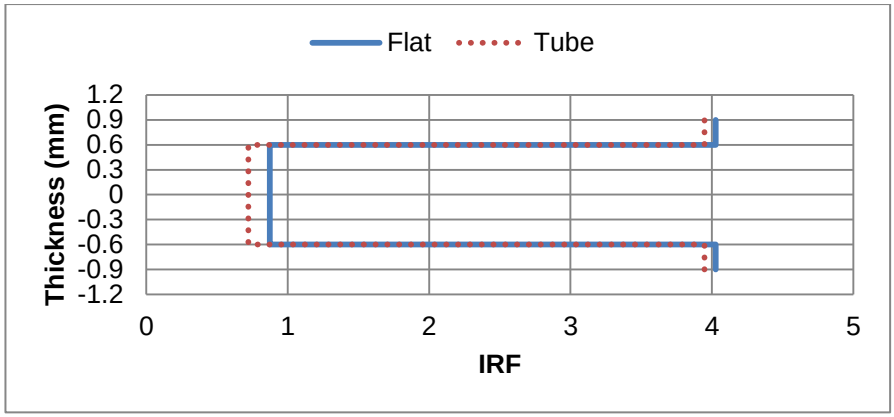

Figure 4-28: Ply-by-ply IRF through the thickness of tube and flat hybrid composite models

4.4.4 Tube and flat models with embedded CB

Section 4.4.3 explained the relationship between the tube and flat geometries, and it was noted that the flat geometry could represent the tube geometry, as they are equal in stress distribution and failure concepts. The objective of this section is to show that by embedding the CB geometry within $[(\pm 75)_C/(\pm 10)_{FG}]_S$ laminate layers, the results for both the tube and the flat geometries would be equivalent.

The CB was added to the tube and flat geometries with the following dimensions 75x31x0.1mm (the same as section 4.1.2). The dimensions of the tube and flat geometries are listed in Tables 4-4 and 4-6.

The unidirectional tensile load of 136KN was applied to both geometries. The stress distribution analyses were also done on both geometries as shown Figures 4-29 and 4-30.

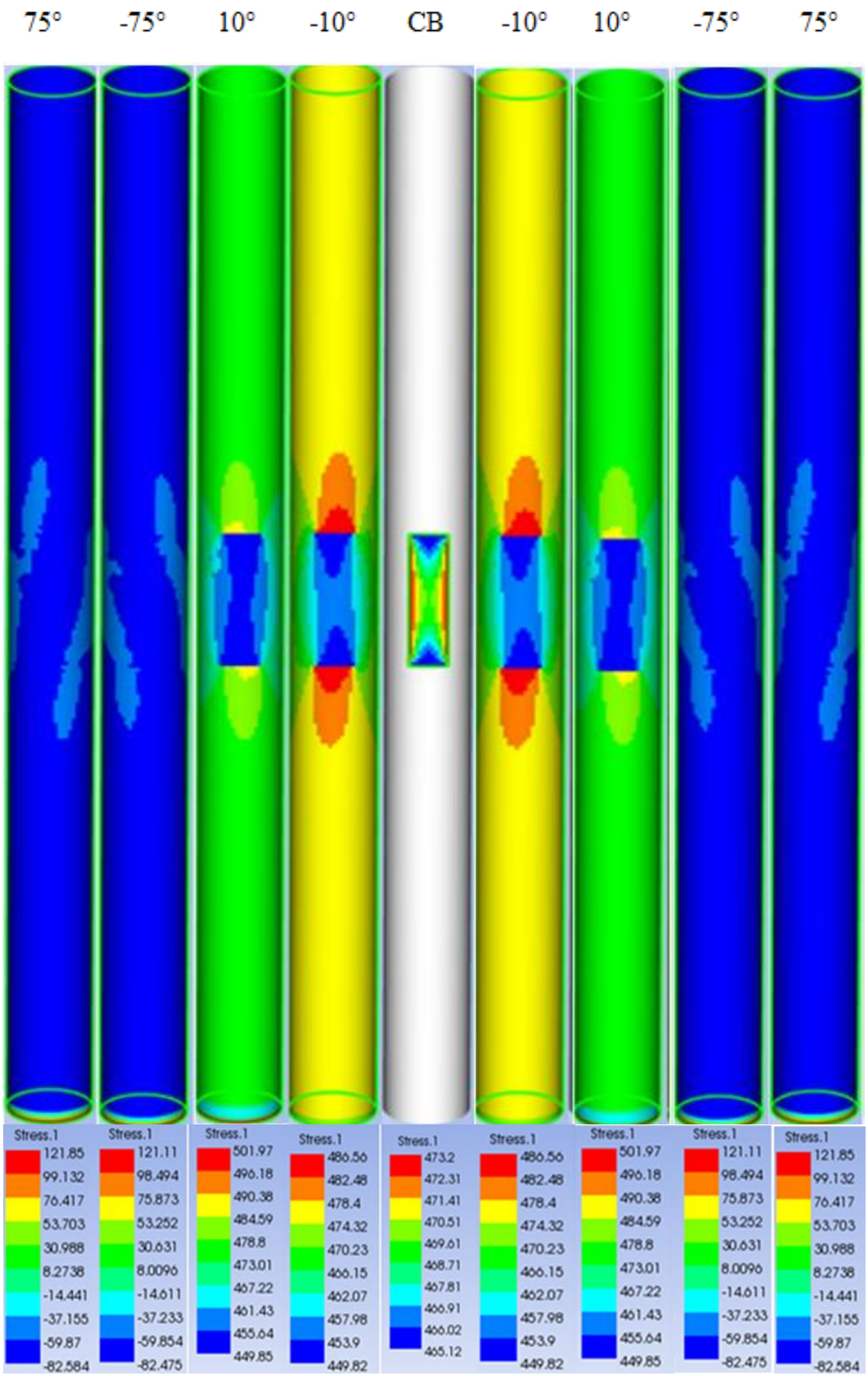

Figure 4-29: Contour plot of stress distribution through tube hybrid composite with embedded CB subjected to tensile load

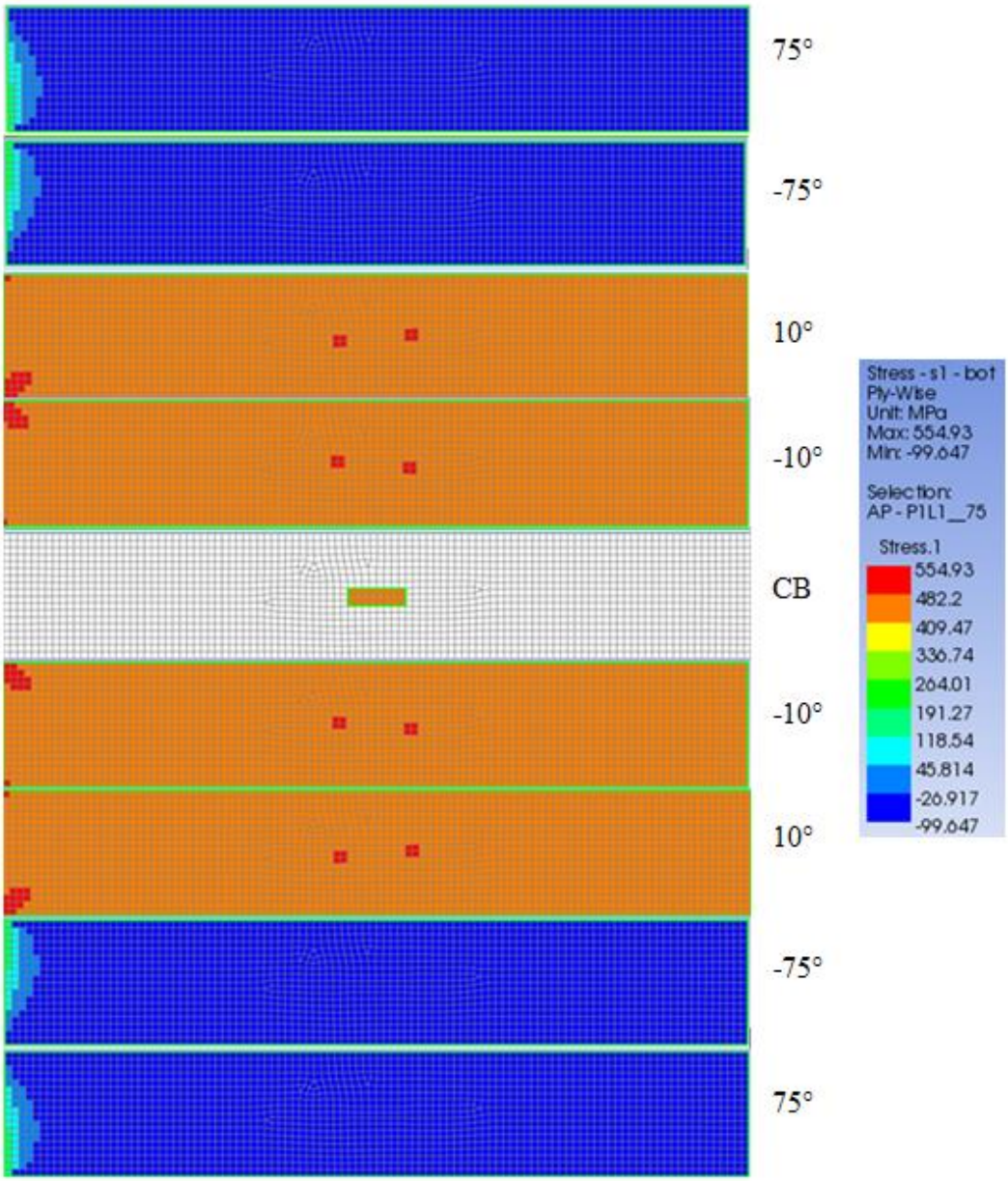

Figure 4-30: Contour plot of stress distributions through flat hybrid composite with embedded CB subjected to tensile load

4.4.5 Comparison of results between tube and flat models with embedded CB

The contour plots in Figures 4-29 and 4-30 show the stress distributions ply-by-ply through the thickness of $[(\pm 75)_C/(\pm 10)_{FG}]_S$ hybrid laminate for the tube and flat models. The stress analysis around the embedded CB shows that the stress changes slightly at the interface between the CB and the host material. Therefore, two zones were selected as in sections 4.1.3.1 and 4.1.3.2 to investigate the stress concentrations.

4.4.5.1 Location of embedded CB for tube and flat models

In order to examine the stress concentrations at the location of the embedded CB, a sampling element was selected for both the tube and the flat geometries as indicated in Figure 4-31. The details of stress analysis and failure analysis for the selected element on the embedded CB are mentioned in Table 4-8.

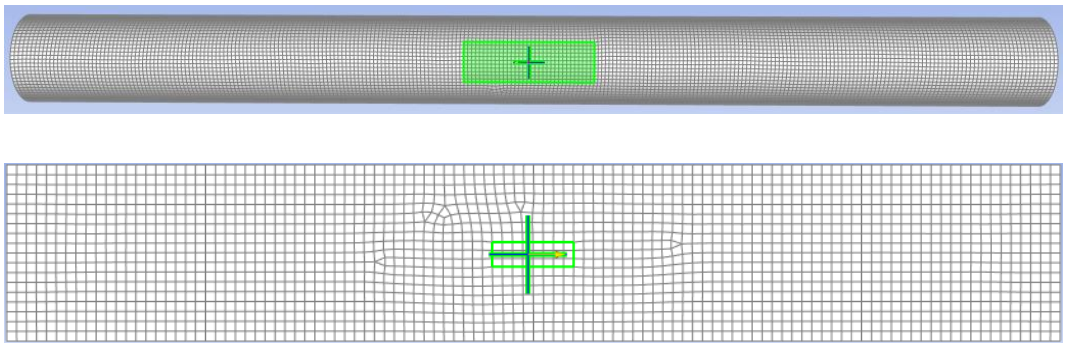

Figure 4-31: Location of sample elements for tube and flat models on embedded CB

The comparison between stresses on the tube versus flat models (Figure 4-32) shows that the response from both models is the same after the applied tensile load. However, the carbon fibre layers in the flat model carried 15% less stress than the tube model while the fibre-glass layers in the flat model carried 1.8% more stress than the tube model. The stress on the layer with an embedded CB in the flat model is 1.7% more than the tube model. Regardless of those stress differences, the failure analysis for both models is almost the same as illustrated in Figure 4-33. The values of IRF in the fibre-glass layers are similar for the tube and the flat models but the IRF values for carbon fibre layers in the flat model are 1.5% more than IRF values in the tube model.

In conclusion, while the geometries are different for the tube and the flat models, both reacted similarly and it is noted that the model geometry and stress distributions for a laminate composite are not related.

Table 4-8: Details of stress and failure analysis at the location of an embedded CB for the tube and flat geometries

			Tube		Flat	
Fibre	**Thickness (mm)**	**Angle**	**Stress**	**IRF**	**Stress (MPa)**	**IRF**
Carbon	0.15	75	-70	3.86	-60	3.92
Carbon	0.15	-75	-70	3.86	-60	3.92
Glass	0.3	10	455	0.85	463	0.85
Glass	0.3	-10	455	0.85	463	0.85
CB	0.1	0	470	0.68	478	0.70
Glass	0.3	-10	455	0.85	463	0.85
Glass	0.3	10	455	0.85	463	0.85
Carbon	0.15	75	-70	3.86	-60	3.92
Carbon	0.15	-75	-70	3.86	-60	3.92

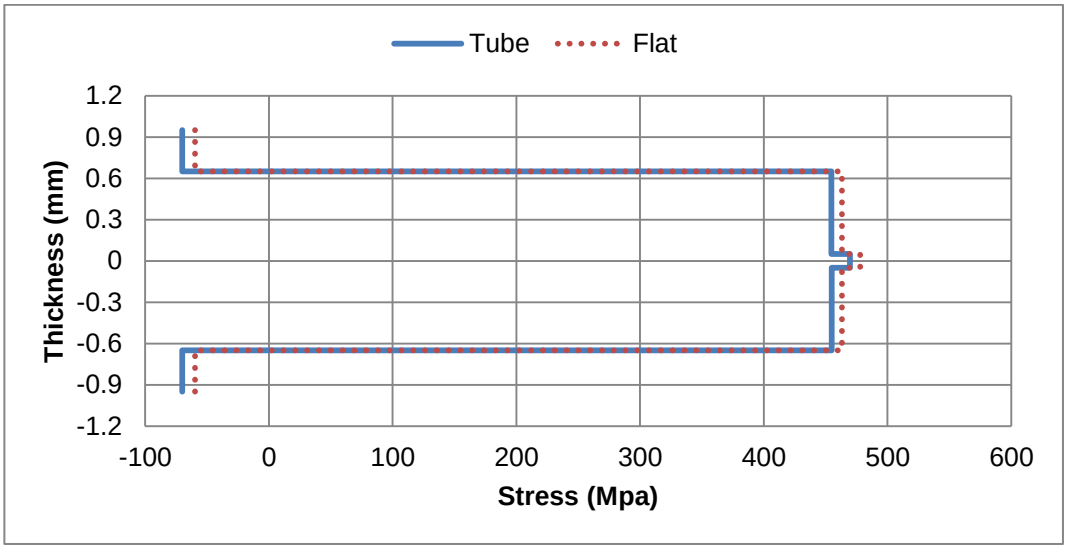

Figure 4-32: Stress analysis through a thickness of $[(\pm75)_C/(\pm10)_{FG}]_S$ laminate at the location of embedded CB for the tube and flat geometries

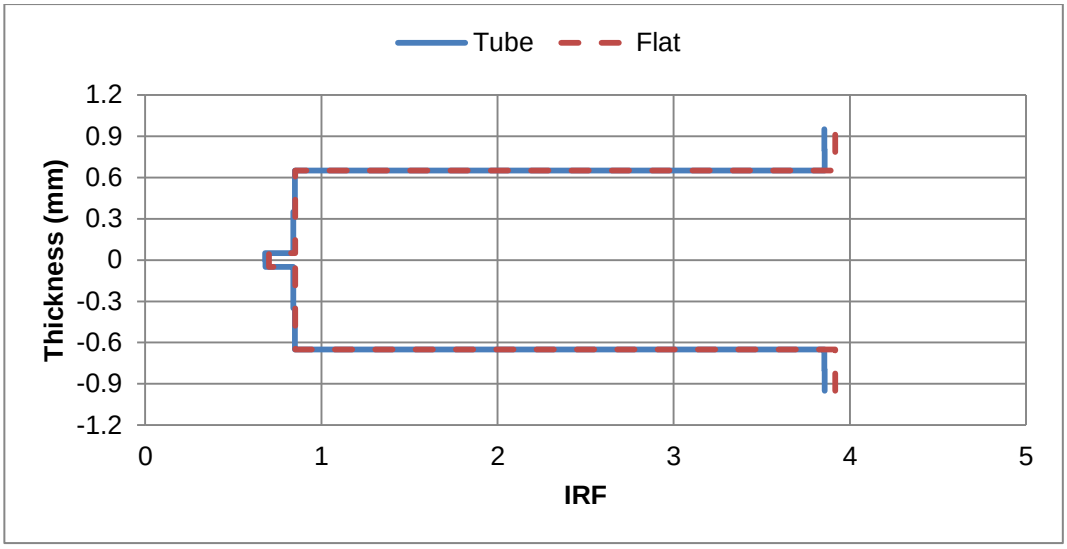

Figure 4-33: Failure analysis through the thickness of $[(\pm75)_C/(\pm10)_{FG}]_S$ laminate at the location of an embedded CB for the tube and flat geometries

4.4.5.2 Interface between embedded CB and the host material for tube and flat models

From Figures 4-29 and 4-30, the interfaces between an embedded CB and the hybrid composite material accommodate the maximum stress for both models. The sample elements for the tube and the flat models were chosen according to Figure 4-34, through the thickness of the hybrid composite $[(\pm75)_C/(\pm10)_{FG}]_S$.

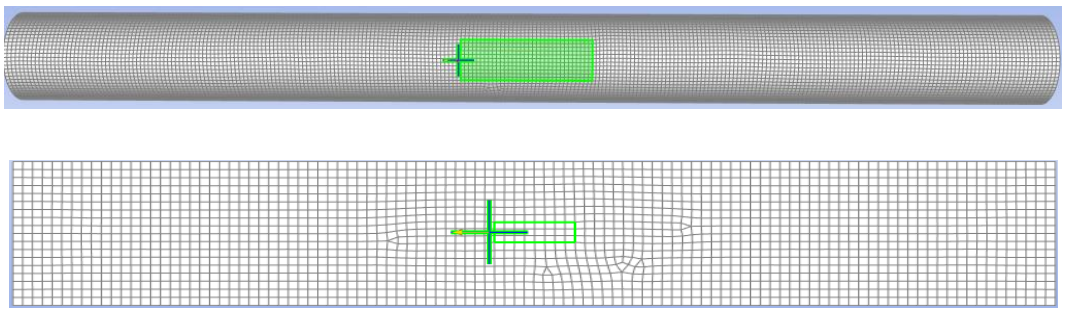

Figure 4-34: Location of sample elements for tube and flat models at the interface between embedded CB and the host material

The details of stress and IRF values for each ply in the sample element are in Table 4-9. The stresses and IRF for the tube and flat models at the interface between an embedded CB and the hybrid composite are illustrated in Figures 4-35 and 4-36 respectively. Comparison of the stresses reveals similar stress

distribution values for both models. The stress values for the flat model are less than 1% greater than the stress values in the tube model. Also the IRF values are very close to IRF values for the tube.

In summary, the results of stress and failure analysis for both models at the interface between an embedded CB and the hybrid composite have good agreement.

Table 4-9: Details of stress and failure analysis on the interface between embedded CB and the hybrid composite for the tube and flat geometries

			Tube		Flat	
Ply	**Thickness (mm)**	**Angle (°)**	**Stress (MPa)**	**IRF**	**Stress (MPa)**	**IRF**
Carbon	0.15	75	-63	4.11	-63	4.14
Carbon	0.15	-75	-63	4.11	-63	4.14
Glass	0.3	10	485	0.91	489	0.90
Glass	0.3	-10	485	0.91	489	0.90
Glass	0.3	-10	485	0.91	489	0.90
Glass	0.3	10	485	0.91	489	0.90
Carbon	0.15	75	-63	4.10	-63	4.14
Carbon	0.15	-75	-63	4.10	-63	4.14

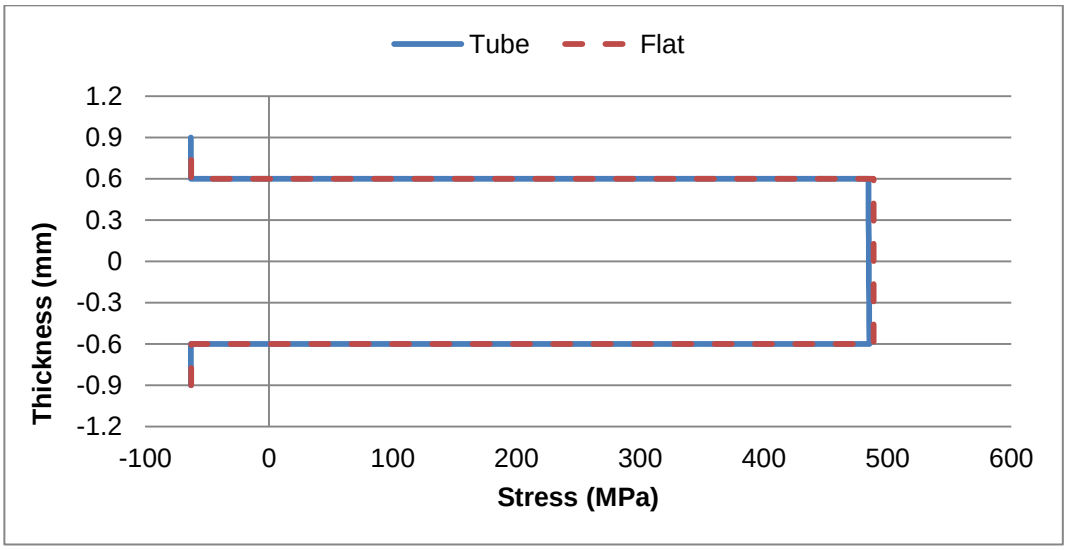

Figure 4-35: Stress analysis through the thickness of $[(\pm 75)_C/(\pm 10)_{FG}]_S$ laminate at the interface between embedded CB and the hybrid composite for the tube and flat geometries

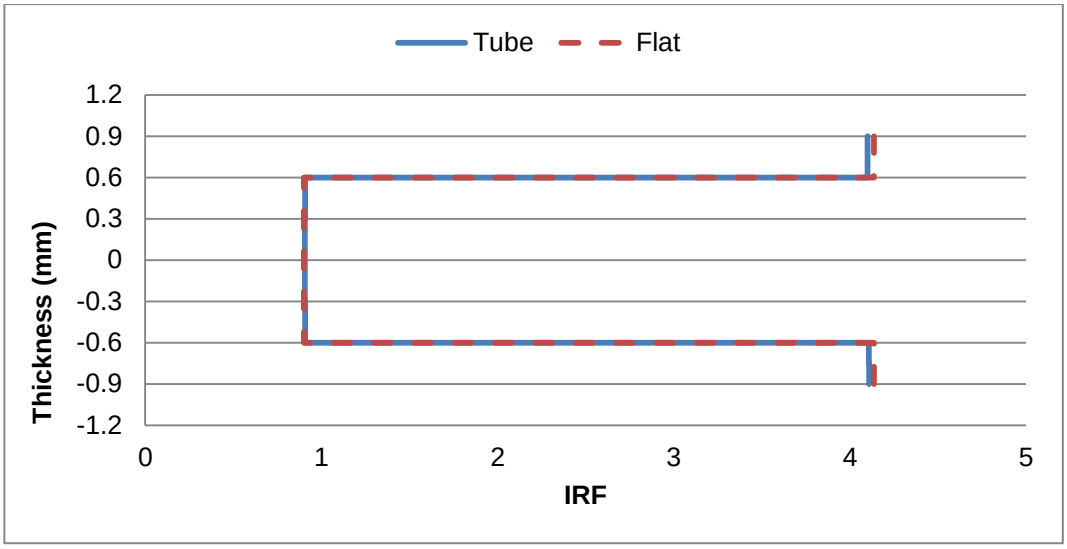

Figure 4-36: Failure analysis through the thickness of $[(\pm75)_C/(\pm10)_{FG}]_S$ laminate at the interface between embedded CB and the hybrid composite for the tube and flat geometries

4.5 Chapter conclusions

In this chapter, two flat hybrid composites (carbon/glass and epoxy) in a $[(\pm75)_C/(\pm10)_{FG}]_S$ lay-up and eight plies using a filament winding pattern, with and without an embedded circuit board, were simulated and tested to determine their mechanical performance. The effect of an embedded CB on the host material was investigated numerically as well as experimentally.

Numerical simulation analysis utilised ANSYS ACP software and the fabricated samples validated the findings. Then, the mechanical properties of the fabricated samples were evaluated by means of a tensile test.

The results from FEA analysis showed that the ultimate stress (485 MPa) on the area in which the CB was embedded, was 5% less than the ultimate stress (512 MPa) of the model without an embedded CB. In addition, by choosing the thin CB (0.1mm thickness) the negative effect of a CB on the mechanical properties of a host material became negligible. The IRF results demonstrated that failure occurs within the carbon fibre layers sooner than the fibre-glass layers due to the Poisson effect when applying tensile load.

The results from the experimental work indicated that the ultimate tensile strength and modulus of elasticity of the specimen containing the embedded CB was about

4.7% and 9.7% less than the specimen without the embedded CB, respectively. It was noted that the failure occurred at approximately 43mm away from the location of the CB. Therefore, it can be argued that by designing low angle fibres surrounding an embedded CB, most of the applied load will be shared by the fibre-glass layers, which in turn would protect the CB from failing.

After validating numerical simulation analysis, further study was performed on the tube geometry. Two models were created to confirm that the flat model can represent the tube geometry. It was assumed that the applied tensile load and cross-sectional area for both models were equal. Therefore, the tube geometry was converted to a flat geometry. Comparing the stress distributions through the thickness of $[(\pm 75)_C/(\pm 10)_{FG}]_S$ laminates for both models revealed a similarity between them. It can be argued that embedding a CB within a composite material would be independent of the geometry of the host material. Parameters like the thickness of the CB and the size ratio of an embedded CB and host material could be more effective, and consequently the next chapter will examine the effect of CB size on the hosting structure.

In conclusion, the study showed that low angle glass-fibres controlled the applied load, which was transmitted to the carbon fibres until complete failure occurred. The failure mode was verified both theoretically and experimentally, where the failure was initiated as delamination at the interface between the fibre-glass and the carbon fibre. Based on these results, the numerical modelling was in good agreement with the experiments. The CB was embedded into the hybrid composites with minimal deterioration of the hybrid composite's structural strength.

5 SENSITIVITY ANALYSIS OF CB SIZE ON COMPOSITE STRUCTURAL STRENGTH

The relationship between the size of an embedded circuit board (CB) with the host material is the focus of this chapter. Two types of sensitivity were investigated in the research. The first sensitivity analysis was the area ratio of the CB area to the area of the host material (area sensitivity). The second sensitivity analysis was the thickness variation effect of the embedded CB within the hybrid composite (thickness sensitivity).

5.1 Area sensitivity

One of the uncertainties about embedding a CB within the composite material was the ratio of the CB area to the area of the host material. The FEA which was used to analyse the area sensitivity was based on the flat model in section 4.4.2.

Table 5-1 details of dimensions and area ratio (CB:host) of four different models

	Host Material				CB				
Description	**Width (mm)**	**Length (mm)**	**Area (mm^2)**	**Ratio L:W**	**Width (mm)**	**Length (mm)**	**Area (mm^2)**	**Ratio L:W**	**Area Ratio CB: Host**
Original - Flat Sample	50	300	15000	6	30	100	3000	3.3	20%
Tube converted to Flat	215.2	1291.2	277864	6	130	432	55964	3.3	20%
Tube converted to Flat - with Original CB dimension	215.2	1291.2	277864	6	30	100	3000	3.3	1%
Tube converted to Flat - with area ratio of 5%	215.2	1291.2	277864	6	65	215	13893	3.3	5%
Tube converted to Flat - with area ratio of 10%	215.2	1291.2	277864	6	91	304	27786	3.3	10%

The model geometry in section 4.1.2 was considered to be the baseline and referred to as the "original". As described in Table 5-1, four models were created according to the area ratios 1%, 5%, 10% and 20%. The laminate lay-up was followed by $[(\pm 75)_C/(\pm 10)_{FG}]_S$. The ratio of length to width for the host material (6) and the CB (3.3) were constant in all models and the area for the host material was constant. The load and boundary conditions were equalised for four model options. The area ratio was the only variable in the simulations.

5.1.1 Stress analysis and results

In order to evaluate the results between the models, contour plots of stress distribution through the laminate plies were generated for each area ratio. Figures 5-1, 5-2, 5-3 and 5-4 show the contour plots for area ratios 20%, 1%, 5% and 10% respectively. It is noted from the plots that the wider the CB width, the greater the increased in stress concentrations (red colour elements) at the interface of the CB with the host material, however the values of stress were equal for all.

In summary, as can be seen in the figures, the fibre glass layers carried the primary tensile load while the carbon fibre layers carried the compressional load.

An analysis of the models was based on a comparison by considering equally selected elements (coordinate point) for all models in two different zones. The first zone was at the location of the embedded CB and the second zone was at the interface between the CB and the host material.

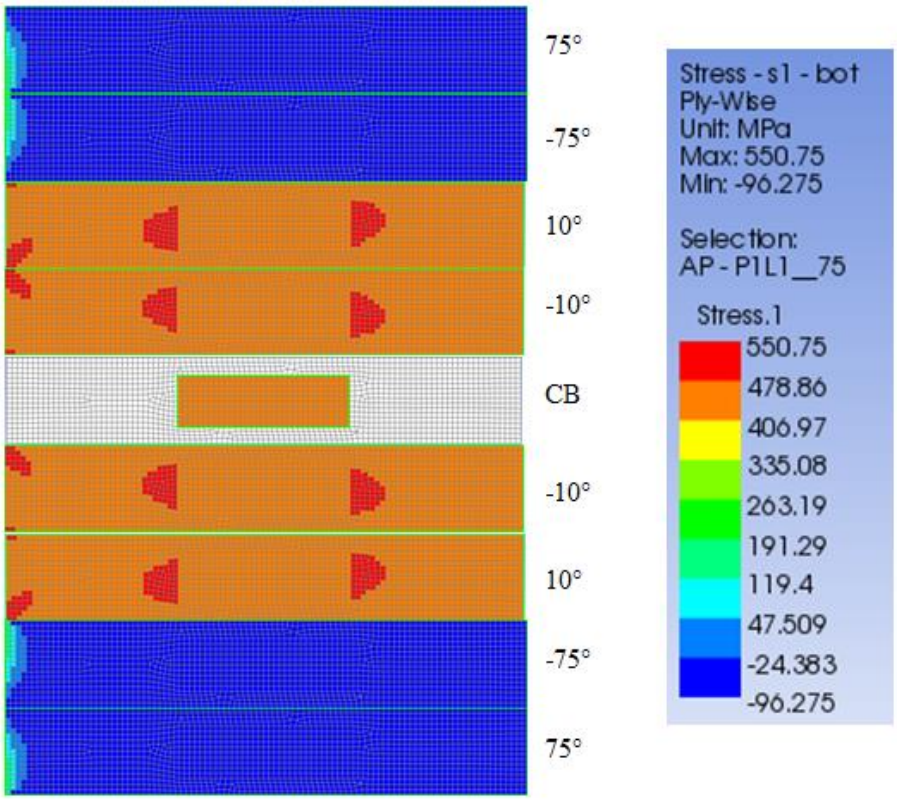

Figure 5-1: The contour plot of stress distribution through $[(\pm 75)_C/(\pm 10)_{FG}]_S$ laminate with an area ratio CB: host of 20%

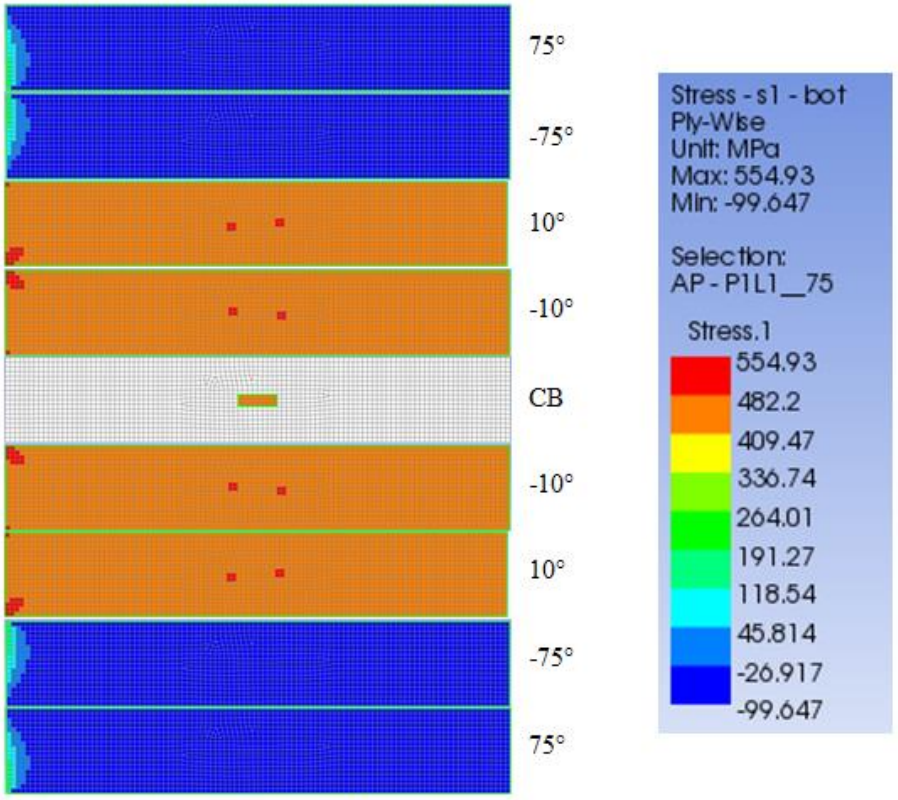

Figure 5-2: The contour plot of stress distribution through $[(\pm 75)_C/(\pm 10)_{FG}]_S$ laminate with an area ratio CB: host of 1%

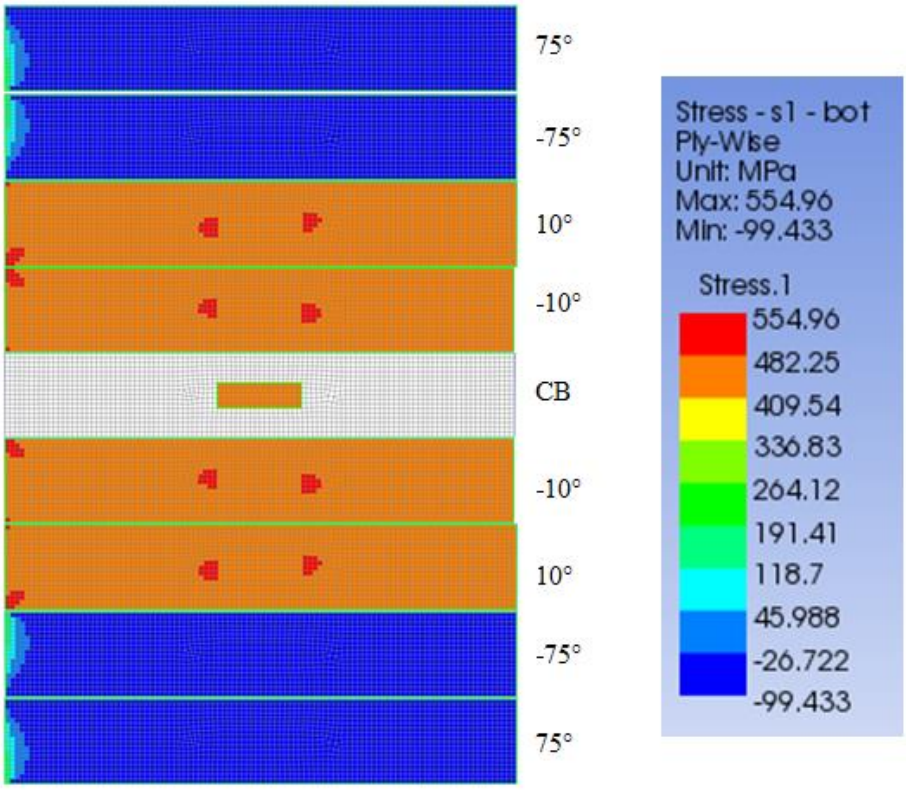

Figure 5-3: The contour plot of stress distribution through $[(\pm 75)_C/(\pm 10)_{FG}]_S$ laminate with an area ratio CB: host of 5%

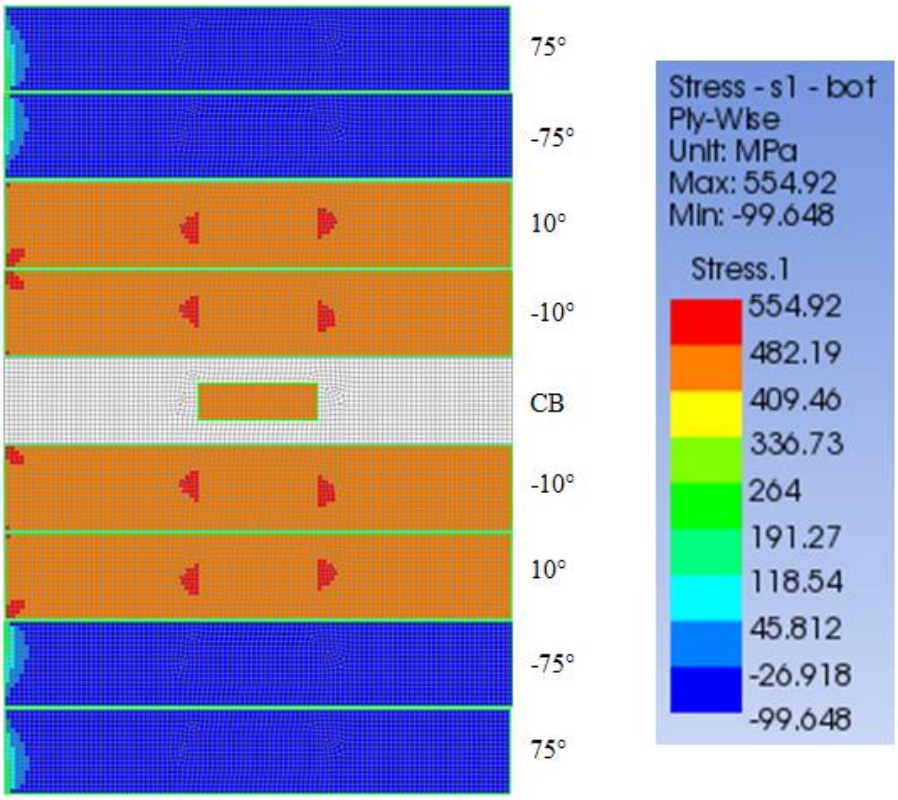

Figure 5-4: The contour plot of stress distribution through $[(\pm75)_C/(\pm10)_{FG}]_S$ laminate with an area ratio CB: host of 10%

5.1.1.1 Analysis of area sensitivity at the location of an embedded CB

A sample element was selected at the location of the embedded CB for all models with an equal coordinate point as shown in Figure 5-5. It was noted from a comparison of stress distribution and IRF within the $[(\pm75)_C/(\pm10)_{FG}]_S$ laminate layer between the models that the size of the embedded CB did not affect the strength of the hybrid composite laminate.

Figure 5-6 and Table 5-2 describe the stress analysis ply-by-ply through the laminate layer. By increasing the size of the embedded CB, the compressional stresses were identical in the carbon fibre layers and slightly different (less than 1% difference) in the fibre glass layers. As a result, it can be concluded that the changes between the models with a different area ratio were not significant.

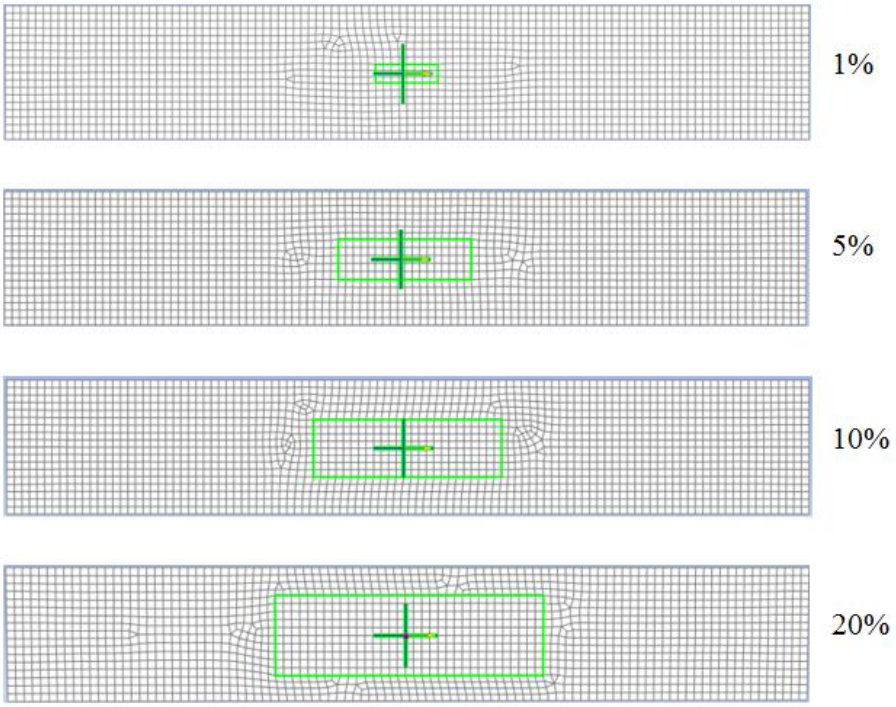

Figure 5-5: Selected sample element at the location of embedded CB in four different models with area ratios of CB: host of 1%, 5%, 10% and 20%

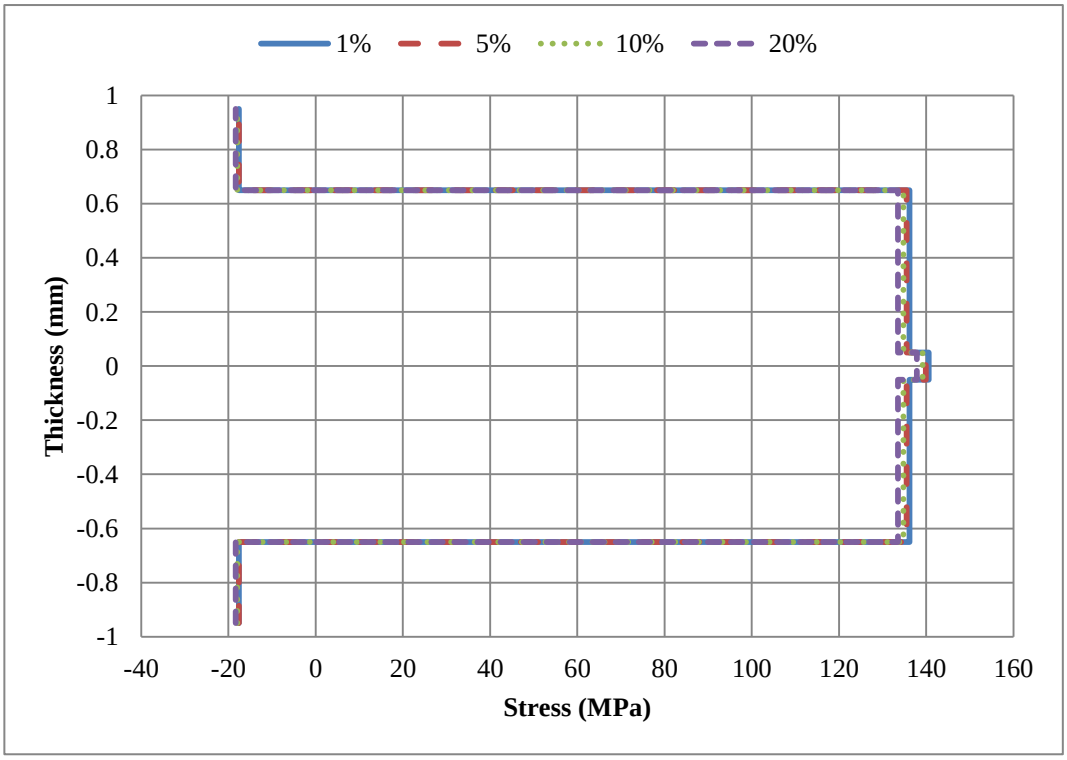

Figure 5-6: Ply-by-ply stress analysis through the $[(\pm 75)_C/(\pm 10)_{FG}]_S$ laminate layer at the location of the embedded CB for models with an area ratios of 1%, 5%, 10% and 20%

Table 5-2: Details of stress analysis through the $[(\pm75)_C/(\pm10)_{FG}]_S$ laminate layer at the location of embedded CB for models with area ratios of 1%, 5%, 10% and 20%

			Stress (MPa)			
Ply	**Thickness (mm)**	**Angle (°)**	**1%**	**5%**	**10%**	**20%**
Carbon	0.15	75	-18	-18	-18	-18
Carbon	0.15	-75	-18	-18	-18	-18
Glass	0.3	10	136	136	135	134
Glass	0.3	-10	136	136	135	134
CB	0.1	0	141	140	139	138
Glass	0.3	-10	136	136	135	134
Glass	0.3	10	136	136	135	134
Carbon	0.15	-75	-18	-18	-18	-18
Carbon	0.15	75	-18	-18	-18	-18

The details of failure analysis ply-by-ply through the thickness of the laminate layer are illustrated by Figure 5-7 and Table 5-3. It was observed that the response of the Inverse Reserve Factor (IRF) for each ply was indistinguishable. As the values greater than one deal with failure and less than one are safe, the IRF values in the carbon fibre layers were almost identical and the responses from all models showed the failure would happen initially in the carbon fibre layers with the value of around 1.1. while the IRF values in the fibre glass layers (0.2) indicated that the layers would respond in a very similar manner for the various area ratios.

Table 5-3: Details of failure analysis through the $[(\pm75)_C/(\pm10)_{FG}]_S$ laminate layer at the location of embedded CB for models with area ratios of 1%, 5%, 10% and 20%

			IRF			
Ply	**Thickness (mm)**	**Angle (°)**	**1%**	**5%**	**10%**	**20%**
Carbon	0.15	75	1.2	1.1	1.1	1.1
Carbon	0.15	-75	1.2	1.1	1.1	1.1
Glass	0.3	10	0.3	0.2	0.2	0.2
Glass	0.3	-10	0.3	0.2	0.2	0.2
CB	0.1	0	0.2	0.2	0.2	0.2
Glass	0.3	-10	0.3	0.2	0.2	0.2
Glass	0.3	10	0.3	0.2	0.2	0.2
Carbon	0.15	-75	1.2	1.1	1.1	1.1
Carbon	0.15	75	1.2	1.1	1.1	1.1

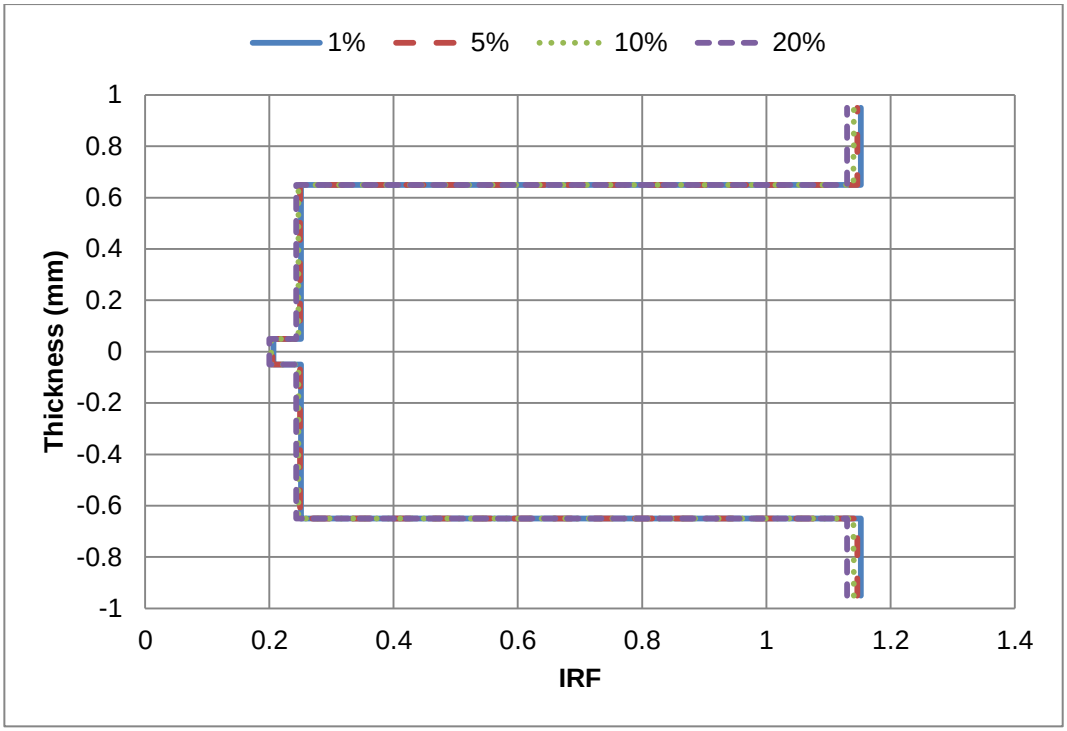

Figure 5-7: Ply-by-ply failure analysis through the $[(\pm75)_C/(\pm10)_{FG}]_S$ laminate layer at the location of embedded CB for models with area ratios of 1%, 5%, 10% and 20%

5.1.1.2 Analysis of area sensitivity at the interface between the embedded CB and the host material

The interface between the embedded CB and the host material was evaluated by selecting a sample element with the same coordinate point for all models with various area ratios. Figure 5-8 shows the location of the sample element for models with a 1%, 5%, 10% and 20% area ratio.

Ply-by-ply stress analysis is shown for the models in Figure 5-9 in which the stress on the carbon fibre layers had even values. Although the stress on the fibre glass layers trended downwards (less than one percent) from the models of 1% to 20%, the changes were not significant. The details of stress values are mentioned in Table 5-4. As can be seen, the stress values in the 1% model were 144 MPa which decreased to 142 MPa in the 20% model. All in all, the stress distribution values were not affected by the size of the embedded CB at the interface between the CB and the host material.

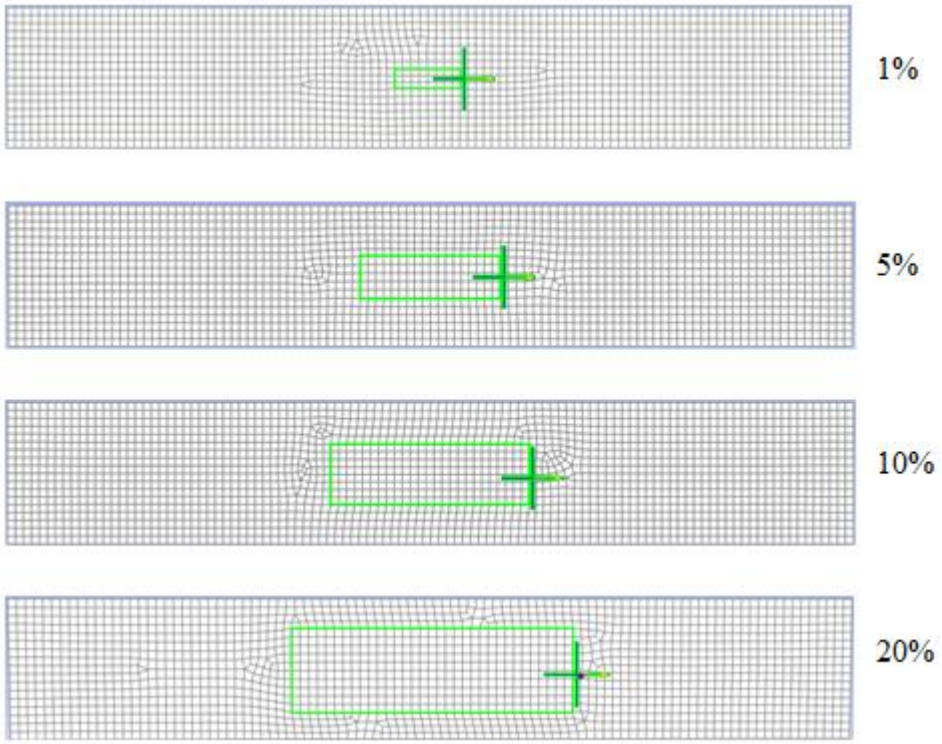

Figure 5-8: Selected sample element at the interface between embedded CB and the host material with various models having area ratios (CB: host) of 1%, 5%, 10% and 20%

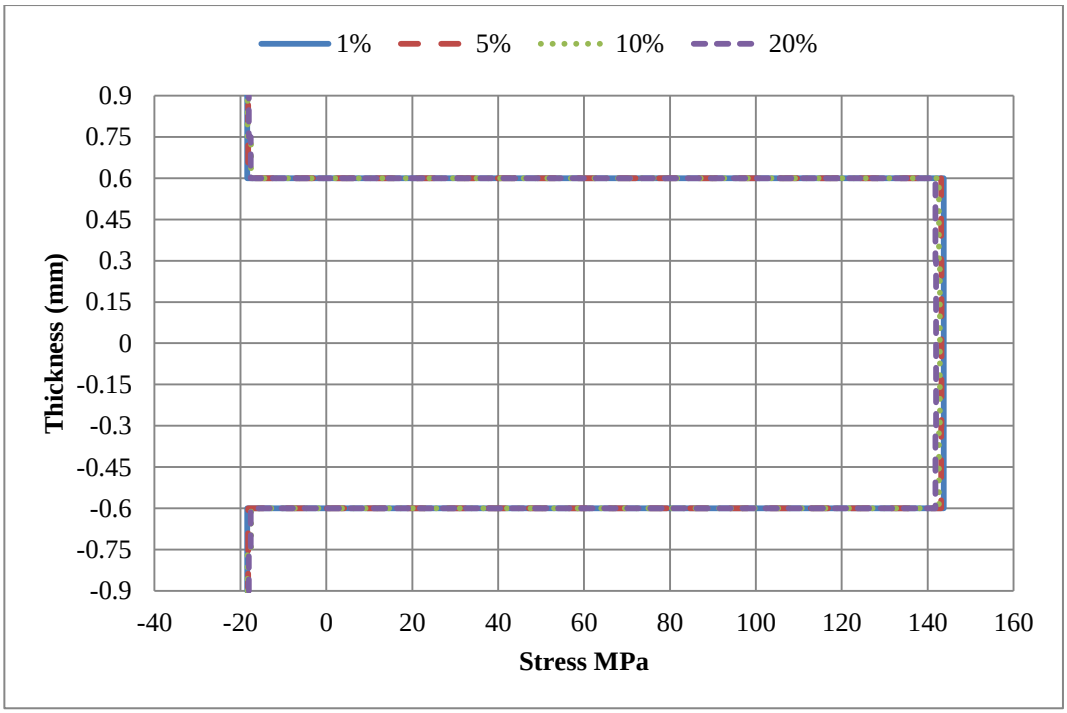

Figure 5-9: Ply-by-ply stress analysis through the $[(\pm 75)_C/(\pm 10)_{FG}]_S$ laminate layer at the interface between the embedded CB and the host material for models with area ratios of 1%, 5%, 10% and 20

Table 5-4: Details of stress analysis through the $[(\pm 75)_C/(\pm 10)_{FG}]_S$ laminate layer at the interface between the embedded CB and the host material for models with area ratios of 1%, 5%, 10% and 20%

			Stress (MPa)			
Ply	**Thickness (mm)**	**Angle (°)**	**1%**	**5%**	**10%**	**20%**
Carbon	0.15	75	-18	-18	-18	-18
Carbon	0.15	-75	-18	-18	-18	-18
Glass	0.3	10	144	143	143	142
Glass	0.3	-10	144	143	143	142
Glass	0.3	-10	144	143	143	142
Glass	0.3	10	144	143	143	142
Carbon	0.15	-75	-18	-18	-18	-18
Carbon	0.15	75	-18	-18	-18	-18

The failure analysis at the interface between the CB and the host material is shown in Table 5-5 and Figure 5-10. It is noted that the IRF values for all models were equivalent in the carbon fibre and fibre glass layers, which confirmed that the CB size was negligible.

Table 5-5: Details of failure analysis through the $[(\pm 75)_C/(\pm 10)_{FG}]_S$ laminate layer at the interface between the embedded CB and the host material for models with area ratios of 1%, 5%, 10% and 20%

			IRF			
Ply	**Thickness (mm)**	**Angle (°)**	**1%**	**5%**	**10%**	**20%**
Carbon	0.15	75	1.2	1.2	1.2	1.2
Carbon	0.15	-75	1.2	1.2	1.2	1.2
Glass	0.3	10	0.3	0.3	0.3	0.3
Glass	0.3	-10	0.3	0.3	0.3	0.3
Glass	0.3	-10	0.3	0.3	0.3	0.3
Glass	0.3	10	0.3	0.3	0.3	0.3
Carbon	0.15	-75	1.2	1.2	1.2	1.2
Carbon	0.15	75	1.2	1.2	1.2	1.2

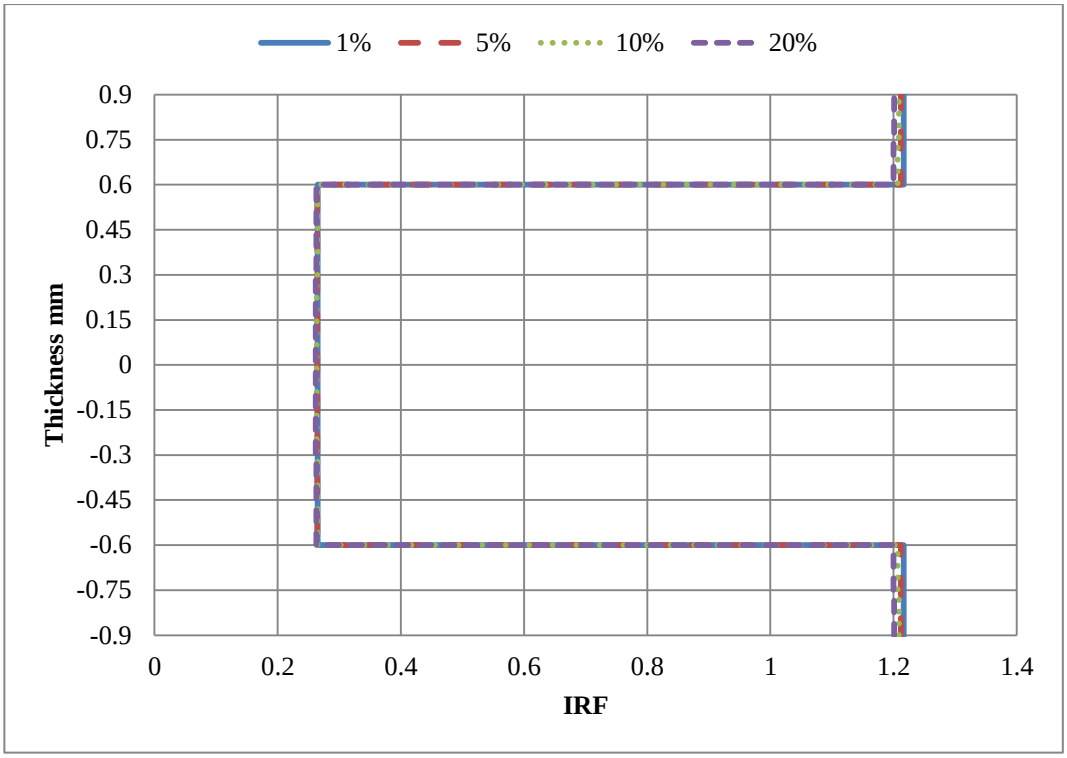

Figure 5-10: Ply-by-ply failure analysis through the $[(\pm75)_C/(\pm10)_{FG}]_S$ laminate layer at the interface between the embedded CB and the host material for models with area ratios of 1%, 5%, 10% and 20%

5.2 Thickness sensitivity

The second sensitivity analysis was the thickness variation effect of the embedded CB within the $[(\pm75)_C/(\pm10)_{FG}]_S$ laminate hybrid composite. When the thickness of the CB becomes large, embedding the CB into the laminate will cause waviness of the surrounding layers and formation of resin pockets, however study of such these parameters were not taken into account in the finite element analysis of this study. Four thickness options (0.1mm, 0.5mm, 1mm and 1.5mm) were selected including the original/baseline CB thickness which was 0.1mm. Consequently, four individual models were created to analyse the effect of thickness variation on the host material. The summary of the laminate models is shown in Table 5-6, and it can be seen in the table that the models were based on the CB thickness. The original/baseline model and all the parameters including the applied load, mechanical properties and dimensions of the host and the embedded CB were selected from the basic model in section 4.1.2, for all models. The only parameter that varied between the models was the CB thickness.

Table 5-6: Details of four models with different CB thicknesses

		Thickness (mm)			
Ply	**Angle (°)**	**0.1**	**0.5**	**1**	**1.5**
Carbon	75	0.15	0.15	0.15	0.15
Carbon	-75	0.15	0.15	0.15	0.15
Glass	10	0.3	0.3	0.3	0.3
Glass	-10	0.3	0.3	0.3	0.3
CB	**0**	**0.1**	**0.5**	**1**	**1.5**
Glass	-10	0.3	0.3	0.3	0.3
Glass	10	0.3	0.3	0.3	0.3
Carbon	-75	0.15	0.15	0.15	0.15
Carbon	75	0.15	0.15	0.15	0.15

5.2.1 Stress analysis and results

A stress analysis was carried out on the four models by generating the contour plots of stress distribution through the laminate plies. Figures 5-11 to 5-14 demonstrate the ply-by-ply stress distribution through the $[(\pm 75)_C/(\pm 10)_{FG}]_S$ laminate layer with an embedded CB having thicknesses of 0.1mm, 0.5mm, 1mm and 0.5mm subject to a unidirectional tensile load. As can be seen from the plots, by increasing the CB thickness the stress concentration values reduced dramatically at the embedded CB (from orange to green colour) and increased at the interface between the embedded CB and the host material. In particular, the stress expanded into the interface between the carbon fibre layers and the CB. It was a note of significance that the thicker CB thickness, the greater the affect on the carbon fibre layers.

As for previous sections, two zones (one at the location of the embedded CB and the other at the interface between the CB and the host material) were examined to demonstrate the details for stress and failure analysis.

The ply-by-ply failure analysis was reported as a Margin of Safety (MoS) which was obtained from equation (4.3). MoS values greater than zero have greater margin to failure and less than zero indicate failure.

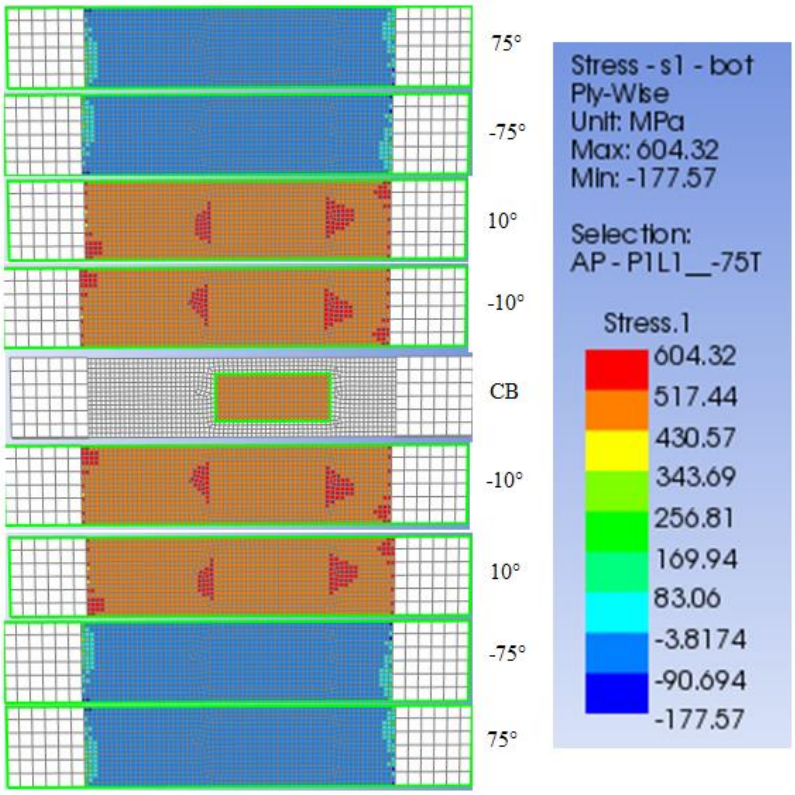

Figure 5-11: Ply-by-ply stress distribution through a $[(\pm 75)_C/(\pm 10)_{FG}]_S$ laminate layer with embedded CB (thickness of <u>0.1mm</u>) subjected to a unidirectional tensile load.

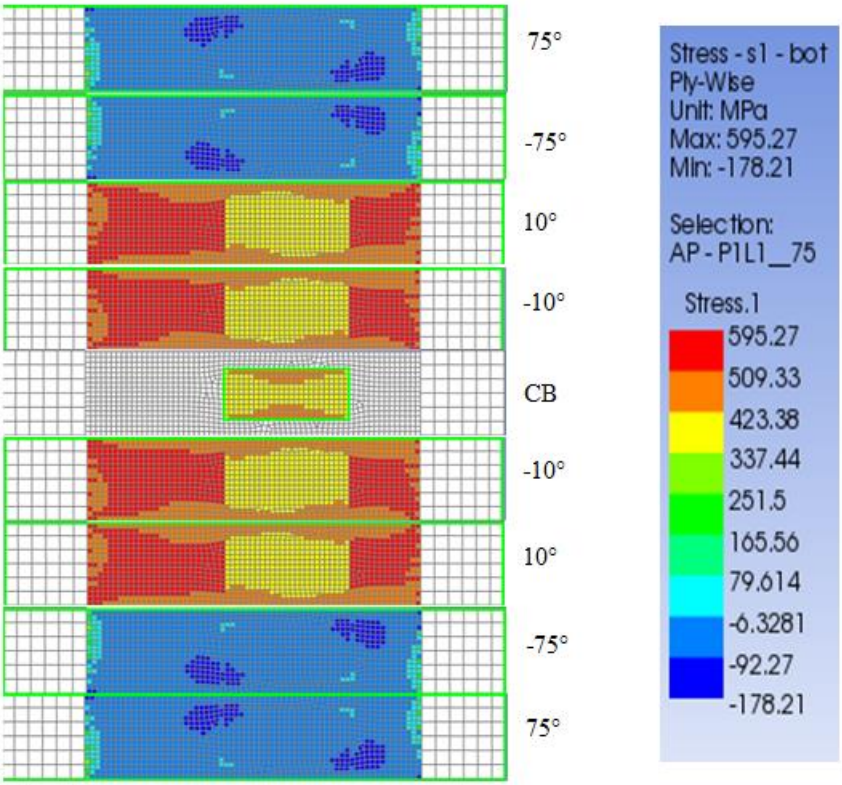

Figure 5-12: Ply-by-ply stress distribution through a $[(\pm 75)_C/(\pm 10)_{FG}]_S$ laminate layer with embedded CB (thickness of <u>0.5mm</u>) subjected to a unidirectional tensile load.

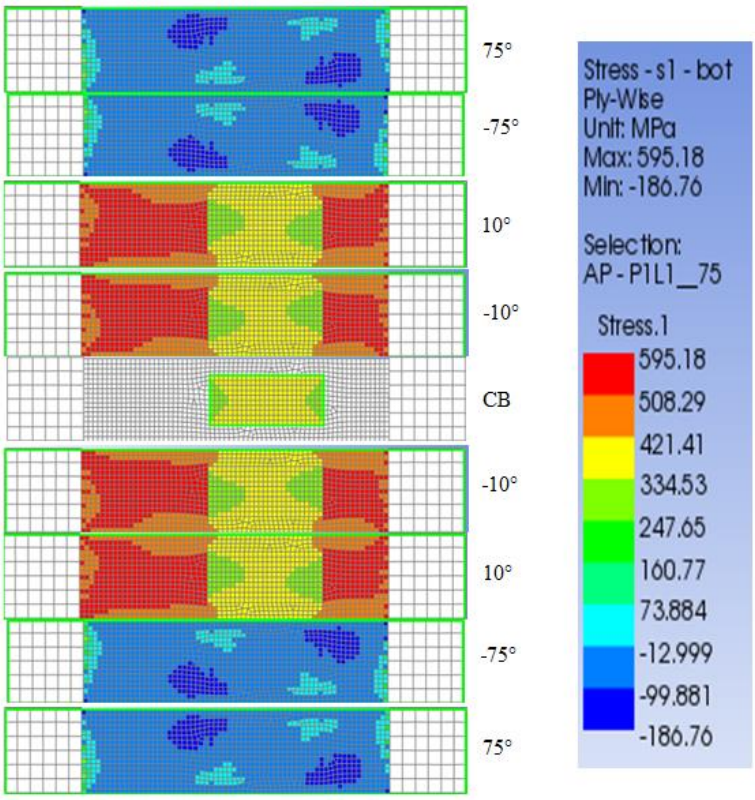

Figure 5-13: Ply-by-ply stress distribution through a $[(\pm 75)_C/(\pm 10)_{FG}]_S$ laminate layer with embedded CB (thickness of <u>1mm</u>) subjected to a unidirectional tensile load.

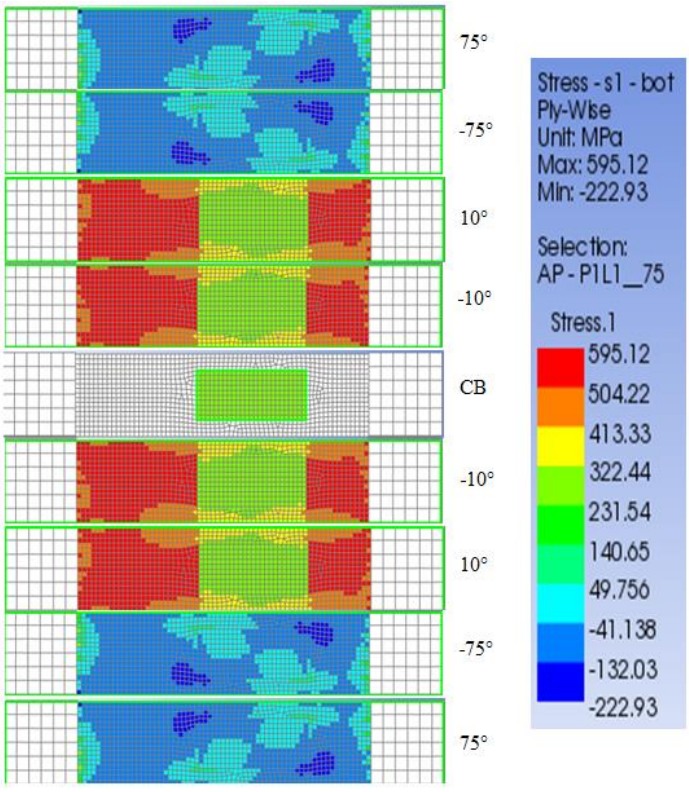

Figure 5-14: Ply-by-ply stress distribution through a $[(\pm 75)_C/(\pm 10)_{FG}]_S$ laminate layer with embedded CB (thickness of <u>1.5mm</u>) subjected to a unidirectional tensile load.

5.2.1.1 Analysis of thickness sensitivity at the location of embedded CB

A selected sample element at the location of an embedded CB revealed the relationship between the CB thickness variation and stress distributions. Figure5-15 shows the position of the selected sample element on a $[(\pm75)_C/(\pm10)_{FG}]_S$ hybrid laminate composite (host material) and the embedded CB for four models with various CB thicknesses. The coordinate point of the selected sample element was the same for all models.

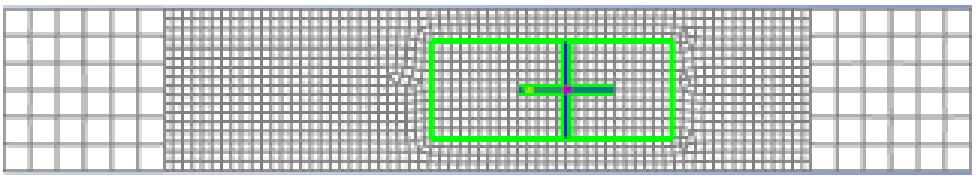

Figure 5-15: Selected sample element at the location of an embedded CB

The ply-by-ply results of stress and failure analysis at a selected sample element at the location of an embedded CB are presented in Table 5-7. It was observed from Figure 5-16 that stress values reduced almost 16% when the CB thickness increased from 0.1mm to 0.5mm, 0.5mm to 1mm and 1mm to 1.5mm through the $[(\pm75)_C/(\pm10)_{FG}]_S$ hybrid laminate layer which meant that the interval CB thickness of 0.5mm between the models caused 16% reduction in stress values.

Table 5-7: Details of stress and failure analysis at selected sample element at the location of embedded CB for four models

		Stress (MPa)				MoS			
Ply	**Angle (°)**	**0.1**	**0.5**	**1**	**1.5**	**0.1**	**0.5**	**1**	**1.5**
Carbon	75	-65	-55	-46	-42	-0.76	-0.71	-0.64	-0.58
Carbon	-75	-66	-57	-49	-39	-0.76	-0.71	-0.65	-0.58
Glass	10	487	408	338	288	0.12	0.35	0.64	0.9
Glass	-10	487	407	338	289	0.12	0.35	0.62	0.92
CB	0	503	421	349	298	0.37	0.64	0.99	1.33
Glass	-10	487	407	338	289	0.12	0.35	0.62	0.92
Glass	10	487	408	338	288	0.12	0.35	0.64	0.9
Carbon	-75	-66	-57	-49	-39	-0.76	-0.71	-0.65	-0.58
Carbon	75	-65	-55	-46	-42	-0.76	-0.71	-0.64	-0.58

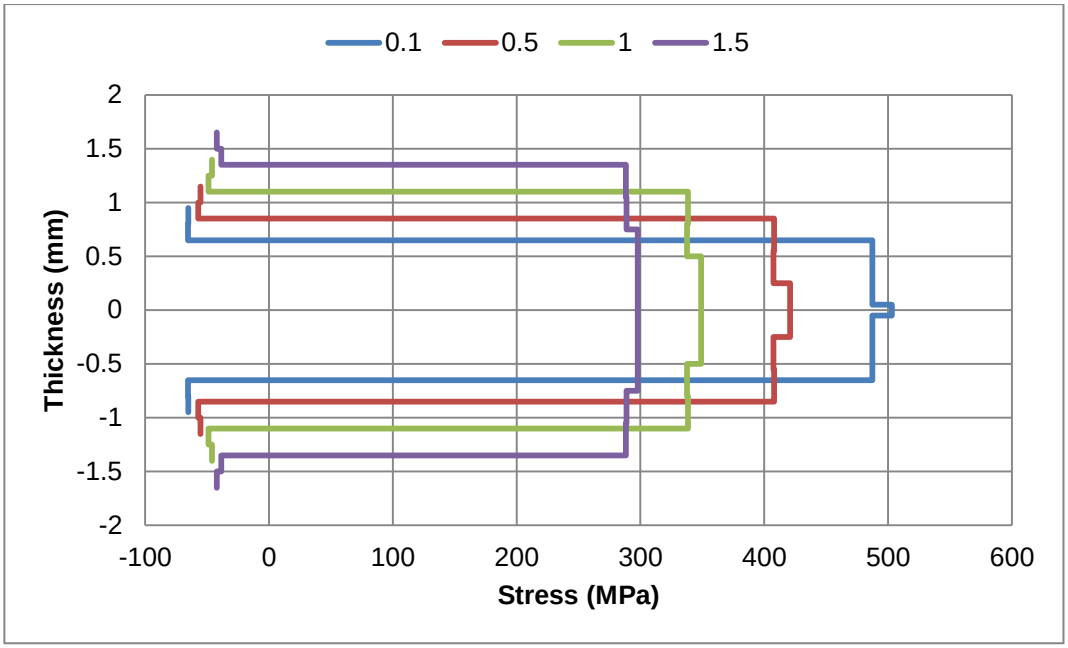

Figure 5-16: Ply-by-ply stress distribution through $[(\pm 75)_C/(\pm 10)_{FG}]_S$ laminate layer of selected sample element at the location of embedded CB

The failure analysis is presented as a margin of safety (MoS) in Figure 5-17 which shows the MoS values within the fibre glass layers change greater than the values within the carbon fibre layers and failure at the location of the embedded CB reduced significantly when the thickness of the CB became thicker from 0.1mm to 1.5mm. By choosing the greater thickness for an embedded CB, the strength of the embedded CB and the host material at that location would rise noticeably.

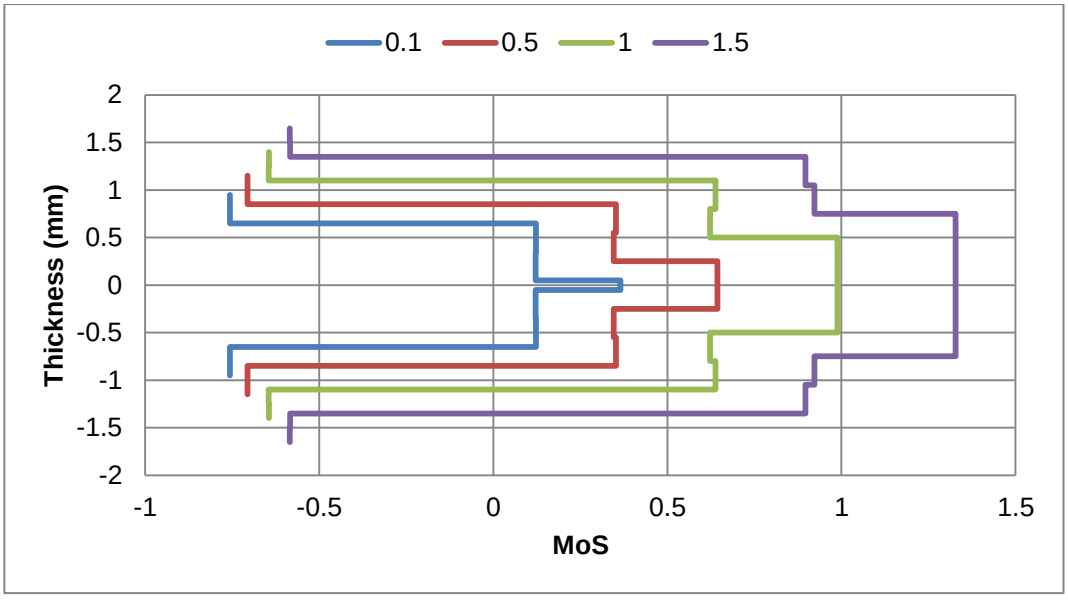

Figure 5-17: Ply-by-ply failure analysis through $[(\pm 75)_C/(\pm 10)_{FG}]_S$ laminate layer at selected sample element at the location of embedded CB

5.2.1.2 Analysis of thickness sensitivity at the interface between the embedded CB and the host material

The second zone was evaluated by taking a sample element at the interface between the embedded CB and a $[(\pm 75)_C/(\pm 10)_{FG}]_S$ laminate (host material) layer as can be seen in Figure 5-18. The coordinate point of the sample element was the same for all models.

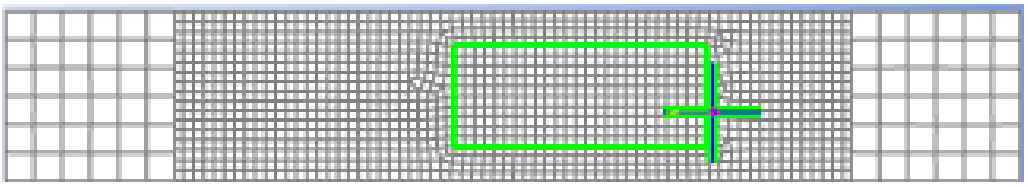

Figure 5-18: Selected sample element at the interface between the embedded CB and the host material

Table 5-8 represents the results of stress and failure analysis for four models at the selected sample element position at the interface between the embedded CB and the host material. It was noted that the stress concentrations increased as the CB thickness increased as shown in Figure 5-19. Values increased around 4% in stress for each CB thickness interval (from 0.1mm to 0.5mm, from 0.5mm to 1mm and 1 to 1.5mm).

One of the main reasons could be because the interlaminar stresses grew at the interface between the embedded CB and the host material.

Table 5-8: Details of stress and failure analysis at selected sample element at the interface between the embedded CB and the host material for four models

		Stress (MPa)				MoS			
Ply	**Angle (°)**	**0.1**	**0.5**	**1**	**1.5**	**0.1**	**0.5**	**1**	**1.5**
Carbon	75	-68	-58	-69	-70	-0.77	-0.78	-0.79	-0.79
Carbon	-75	-65	-62	-43	-40	-0.77	-0.78	-0.78	-0.79
Glass	10	520	542	555	565	0.04	-0.02	-0.08	-0.11
Glass	-10	520	541	561	571	0.05	-0.02	-0.04	-0.06
Glass	-10	520	541	561	571	0.05	-0.02	-0.04	-0.06
Glass	10	520	542	555	565	0.04	-0.02	-0.08	-0.11
Carbon	-75	-65	-62	-43	-40	-0.77	-0.78	-0.78	-0.79
Carbon	75	-68	-58	-69	-70	-0.77	-0.78	-0.79	-0.79

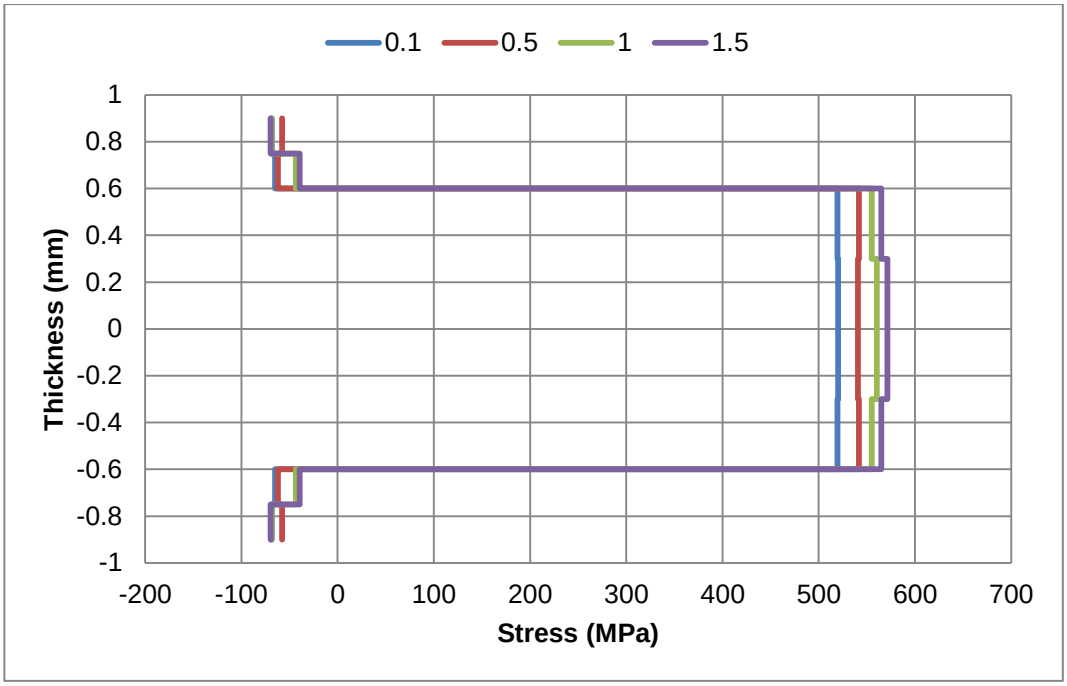

Figure 5-19: Ply-by-ply stress distribution through a $[(\pm 75)_C/(\pm 10)_{FG}]_S$ laminate layer at selected sample element at the interface between the embedded CB and the host material for four models

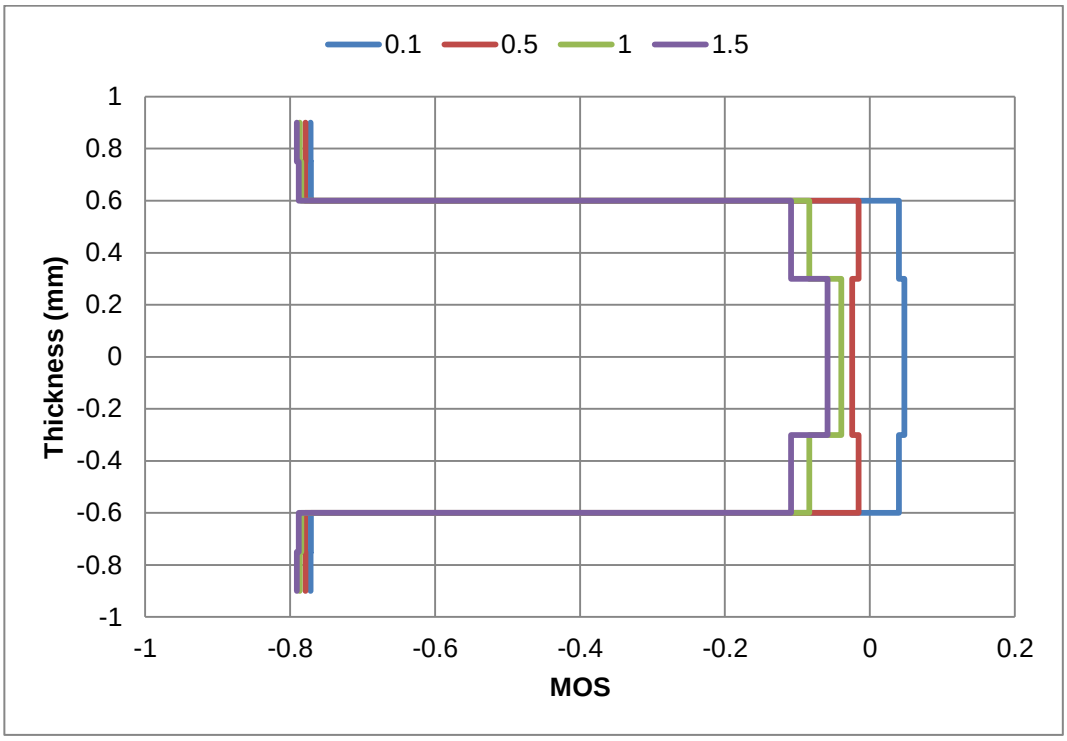

Figure 5-20: Ply-by-ply failure analysis through a $[(\pm 75)_C/(\pm 10)_{FG}]_S$ laminate layer at selected sample element at the interface between the embedded CB and the host material for four models

The failure analysis was demonstrated in Figure 5-20. At the interface between the embedded CB and the host material, the original/baseline model with a CB thickness of 0.1mm had the highest MoS values in carbon fibre and fibre glass layers. In contrast, the model with the CB thickness of 1.5mm had the lowest MoS values which meant that the failure of carbon fibre and fibre glass layers would most likely happen.

In summary, the effect of the CB thickness difference on the strength of the host material was dominant. It is concluded that the CB thickness of 0.1mm (the original/baseline model) had less effect on the strength of the host material than the other models.

5.3 Chapter conclusions

The sensitivity analysis of the CB size on the structural strength of the hybrid composite was evaluated in this chapter. The first analysis (area sensitivity) was carried out on the area ratio of the CB to the host material, with a constant thickness in four different models (area ratios of CB: host of 1%, 5%, 10% and 20%). The results of stress and failure analysis indicated that the area sensitivity did not affect the strength of the host material.

The second analysis was done on thickness sensitivity, in which four thickness variations (0.1mm, 0.5mm, 1mm and 1.5mm) were selected to analyse the role of the CB thickness on the strength of the host material. It was observed from the stress and failure results that although the thicker CB could add strength to electronics and the location of the embedded CB, it caused the stress concentrations or interlaminar stresses at the interface between the embedded CB and the host material to increase and margin to failure importantly reduced.

6 CONCLUSIONS AND RECOMMENDATIONS

6.1 Conclusions

To achieve the optimum design, five different symmetric multidirectional laminated lay-ups were evaluated using eight plies. In order to obtain the optimum design over the multi-angled laminates, a constant uniaxial load of 1000 lb/in was applied at 0 degrees (N_X) on the eight layer laminates. It was assumed that the load in the hoop and shear directions were zero (N_Y and N_{XY}). Based on Tsai-Hill theory, simulation runs were performed for each laminate design and the results indicated that the $[(\pm75)_C/(\pm10)_{FG}]_S$ laminate angles maintained higher MoS values, compared to the other laminate design angles.

Two flat hybrid composites (carbon/glass- and epoxy) in a $[(\pm75)_C/(\pm10)_{FG}]_S$ lay-up and eight plies using a filament winding pattern, with and without an embedded circuit board, were simulated and tested to determine their mechanical performance. The effect of an embedded CB on the host material was investigated numerically as well as experimentally.

Numerical simulation analysis utilised ANSYS ACP software and their findings were validated by fabricating samples. Then, the mechanical properties of the fabricated samples were evaluated by means of a tensile test.

The results from FEA analysis showed that the ultimate stress (485 MPa) on the area in which the CB was embedded was 5% less than the ultimate stress (512 MPa) within the model without an embedded CB. In addition, by choosing the thin CB (0.1mm thickness) the negative effect of a CB on the mechanical properties of a host material became negligible. The IRF results demonstrated that the failures occurred within carbon fibre layers sooner than fibre-glass layers due to the Poisson effect during applied tensile loading.

The results from the experimental work indicated that the ultimate tensile strength and modulus of elasticity of the specimen containing the embedded CB was about 4.7% and 9.7% less than the specimen without the embedded CB, respectively. It was noted that the failure occurred at approximately 43mm away from the location of the CB. Therefore, it can be argued that by designing low angle fibres

surrounding an embedded CB, most of the applied load will be shared by the fibre-glass layers, which in turn would protect the CB from failing.

After validation by numerical simulation analysis, further study was performed on the tube geometry. Two models were created to confirm that the flat model could represent the tube geometry as well. It was assumed that the applied tensile load and cross-sectional area for both models were equal. Therefore, the tube geometry could be applied to the flat geometry. When compared, the stress distributions through the thickness of $[(\pm 75)_C/(\pm 10)_{FG}]_S$ laminates for both models revealed a similarity between them.

In conclusion, the study showed that low angle glass-fibres controlled the applied load, which was transmitted to the carbon fibres until complete failure occurred. The failure mode was verified both theoretically and experimentally, where the failure was initiated as delamination at the interface between the fibre-glass and the carbon fibre. Based on these results, the numerical modelling was in good agreement with the experiments. The CB was embedded into the hybrid composites with minimal deterioration of the hybrid composite's structural strength.

It can be argued that embedding a CB within a composite material would be independent of the geometry of the host material. Parameters like the thickness of the CB and the size ratio of an embedded CB and host material could be more effective subsequently.

The sensitivity analysis of the CB size on the structural strength of the hybrid composite was evaluated. The first analysis was carried out on area sensitivity (the area ratio of the CB area to the host material) with a constant thickness using four different models (the area ratios of CB: host were 1%, 5%, 10% and 20%). The results of stress and failure analysis indicated that the area sensitivity did not affect the strength of the host material.

The second analysis was performed on thickness sensitivity, using four thickness variations (0.1mm, 0.5mm, 1mm and 1.5mm) which were selected to analyse the role of the CB thickness on the strength of the host material. It was observed from the stress and failure results that although the thicker CB could add strength to

electronics at the location of the embedded CB, it caused the stress concentrations or interlaminar stresses in the interface between the embedded CB and the host material to increase, and also the margin to failure dropped (which was important).

6.2 Recommendations

The main focus of this study was to understand the effect of an embedded CB on the strength of the host material. From the study, it is recommended that further research be performed on the effect of the host material on the electronic components in the CB as well. As the unidirectional axial load was considered as an applied load during this study, further study considering biaxial loads applied to the host material is of primary importance. Therefore, an extension of this work for the case of the effect of biaxial loads is necessary in order to evaluate the effect of an embedded CB on the strength of the host material. It is recommended to investigate the effect layer waviness and resin pockets due to embedded sensors on structural integrity of composite laminates.

6.3 Further study

Using my knowledge as a material scientist at Globaltech Corporation and my PhD research at Curtin University, I was able to apply my learnings to build two experimental Condition Monitoring Pads (CMPs). The first CMP was built with fibre-glass/epoxy and infra-red (IR) communication for line-of-sight data transmission in environments where RF would not work eg. under water. The battery in the CMP was charged by a connector.

The second pad shown in Figure 6-1 was also a fibre glass/epoxy with dimensions of 126mm x 115mm x 16mm, which contains accelerometers to show vibrations in the x, y and z directions, strain gauges to show the vectorial changes in strain on the pad and a temperature sensor. The CMP was built with radio frequency (RF) transmitter and an embedded battery which can be charged wirelessly to communicate the data directly to a hand-held tablet (or iPhone).

Figure 6-1: a) CMP with IR, b) CMP with RF data transmission

The tablet displays vibrations in x, y and z directions as gauges on the tablet of Figure 6-2 and after thresholds are set they sound an alarm on the tablet when exceeded. If the strain or temperature of the pad changes, it sounds an alarm on the tablet. For further detail see Figure 6-3.

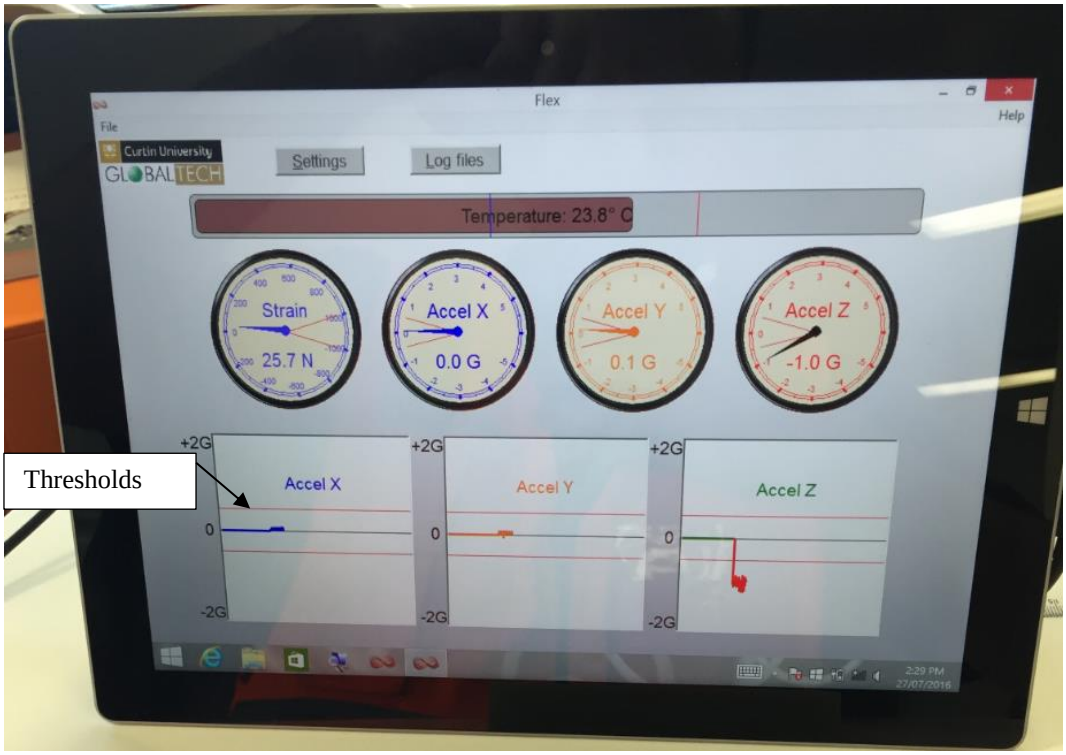

Figure 6-2: CMP tablet showing changes in x, y and z strains as traces, with threshold levels which, if exceeded, sound an alarm. The temperature gauge is shown on the strip across the top.

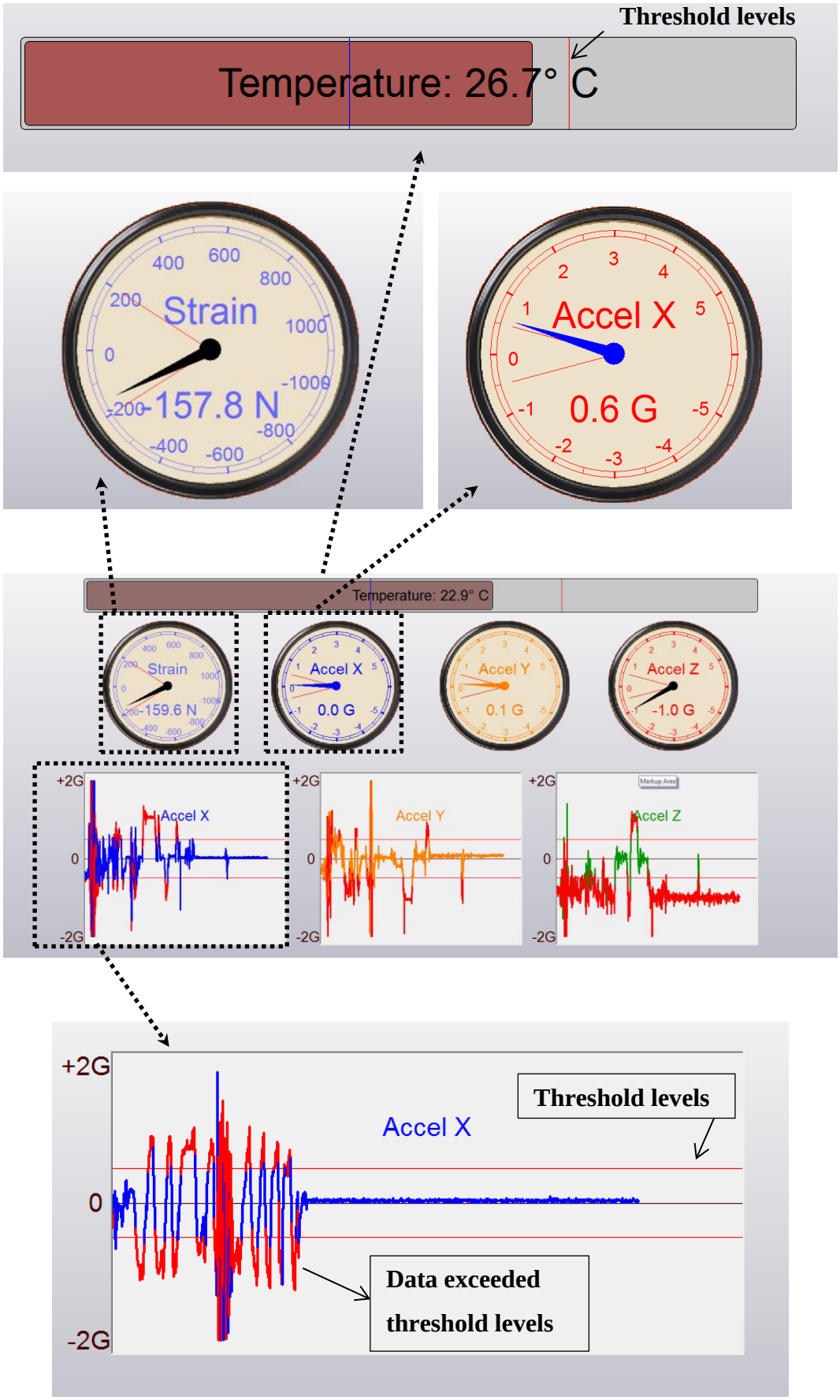

Figure 6-3: The details of the software on the tablet when it is receiving the data from the CMP

6.3.1 CMP application

The CMP fibreglass pad can be glued or bolted externally on any equipment, and will transmit vibrations, strain and temperature changes immediately via RF (or underwater via infra-red) to a receiver, for example a tablet (as shown) or iPhone. Thresholds can be set on the tablet and when any of these are exceeded an alarm will sound. This packaging has encouraged oil and gas company Woodside Energy, to consider using it for vibration monitoring of their LNG process plant, and it is hoped that this application will become a monitoring tool for their process plant monitoring operations of the future.

6.4 Future applications

Additional functionality can be achieved by linking two or more CMPs – for example attaching two CMPS to the outside of a pressure vessel and linking them by IR. If this link breaks it can indicate distortion and therefore give an alarm of excessive pressure within the vessel without needing an internal gauge.

While fibre-glass tanks and pipes can obviously be built containing electronic monitoring devices, such CMPs can be used as sensors externally mounted on process plant equipment on offshore platforms, both above the water line (wifi) and subsea (IR) to provide alarms of equipment going out of specification. The alarms could be connected to a remote monitoring station. Fibreglass/epoxy material has a superior corrosion resistance over conventional materials and can withstand water ingress- while they are intrinsically safe devices where gases are a concern. Consequently, numerous CMPs mounted externally on equipment would be able to monitor the equipment and provide alarms when individual equipment was about to fail. More details about CMP are provided in the Appendix B.

REFERENCES

Aljibori, H. S. S. (2009). Fibre reinforced composite (FRC) structures with potential applications: literature review. *International Journal of Applied Engineering Research*.

Ameri, S. A., Evans, B., Rasouli, V., Roufail, R., Stewart, G. (2014). *Effect of Embedded Electric Sensor on the Structural Strength of Filament Wound Hybrid Composite*. Paper presented at the ASME 2014 33rd International Conference on Ocean, Offshore and Arctic Engineering, San Francisco, California. http://proceedings.asmedigitalcollection.asme.org/proceeding.aspx?articleid=1911717

Ameri, S. A., Evans, B., Rasouli, V., Roufail, R., Stewart, G., Lagat, C. (2014). *The mechanical properties of multi-angle filament wound hybrid composite* Paper presented at the Composites Australia and the CRC for Advanced Composite Structures, Crowne Plaza Hotel, Newcastle.

ANSYS, I. (2013). ANSYS Composite PrepPost User's Guide, from http://148.204.81.206/Ansys/150/ANSYS%20Composite%20PrepPost%20Users%20Guide.pdf

Ashby, M. J., K. (2010). Shaping Profiles *Materials and Design (Second Edition)* (pp. 250-271). Oxford: Butterworth-Heinemann.

ASTM. (2013). ASTM D3171-15 Standard Test Methods for Constituent Content of Composite Materials. West Conshohocken, PA: ASTM International.

ASTM. (2014a). ASTM D3039 / D3039M-14 *Standard Test Method for Tensile Properties of Polymer Matrix Composite Materials*. West Conshohocken, PA: ASTM International.

ASTM. (2014b). ASTM E1237-93 Standard Guide for Installing Bonded Resistance Strain Gages. West Conshohocken, PA: ASTM International.

Baker, A. A., Dutton, S., & Kelly, D. (2004). *Composite materials for aircraft structures* (2nd ed. ed.). Reston, VA: American Institute of Aeronautics and Astronautics.

Beam, S. (2008). About Hipersizer, from http://hypersizer.com/about/

Bednarcyk, B. A., Yarrington, P. W., & Arnold, S. M. (2012). *MULTISCALE FATIGUE ANALYSIS OF COMPOSITE PANELS*. Paper presented at the Mechanics of Nano, Micro and Macro Composite Structures, Politecnico di Torino. http://paginas.fe.up.pt/~icnmmcs/

Birman, V. (2011). *Plate Structures*: Springer Netherlands.

Bourasseau, S., Dupont, M., Pernice, M., Thiriot, A., Blanquet, P., Demol, T., . . . Coutellier, D. (1996). *Integration of optical fibers and piezoelectric ceramics in composite materials.* Paper presented at the 3rd International Conference on Intelligent Materials.

Brothers, G. (2010). Vacuum Bagging Techniques 7th. from http://www.westsystem.com/ss/assets/HowTo-Publications/Vacuum-Bagging-Techniques.pdf

Campbell, F. C. (2010). *Structural composite materials*. Materials Park, Ohio: ASM International.

Composites, R. W. (2016). from http://173.199.132.77/browse/round-carbon-fiber-tubing/filament-wound-carbon-tubing

Corp, C. R. (2011). Methods and Equations Thermoelastic Stiffness Formulation,

from http://hypersizer.com/
Corp, C. R. (2012). Methods and Equations Composite Strength, Ply-Based, from http://hypersizer.com/
Corp, C. R. (2014). HyperSizer Composite Analysis and Structural Sizing Software, from http://hypersizer.com/
Cousigné, O., Moncayo, D., Coutellier, D., Camanho, P., Naceur, H., & Hampel, S. (2013). Development of a new nonlinear numerical material model for woven composite materials accounting for permanent deformation and damage. *Composite Structures, 106*, 601-614. doi: http://dx.doi.org/10.1016/j.compstruct.2013.07.026
CRC, D. (2010). What is DET CRC? , from http://detcrc.com.au/about/what-is-det-crc/
CRC, D. (2013). World's First Successful Drilling with Carbon Fibre Drill Rod. April Newsletter: DET CRC.

Enke, N. F., & Sandor, B. I. (2009). Mechanics of Deformable Bodies *Eshbach's Handbook of Engineering Fundamentals* (pp. 434-508): John Wiley & Sons, Inc.
Eshbach, O. W., & Kutz, M. (2009). *Eshbach's Handbook of Engineering Fundamentals*: Wiley.
Essays, U. (2013). Producing Fiber Reinforced Composites Engineering Essay, from https://www.ukessays.com/essays/engineering/producing-fiber-reinforced-composites-engineering-essay.php?cref=1
Forde, M. (2009). *ICE Manual of Construction Materials, Volume 2 - Metals and Alloys; Polymers; Polymer Fibre Composites in Civil Engineering; Timber; Glass; Non-Conventional Materials; Appendices*: ICE Publishing.
Gemi, L., Tarakçioğlu, N., Akdemir, A., & Şahin, Ö. S. (2009). Progressive fatigue failure behavior of glass/epoxy (±75)2 filament-wound pipes under pure internal pressure. *Materials & Design, 30*(10), 4293-4298. doi: http://dx.doi.org/10.1016/j.matdes.2009.04.025
Globaltech. (2009). Training documentation for Pathfinder
Hagood, N. W., Crawley, E. F., De Luis, J., & Anderson, E. (1989). *Development of integrated components for control of intelligent structures.* Paper presented at the IN: Smart materials, structures, and mathematical issues; US Army Research Office Workshop, Blacksburg, VA, Sept. 15, 16, 1988, Selected Papers (A90-30055 12-39). Lancaster, PA, Technomic Publishing Co., Inc., 1989, p. 80-104.
Harris, B. (1999). *Engineering Composite Materials*. London: IOM.
Herrero, J. (2007). *Buckling, Postbuckling and Progressive Failure Analysis of Hybrid Composite Shear Webs Using a Continuum Damage Mechanics Model.* (Ph.D.), Wichita State University. Retrieved from http://hdl.handle.net/10057/1488
Hill, C. S. (2003). Initial experience with the CDF layer 00 silicon detector. *Nuclear Instruments and Methods in Physics Research Section A: Accelerators, Spectrometers, Detectors and Associated Equipment, 511*(1–2), 118-120. doi: http://dx.doi.org/10.1016/S0168-9002(03)01775-3
Hrinda, G. A. (2008). *Structural Optimization of Conceptual Aerospace Vehicles*. Paper presented at the 4th International Conference on High Performance Structures and Materials, The Algarve; Portugal. http://ntrs.nasa.gov/search.jsp?R=20080019650

Hyer, M. W., & White, S. R. (1998). *Stress Analysis of Fiber-reinforced Composite Materials*: WCB McGraw-Hill.
James C, L. (2011). Development and Manufacture of Cost-Effective Composite Drill Pipe: Advanced Composite Products and Technology (ACPT), Inc. .
Kaddour, A. S., Al-Salehi, F. A. R., Al-Hassani, S. T. S., & Hinton, M. J. (1996). Burst behaviour of ±75 ° filament-wound Kevlar/epoxy and carbon/epoxy tubes at high loading rates. *Composites Science and Technology, 56*(10), 1151-1159. doi: http://dx.doi.org/10.1016/S0266-3538(96)00078-4
Kaddour, A. S., Hinton, M. J., & Soden, P. D. (2003). Behaviour of ±45° glass/epoxy filament wound composite tubes under quasi-static equal biaxial tension–compression loading: experimental results. *Composites Part B: Engineering, 34*(8), 689-704. doi: http://dx.doi.org/10.1016/S1359-8368(03)00077-5
Kaw, A. K. (2006). *Mechanics of composite materials* (2nd ed.). Boca Raton, Fla. London: CRC ; Taylor & Francis [distributor].

Kutz, M. (2002). *Handbook of materials selection*. New York ; [Chichester]: Wiley.
Limited, A. D. I. T. C. (2015). *The Drilling Manual, Fifth Edition*: CRC Press.
Mertiny, P., Ellyin, F., & Hothan, A. (2004). An experimental investigation on the effect of multi-angle filament winding on the strength of tubular composite structures. *Composites Science and Technology, 64*(1), 1-9. doi: http://dx.doi.org/10.1016/S0266-3538(03)00198-2
MIL-HDBK-17-3F. (2002). Military Handbook - MIL-HDBK-17-3F: Composite Materials Handbook, Volume 3 - Polymer Matrix Composites Materials Usage, Design, and Analysis (pp. 70-72): U.S. Department of Defense.
Miracle, D. B., Donaldson, S. L., Henry, S. D., Moosbrugger, C., Anton, G. J., Sanders, B. R., . . . Muldoon, K. (2001). *ASM handbook* (Vol. 21): ASM international Materials Park, OH, USA.
Moulin, E., Assaad, J., Delebarre, C., Kaczmarek, H., & Balageas, D. (1997). Piezoelectric transducer embedded in a composite plate: Application to Lamb wave generation. *Journal of Applied Physics, 82*(5), 2049-2055. doi: doi:http://dx.doi.org/10.1063/1.366015
Muttana Suresh Babu, G. S., Soumitra Biswas. (2009). Composite Fabrication by Filament Winding - An Insight, from http://tifac.org.in/index.php?option=com_content&view=article&id=536:composite-fabrication-by-filament-winding-an-insight&catid=85:publications&Itemid=952
Pagano, N. J., & Pipes, R. B. (1994). The Influence of Stacking Sequence on Laminate Strength. In J. N. Reddy (Ed.), *Mechanics of Composite Materials: Selected Works of Nicholas J. Pagano* (pp. 246-254). Dordrecht: Springer Netherlands.
Peters, S. T. (1998). *Handbook of composites* (2nd ed. / edited by S.T. Peters. ed.). London: Chapman & Hall.
Peters, S. T. (2011). *Composite filament winding*. Materials Park, Ohio: ASM International.
Rohwer, K. (1988). Improved Transverse Shear Stiffnesses for Layered Finite Elements. *DFVLR-FB*.
Rolfes, R. a. R., K. (1997). Improved Transverse Shear Stresses in Composite Finite Elements Based on First Order Shear Deformation Theory. *Int. J.*

Numer. Meth. Engng, 40(1), 51-60. doi: 10.1002/(SICI)1097-0207(19970115)40:1<51::AID-NME49>3.0.CO;2-3
Rosenow, M. W. K. (1984). Wind angle effects in glass fibre-reinforced polyester filament wound pipes. *Composites, 15*(2), 144-152. doi: http://dx.doi.org/10.1016/0010-4361(84)90727-4
Sahin, H. (2012). *Addressing Adaptive Structure Technology to Reduce the Airframe Noise.* KTH Engineering Science, Sweden.
Shalom, S., Harel, H., & Marom, G. (1997). Fatigue behaviour of flat filament-wound polyethylene composites. *Composites Science and Technology, 57*(9–10), 1423-1427. doi: http://dx.doi.org/10.1016/S0266-3538(97)00084-5
Shen, B. S., Tracy, M., Roh, Y.-S., & Chang, F.-K. (1996). Built-in piezoelectrics for processing and health monitoring of composite structures. *AIAA Journal, 1310*, 390-397.
Soden, P. D., Hinton, M. J., & Kaddour, A. S. (1998). Lamina properties, lay-up configurations and loading conditions for a range of fibre-reinforced composite laminates. *Composites Science and Technology, 58*(7), 1011-1022. doi: http://dx.doi.org/10.1016/S0266-3538(98)00078-5
Staab, G. H. (2015). *Laminar Composites (2nd Edition)*: Elsevier.
Stream, P. (2016). Ultrathin Rechargeable Lithium Polymer Batteries from PowerStream, from http://www.powerstream.com/z/ultrathin3.jpg
Strong, A. B. (2008). *Fundamentals of composites manufacturing : materials, methods, and applications* (2nd ed. ed.). Dearborn, Mich.: Society of Manufacturing Engineers.
Summerscales, J., & Short, D. (1978). Carbon fibre and glass fibre hybrid reinforced plastics. *Composites, 9*(3), 157-166. doi: http://dx.doi.org/10.1016/0010-4361(78)90341-5
Torres Arellano, M., Crouzeix, L., Douchin, B., Collombet, F., Hernández Moreno, H., & González Velázquez, J. (2010). Strain field measurement of filament-wound composites at ±55° using digital image correlation: An approach for unit cells employing flat specimens. *Composite Structures, 92*(10), 2457-2464. doi: http://dx.doi.org/10.1016/j.compstruct.2010.02.014
Tsai, S. W., & Wu, E. M. (1971). A General Theory of Strength for Anisotropic Materials. *Journal of Composite Materials, 5*(1), 58-80. doi: 10.1177/002199837100500106
Udar, R. S., & Datta, P. K. (2007). Parametric combination resonance instability characteristics of laminated composite curved panels with circular cutout subjected to non-uniform loading with damping. *International Journal of Mechanical Sciences, 49*(3), 317-334. doi: http://dx.doi.org/10.1016/j.ijmecsci.2006.09.001
Voyiadjis, G. Z. K., P. (2005). Laminate Analysis — Part I *Mechanics of Composite Materials with MATLAB* (pp. 115-147). Berlin, Heidelberg: Springer Berlin Heidelberg.
Warkentin, D. J., Crawley, E. F., & Senturia, S. D. (1991). *Embedded electronics for intelligent structures.* Massachusetts Institute of Technology, Dept. of Aeronautics and Astronautics.
Yang, C. C., J.; Zhao, S. (2013). The Interlaminar Stress of Laminated Composite under Uniform Axial Deformation. *Modeling and Numerical Simulation of Material Science*(3), 49-60. doi:

http://dx.doi.org/10.4236/mnsms.2013.32007
Zweben, C. (2006). Composite Materials *Mechanical Engineers' Handbook* (pp. 380-417): John Wiley & Sons, Inc.
Zweben, C. (2007). Composite Materials *Handbook of Materials Selection* (pp. 357-399): John Wiley & Sons, Inc.

APPENDIX A
FIBRE GLASS/EPOXY ANALYSIS

A.1 FEA for flat fibre glass/epoxy laminate

The FEA simulation was run on flat laminated fibre-glass/epoxy to investigate if hybrid composite is viable. Hybrid composite was proposed in this research based on the advantages mentioned in Chapter 2. The structural strength of a fibre-glass/epoxy laminate could be evaluated via FEA and experimental work.

The laminate of fibre-glass/ epoxy was created using 8 ply stacking sequence of $[\pm 75_{FG}/\pm 10_{FG}]_s$ with dimensions of 300 x 50 x 2.4mm. The CB was not embedded within the laminate layers, as the objective of this simulation was to compare the structural strength of the fibre-glass/epoxy laminate with hybrid laminate.

One end of the model was subjected to a uniaxial tensile load of 34 kN and the other end was fixed. Figure A-1 shows the direction of tensile load towards the X-direction as shown by red arrow. No load is applied in the Y and Z directions.

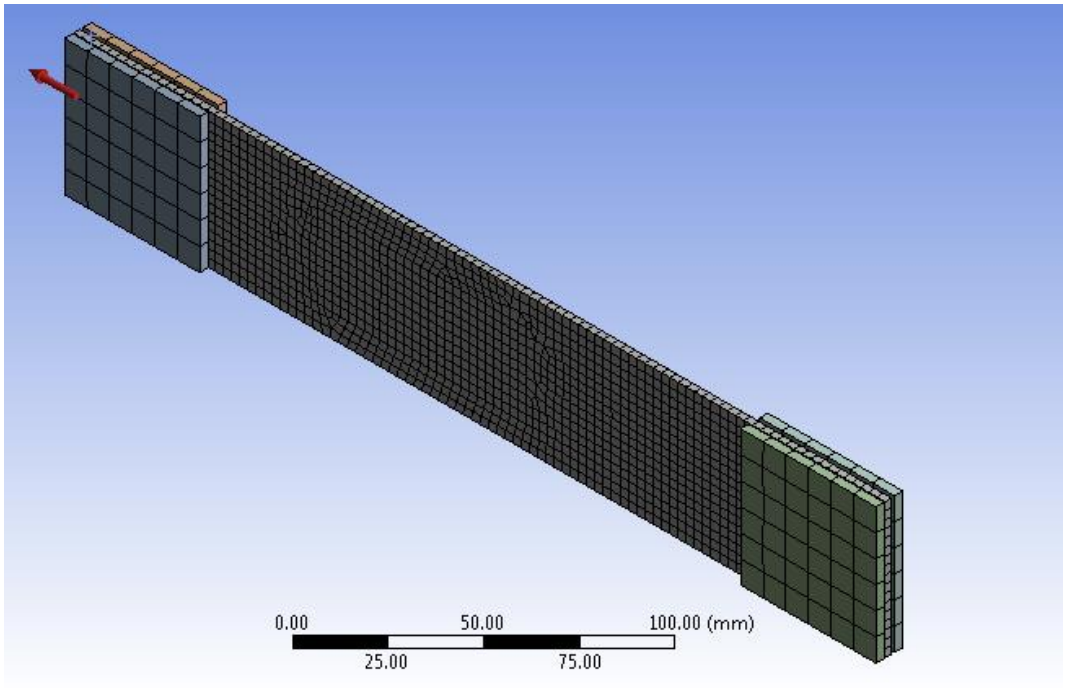

Figure A- 1: Model geometry of $[\pm 75_{FG}/\pm 10_{FG}]_s$ laminate subjected to uniaxial load

A.2 Stress analysis of flat fibre glass/epoxy laminate

The stress distribution was analysed ply-by-ply through the thickness of the $[\pm 75_{FG}/\pm 10_{FG}]_s$ laminated model. Figure A-2 illustrates the stress contour plot ply-by-ply for all laminate layers. The fibres with ±10° carry a significant portion of applied tensile load in the middle of the laminate and fibres with ±75° carry the applied compressional load due to extraction and the Poisson's effect.

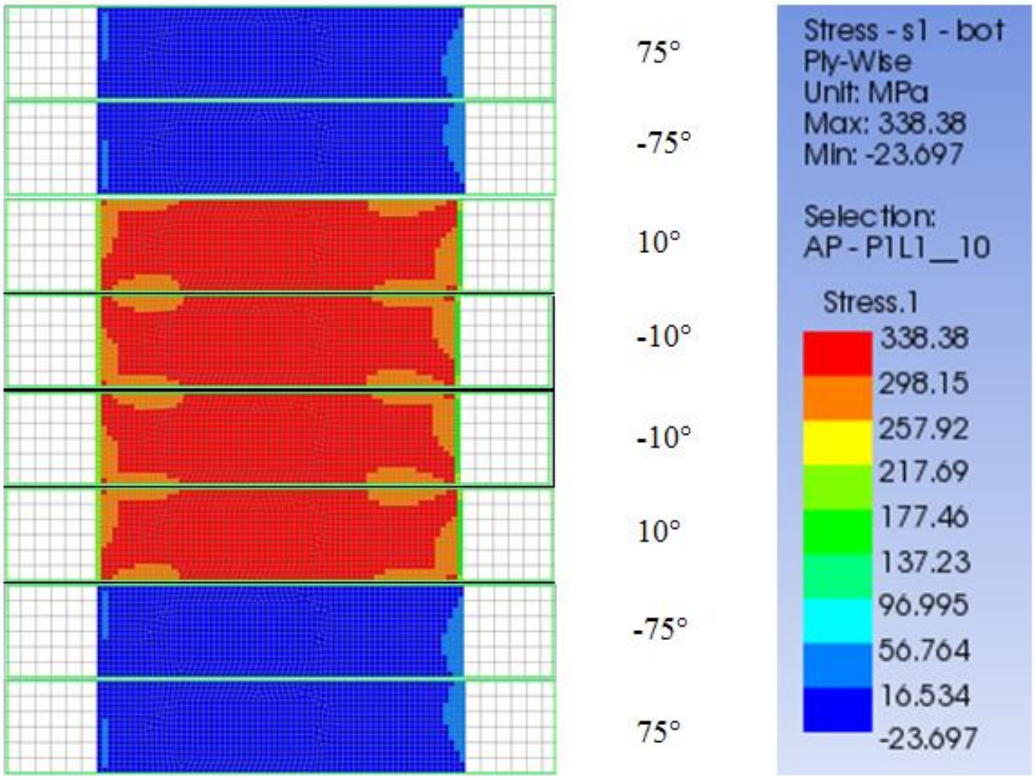

Figure A- 2: Contour plot of stress distribution in flat fibre-glass/epoxy laminate $[\pm 75_{FG}/\pm 10_{FG}]_s$

Figure A-3 shows the stress distribution through the thickness of fibre glass $[\pm 75_{FG}/\pm 10_{FG}]_s$ laminate and hybrid $[\pm 75_{C}/\pm 10_{FG}]_s$ laminate. The step stress distribution is due to the change of material layer properties. The ultimate tensile stress of hybrid laminate is 41% greater than fibre glass laminate.

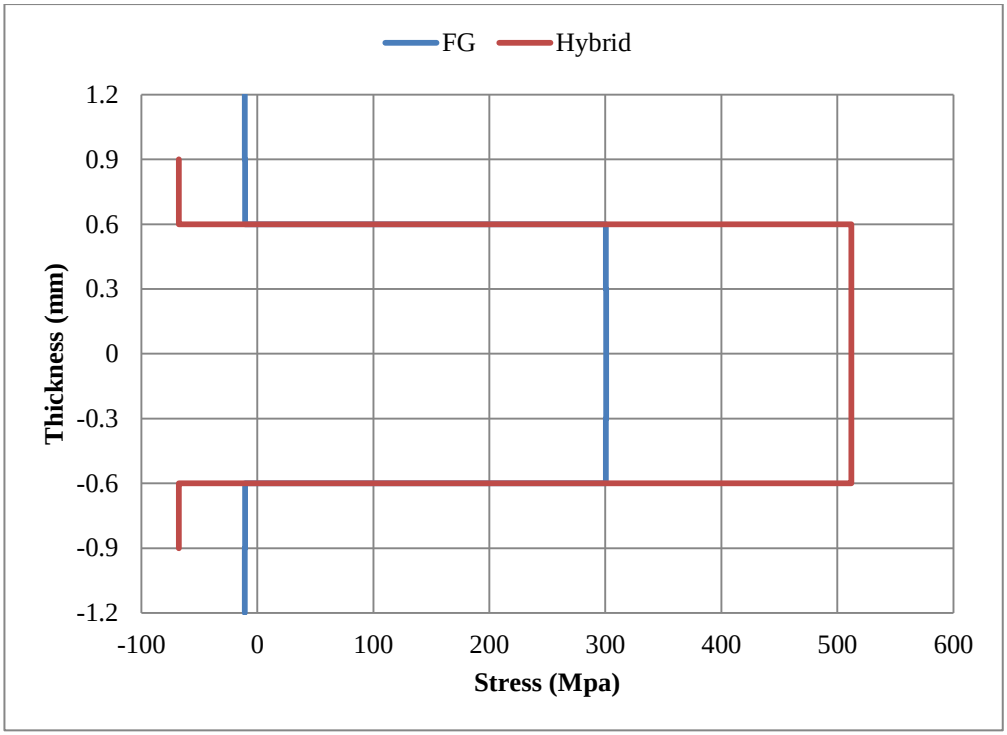

Figure A- 3: Stress distribution through the thickness of fibre glass laminate and hybrid laminate

A.3 Experimental work on flat fibre glass/epoxy laminate

The experimental work was done to validate the FEA analysis. The specimen preparation procedure details are in section 4.2.1 and illustrated in Figures A-4 to A-11. FEA analysis results correlate well to the experimental results.

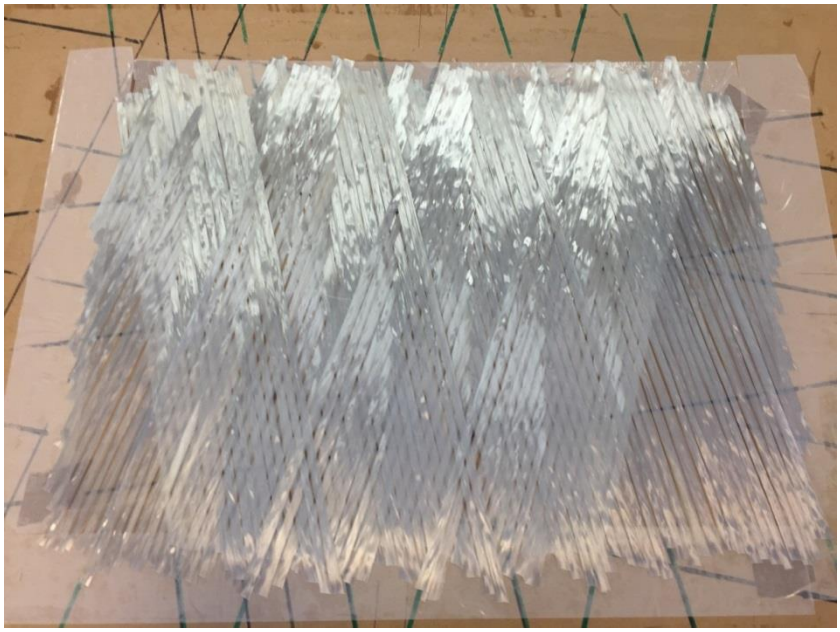

Figure A- 4: Fibre glass lay-up with orientation of ±75° (layers 1 and 2)

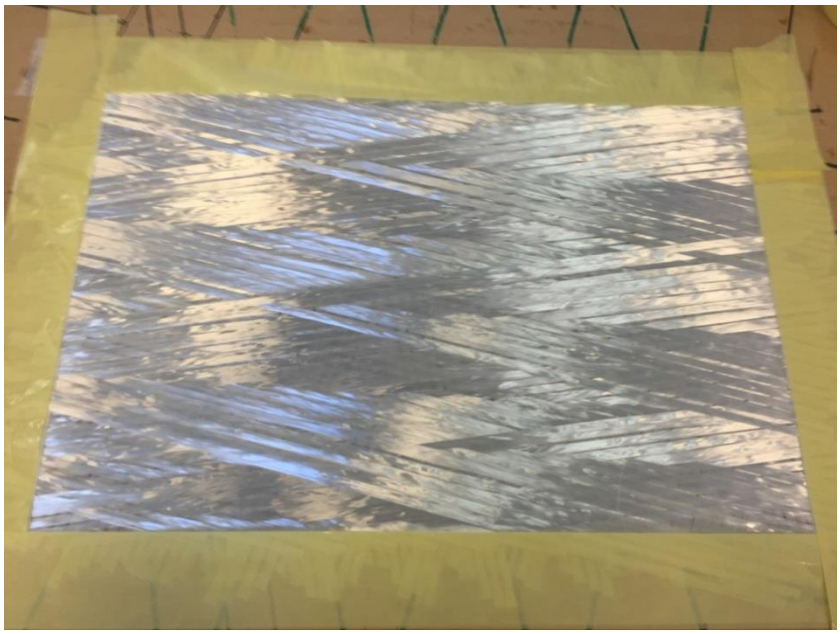

Figure A- 5: Fibre glass lay-up with orientation of ±10° (layers 3 and 4)

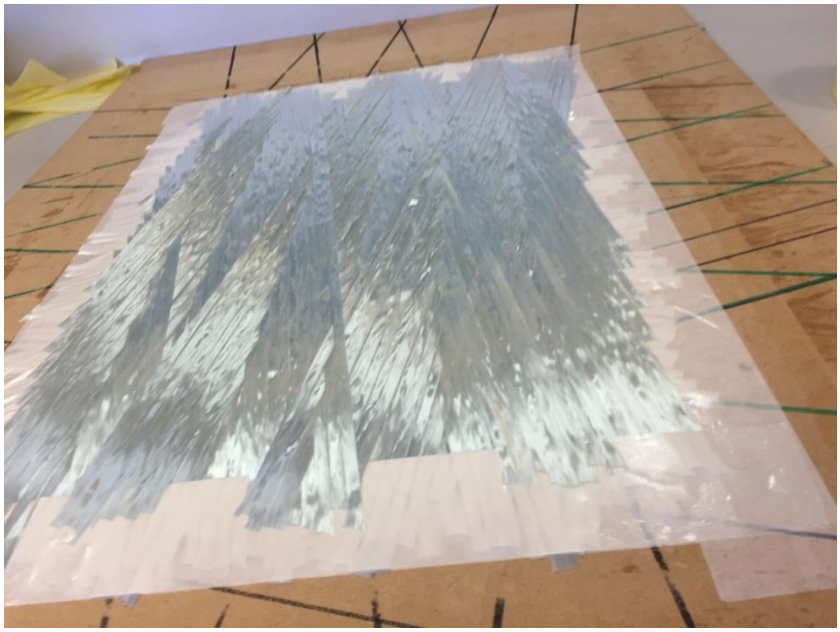

Figure A- 6: Fibre glass lay-up with orientation of ±10° (layers 5 and 6)

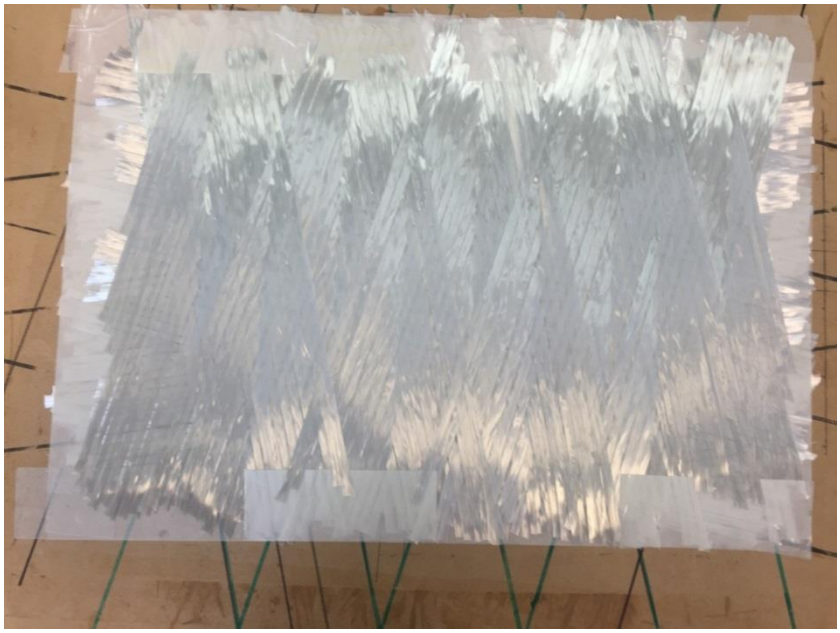

Figure A- 7: Fibre glass lay-up with orientation of ±75° (layers 7 and 8)

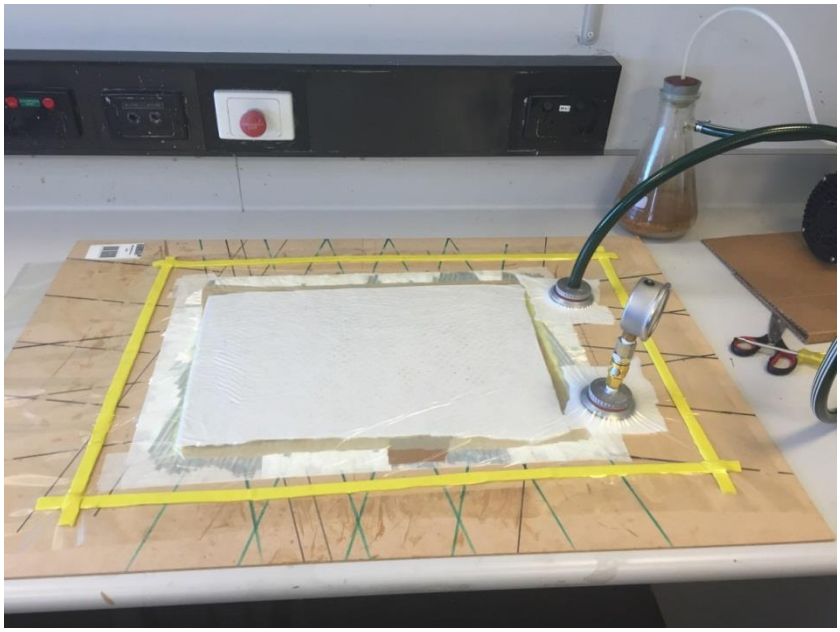

Figure A- 8: Applied epoxy during the Vacuum Bagging Technique

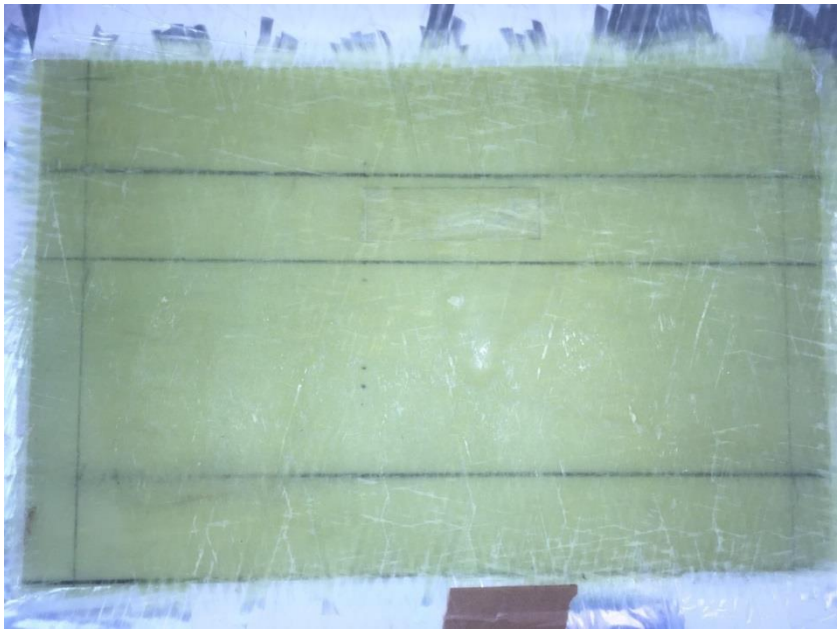

Figure A- 9: Fibre glass/epoxy laminate $[\pm 75_{FG}/\pm 10_{FG}]_s$ after Vacuum Bagging Technique

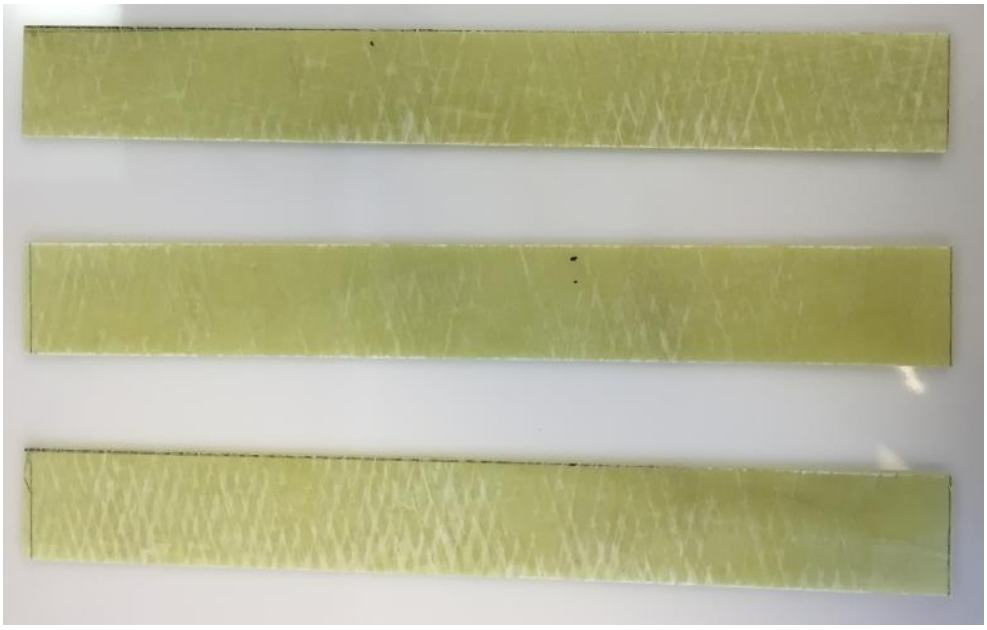

Figure A- 10: Cutting three specimens with dimensions of 50mmx300mm from fibre glass/epoxy laminate $[\pm 75_{FG}/\pm 10_{FG}]_s$

Figure A- 11: Preparing the tabs on the specimens according to ASTM D3039 with attached strain gauges

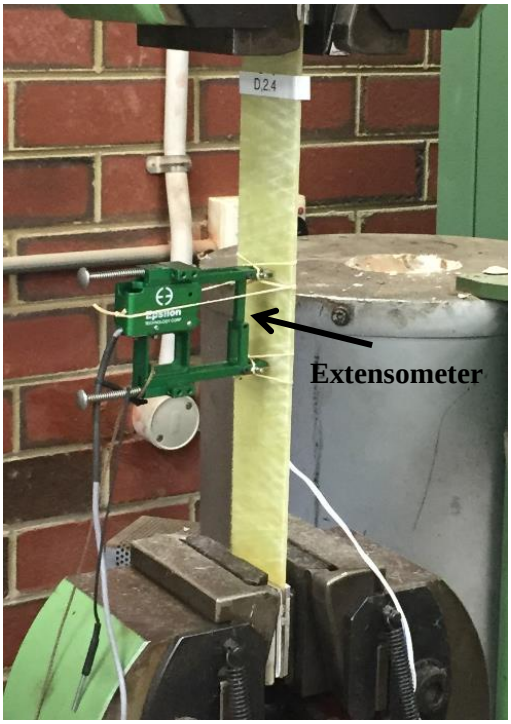

Figure A- 12: Specimen on the tensile machine with attached extensometer

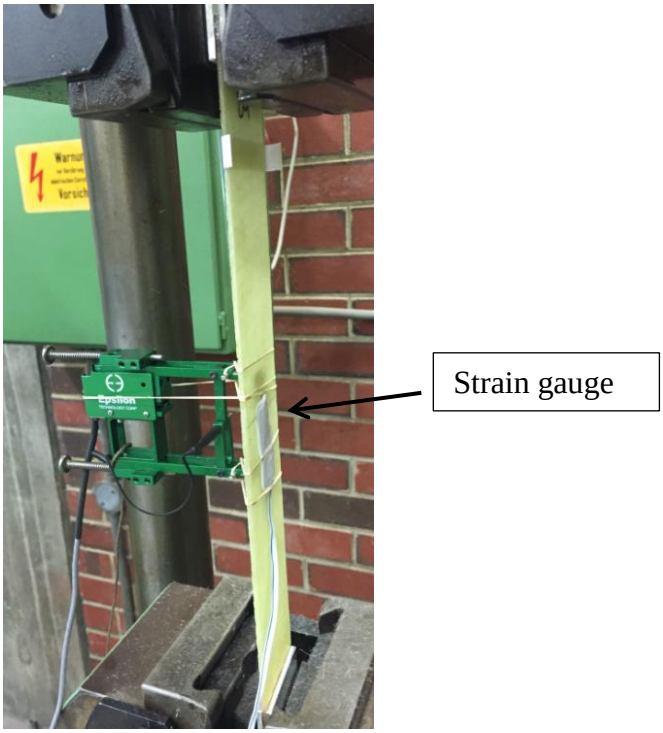

Figure A- 13 Attached extensometer and strain gauge on the middle of the specimen

Figure A- 14: Three specimens after the tensile test

The tensile test was carried out using attached extensometer and strain gauge to record the displacement and strain on each specimen as shown in Figures A-12 to A-14.

By comparing the results between Table 4-3 and Table A-1, the ultimate strength of the fibre glass/epoxy specimen was approximately 40% less than the ultimate strength of hybrid specimens, which confirms that hybrid laminate is a competent choice.

Table A- 1: Results of the tensile test for three specimens

Specimen	Ultimate load (KN)	Ultimate Stress (Mpa)	E (Mpa)	strain (µm/m)	Displacement (mm)	Thickness (mm)
A	37	312	0.0223	14724.25	0.77	2.4
B	35	298	0.0186	15918.91	0.74	2.4
C	34	283	0.023	12352.95	1.2	2.4

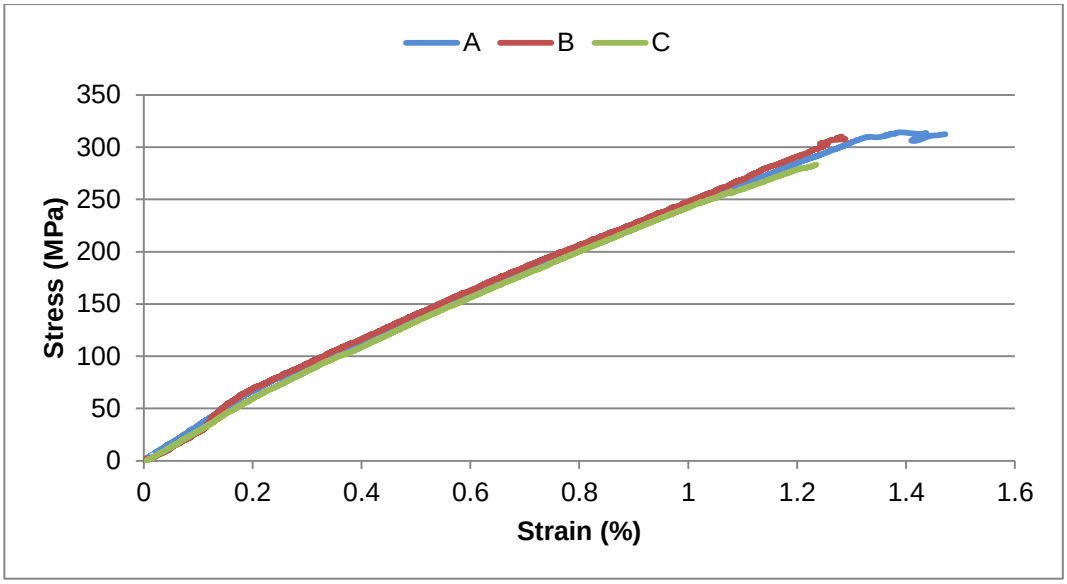

Figure A- 15: Stress vs strain plot of three specimens subjected to the tensile test

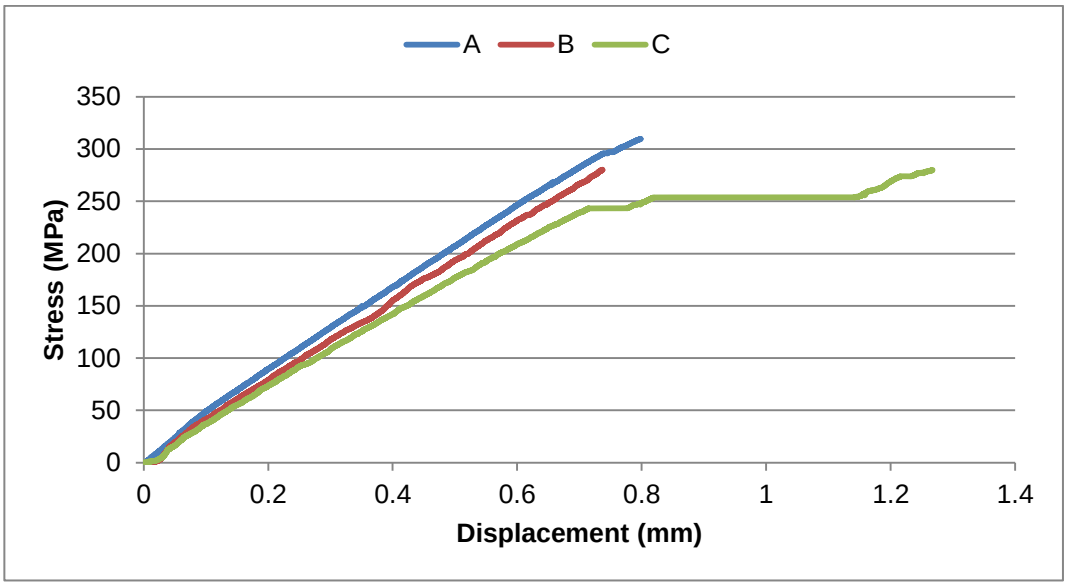

Figure A- 16: Stress vs displacement plot of three specimens subjected to the tensile test

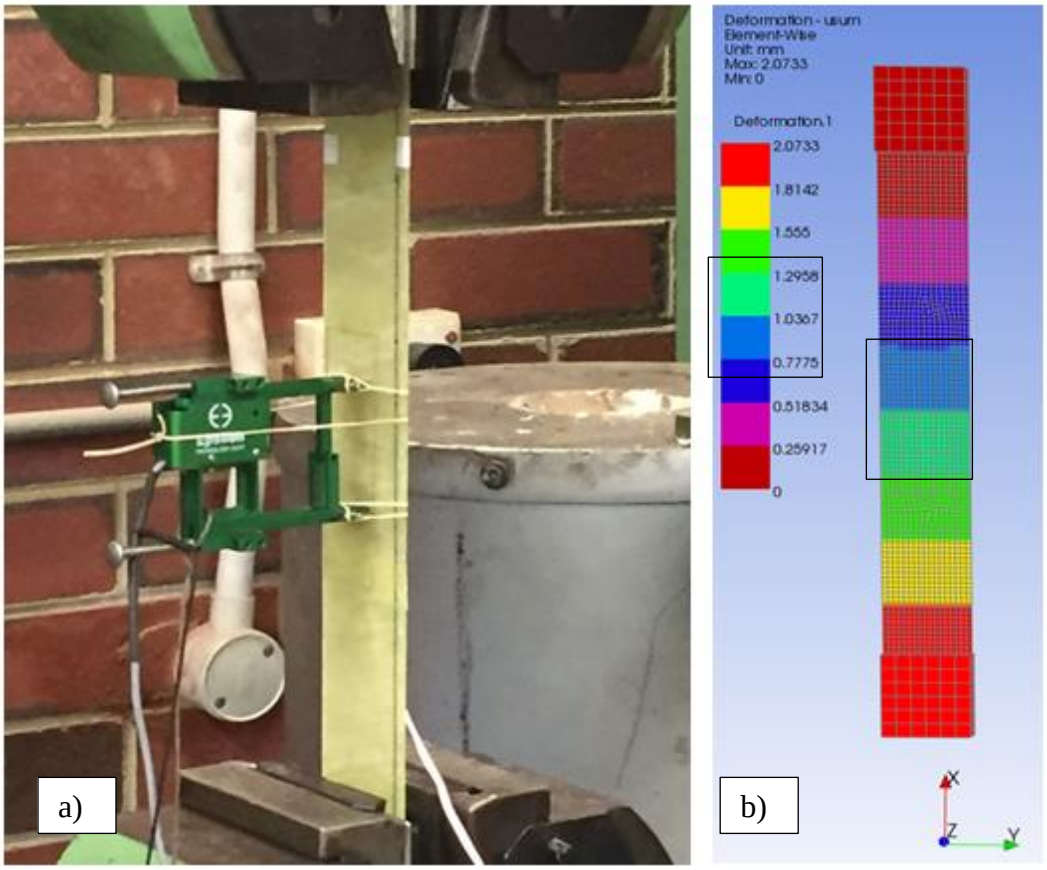

Figure A- 17: a) Location of extensometer on the specimen and b) FEA results of deformation shows good agreement with the tensile test in experimental work

Figure A-17 (a) shows the position of the extensometer on the specimen, which is in the middle. Figure A-17 (b) demonstrates the simulation model of the specimen. It was noted by comparing the results of the extensometer and FEA model's results, the model deformation values were matching the values of extensometer. The light blue and green colours correspond to the location of the extensometer in Figure A-17 (b).

A.4 Fabrication of fibre glass/epoxy filament wound tube with embedded CB for Project 1.3 in DET CRC program

One fibre glass/epoxy filament wound tube with $[\pm 75_{FG}/\pm 10_{FG}]_s$ laminate and embedded CB was fabricated by Teakle Composites for Project 1.3 in the DET CRC research program. The fibre glass/epoxy material was selected because the physical property of the fibre glass/epoxy that made it a better candidate material e.g. fibre glass is translucent and would allow the infrared light to penetrate the fibre layers, accordingly establish communication between transmitter and receiver.

The electronics was provided by Globaltech Corporation Pty. The CB application was the same as the Pathfinder® product produced by Globaltech, which measured the pitch and roll of the composite tube. The composite tube with embedded CB was tested successfully, but this project was subsequently removed from the DET CRC science research program due to budget cuts. Figures A-18 to A-24 show the filament winding fabrication procedure.

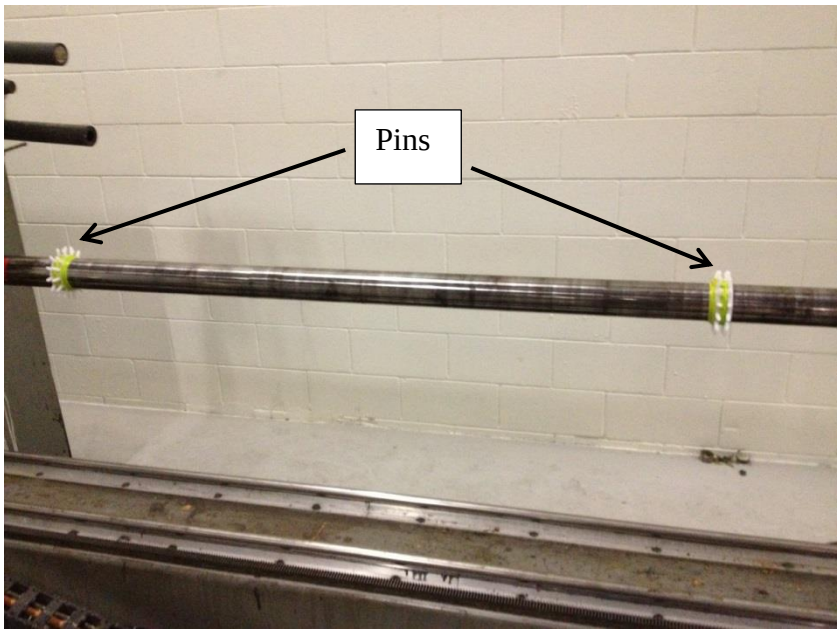

Figure A- 18: Mandrel with attached pins in filament winding machine

Figure A- 19: Winding fibre glass at ±75°

Figure A- 20: Winding fibre glass at ±10° using the pins on the mandrel

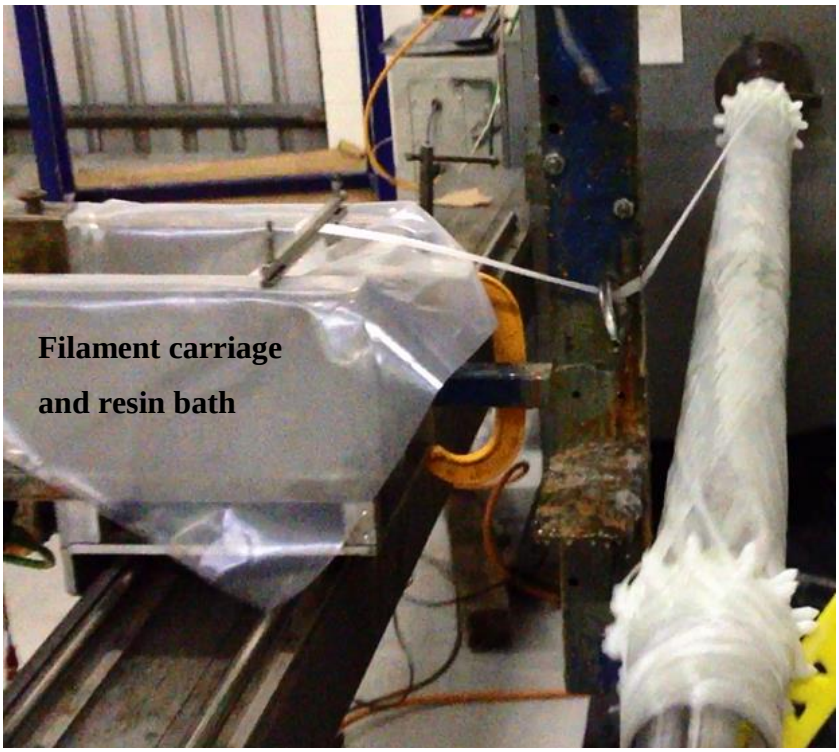

Figure A- 21: Filament carriage and resin bath in filament winding machine

Figure A- 22: Embedded CB in the mid layer of filament wound tube

Figure A- 23: Using tensioned tape to remove air trap and resin excess between the fibres

Figure A- 24: Filament wound tube $[\pm 75_{FG}/\pm 10_{FG}]_s$ with embedded CB

APPENDIX B
CONDITION MONITORING PADS

This section describes the fabrication of two Condition Monitoring Pads (CMPs), in which one used infra-red (IR) for data transmission while the other used radio frequency (RF) as shown in Figure B-1.

Figure B- 1: CMP with IR and RF communication

B.1 Condition Monitoring Pad with IR communication

The hosting material is unidirectional fibre glass fabricated with epoxy resin. Hand lay-up of 60 layers and vacuum bagging technique were utilized. The composite plies surrounding the embedded electronics were cut. The fabrication procedure was as follows:

1. 36 layers of flat fibre glass/epoxy laminate were fabricated as a core of the host material as shown in Figure B-2 and B-3.

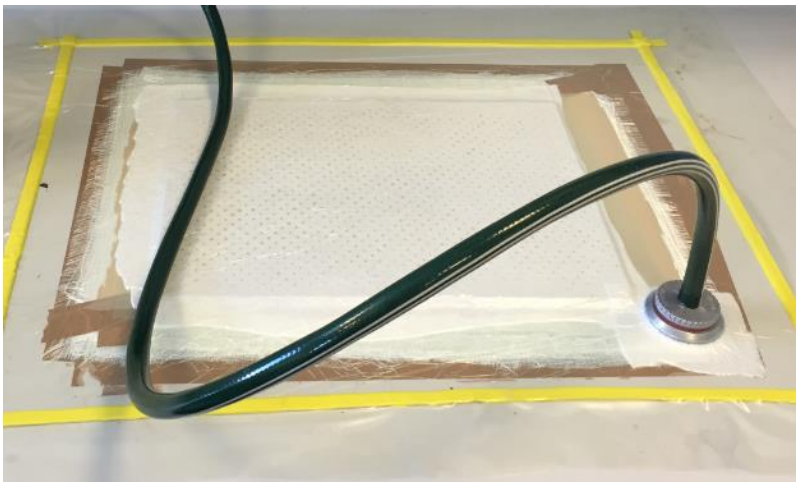

Figure B- 2: The process of the vacuum bagging technique

Figure B- 3: 36 layers of fibre glass/epoxy laminate

2. The composite plies in the middle of the core were cut by water jet in a rectangular shape.
3. One side of the core was covered with a layer of 6 fibre glass plies as shown in Figure B-4.

Figure B- 4: Cut fibre glass/epoxy laminate

4. Strain gauges were attached between the layers of the laminate to show the vectorial changes in strain on the pad as demonstrated in Figures B-5 and B-6. The accelerometers and temperature sensors were located on the main circuit board.

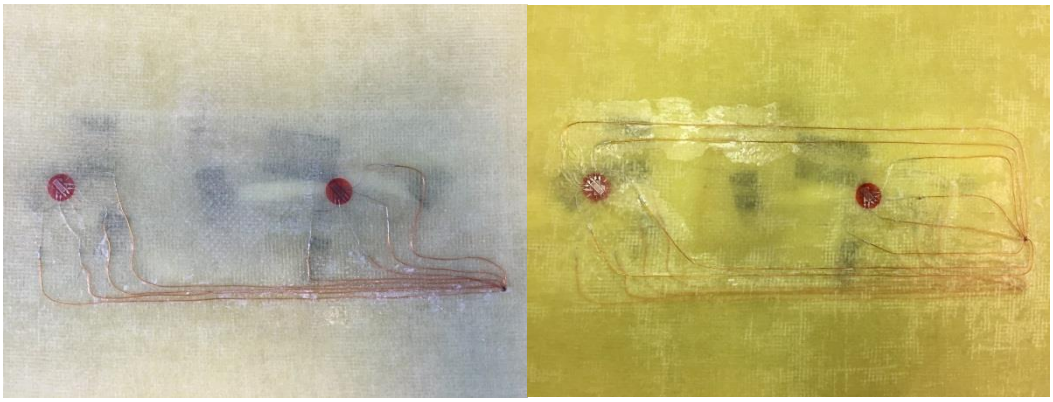

Figure B- 5: Two full bridge strain gauges were attached between the layers

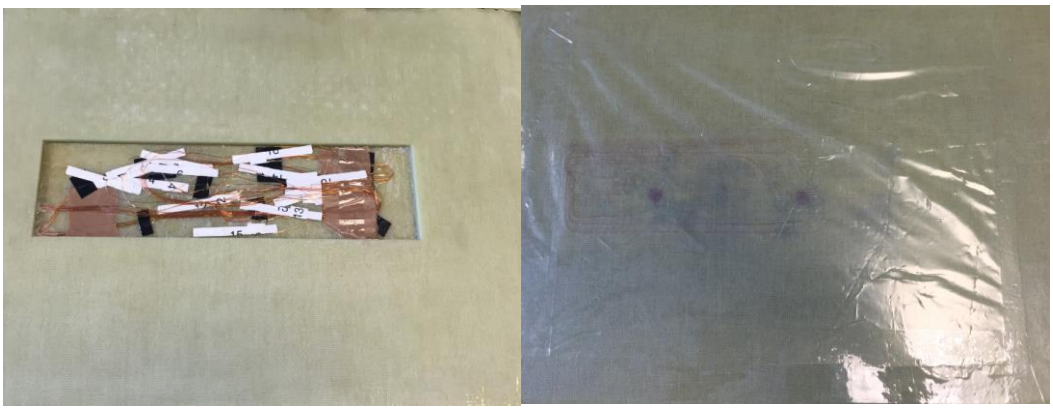

Figure B- 6: Back and front view of the CMP after installing the strain gauges

5 The electronics and the battery were integrated inside the cavity and wired up to the strain gauges.

6 All electronics were encapsulated by clear silicon resin to fix and protect them from any harsh environment and fluid. The other advantage of the silicon encapsulation easy accessibility to the electronics, since the hardness of the silicon is less than the epoxy resin and would be easy to remove the silicon and without damaging the electronics. Figure B-7 shows the details of the electronics and clear silicon encapsulation.

7 The source of power is a rechargeable battery. To maintain the life of the battery, a reed switch is used to turn off the electronics when it is not in use. The switch will be off when the magnet is attached to the pad and will be on when the magnet is removed.

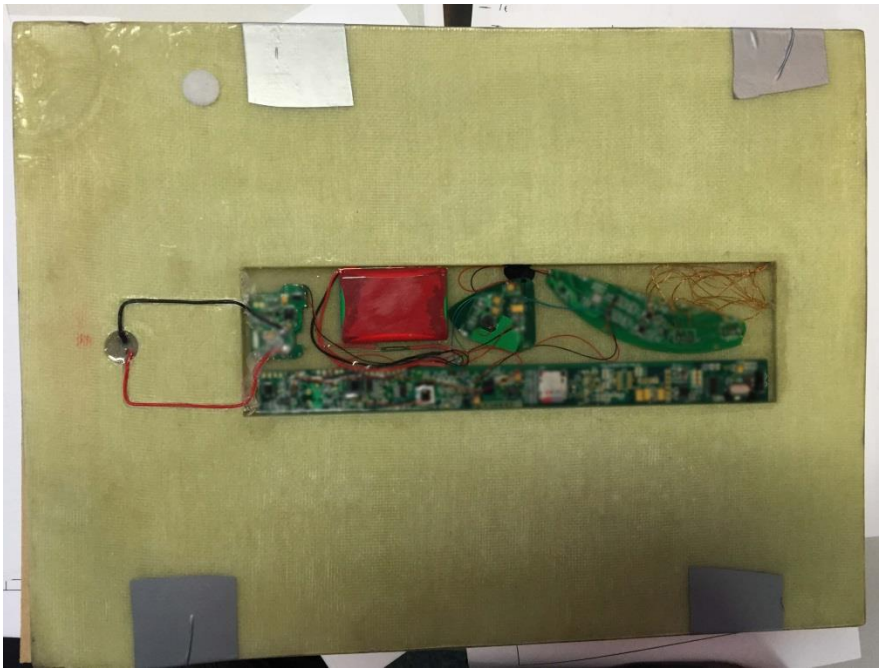

Figure B- 7: Electronics and battery were integrated into the fibre glass/epoxy laminate and encapsulated by silicon resin

8 Four layers of flat fibre glass/epoxy laminate were added to cover and protect the electronics as shown in Figure B-8.

9 The CMP was cut to dimensions of 368mm x 130mm for easy handling, as demonstrated in Figure B-9.

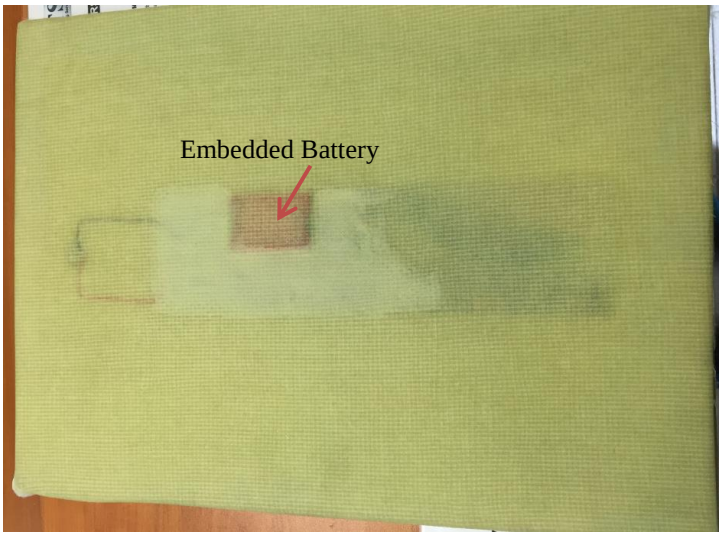

Figure B- 8: Added protecting layers on the electronics

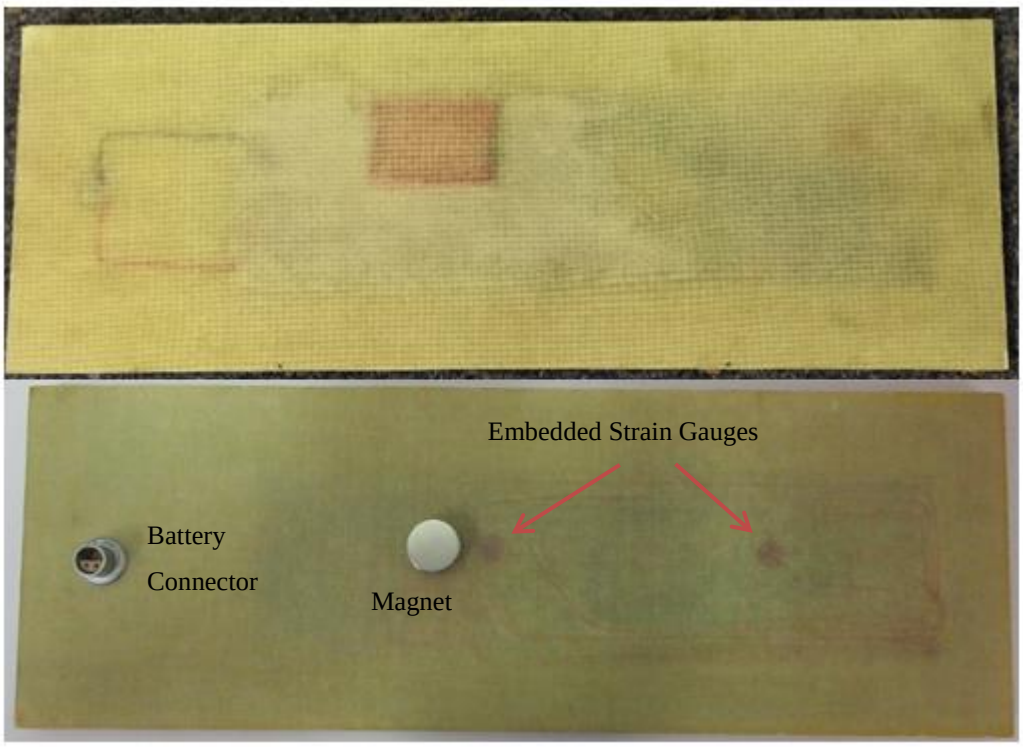

Figure B- 9: Cut CMP in front and rear view

10. The CMP was labelled to guide the instrument users (Figure B-10). To communicate with the tablet a hand-held IR receiver was used as shown in Figures B-11 and B-12.

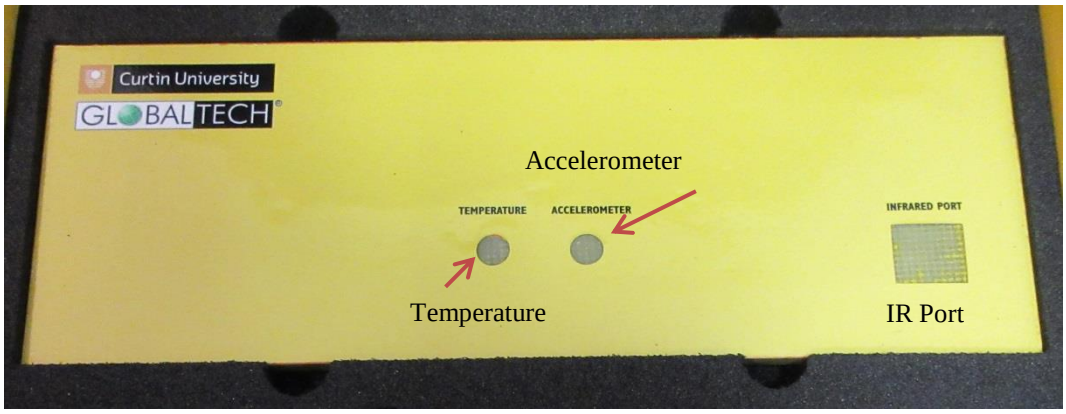

Figure B- 10: Location of the accelerometer and temperature sensor on the CMP

Figure B- 11: Hand-held IR receiver

Figure B- 12: Connection between the tablet and the hand-held receiver

11. Figures B-13 and B-14 show how the hand-held and CMP were communicating through the IR light. The receiver is pointing towards the IR port on the CMP and receiving data.

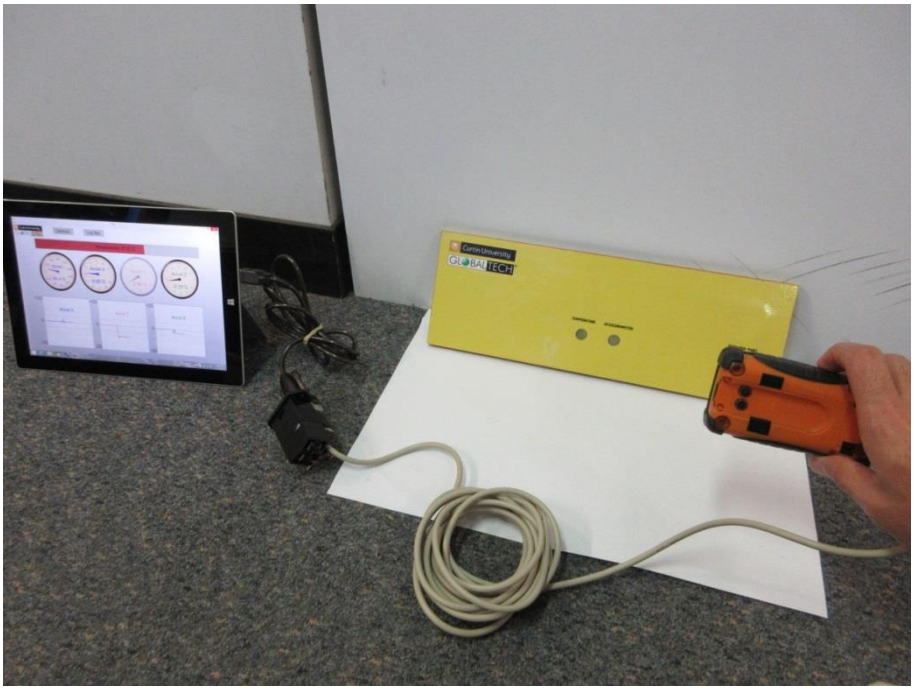

Figure B- 13: IR Communication between the CMP and the tablet

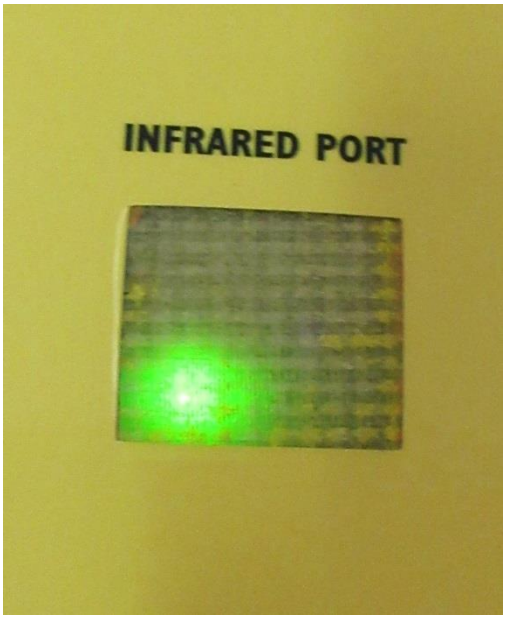

Figure B- 14: CMP transmits data by IR light

12. Then data was transferred to the tablet for display using Flex software, which was created by Globaltech and funded by Curtin University (Figure B-15). Figure B-16 shows the assembly of the charger and CMP's battery connector.

Figure B- 15: Flex Software in the tablet

Figure B- 16: Assembly of battery charger and the connector on the CMP

B.2 Condition Monitoring Pad with RF communication

A second CMP was developed and upgraded to achieve the following objectives:

- To reduce the size (126mm by 115mm)
- Increase range of communication between CMP and the tablet up to 2km via wireless communication
- Increase operation time by decreasing down time to recharge battery via adding a wireless battery charger (inductive charging)

The fabrication method of the CMP with RF was similar to the CMP with IR, with a change of the type of electronics; size was reduced and four strain gauges were added. Figures B-17 to B-22 illustrate the fabrication of the CMP with RF.

Figure B- 17: Core laminate was fabricated by double bias fibreglass fabric and epoxy resin with hand lay-up and vacuum bagging technique using 39 layers

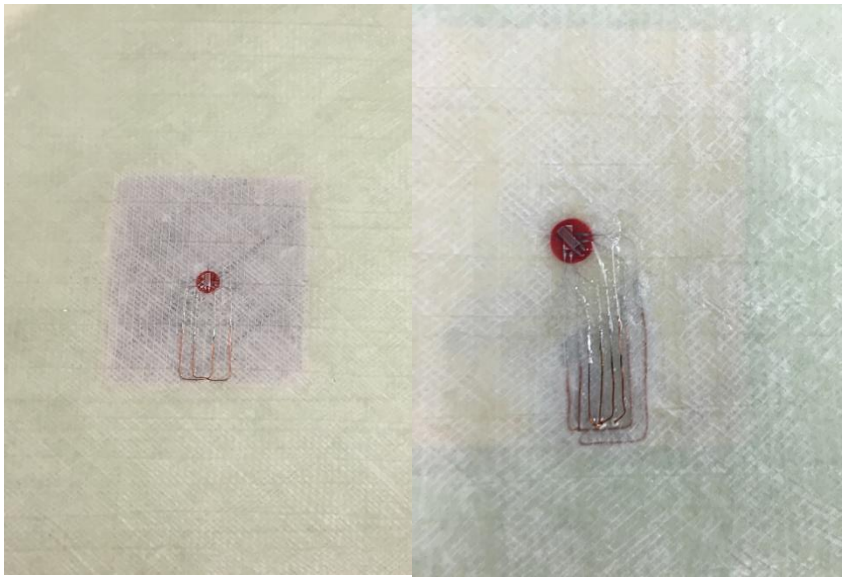

Figure B- 18: Strain gauges were attached between the layers of fibre glass/epoxy

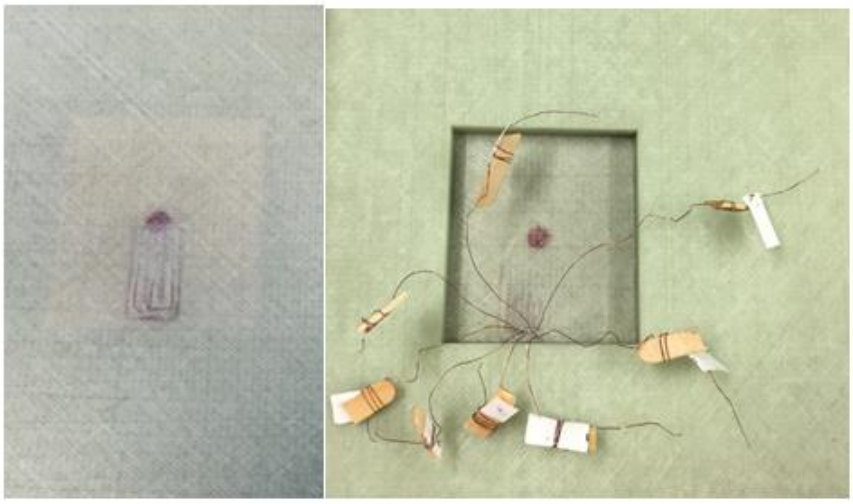

Figure B- 19: Front and rear view of the CMP with RF after attaching the strain gauges between the laminated layers

Figure B-20 shows the main circuit board with attached accelerometers and temperature sensors as well as the battery with inductive receiver and Reed switch. All the electronics components were potted with clear silicon resin. Then the panel was cut to 126mm by 115mm as shown in Figure B-21.

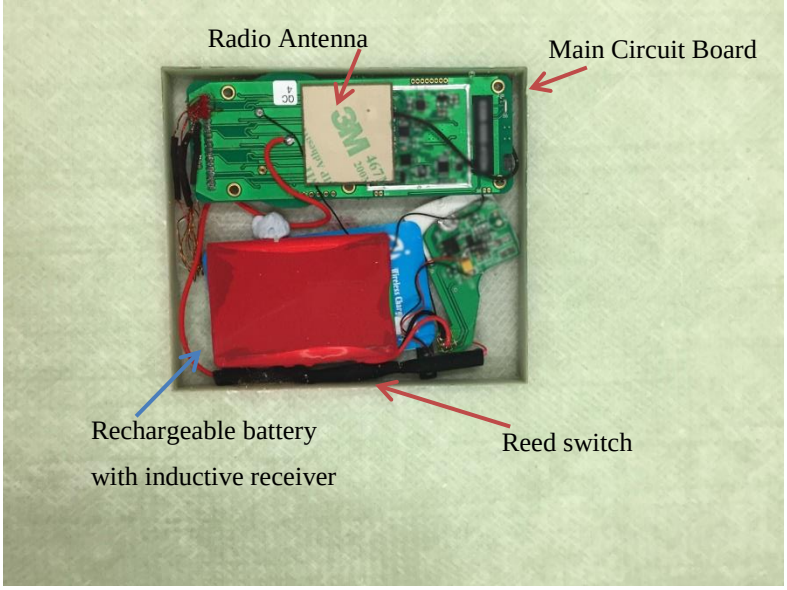

Figure B- 20: Integrated electronics and battery were potted with Silicon resin

Figure B- 21: Water jet is cutting the laminate with embedded sensors

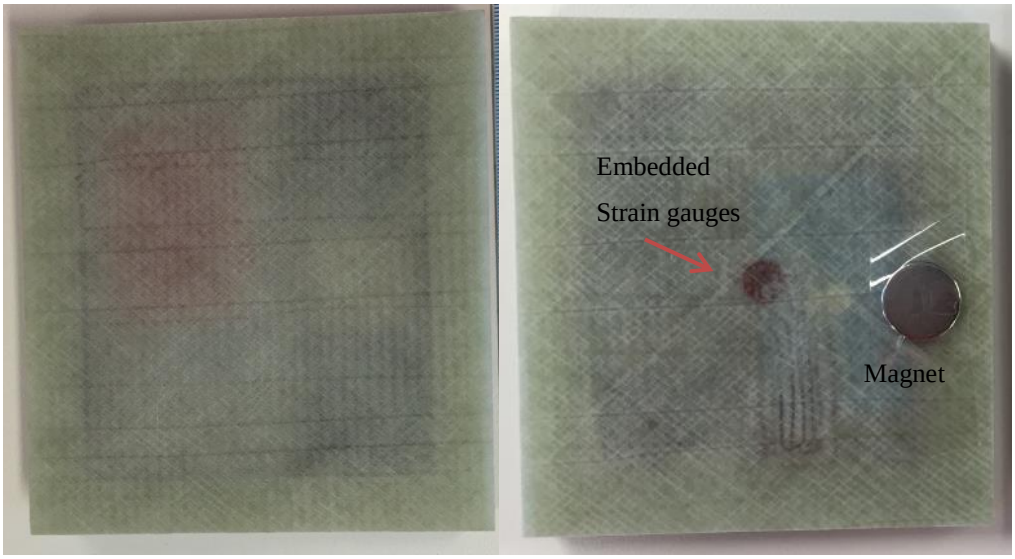

Figure B- 22: Front and rear view of CMP with RF

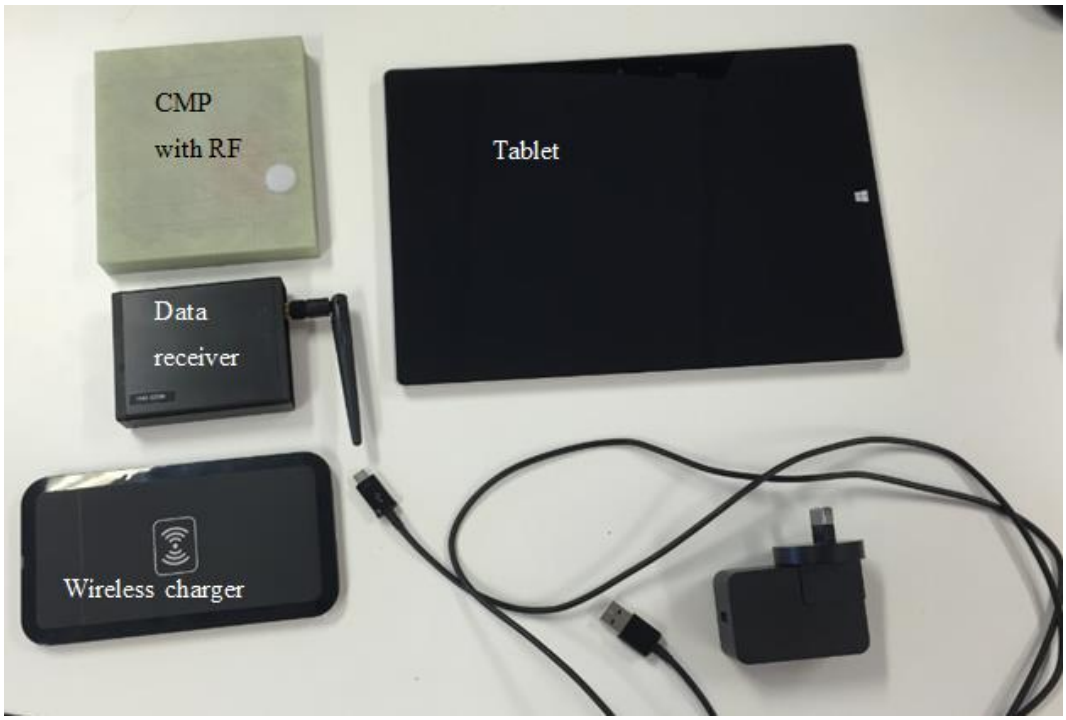

Figure B- 23: The details of CMP parts with RF

The data receiver was connected by a cable to the USB port of the tablet to transfer the transmitted data from the CMP (Figure B-24). Then the CMP would commence operations when a magnet is placed on its surface where the Reed switch was embedded as shown in Figure B-25 and B-26.

Figure B- 24: Data receiver connected to the tablet by a cable through the USB port

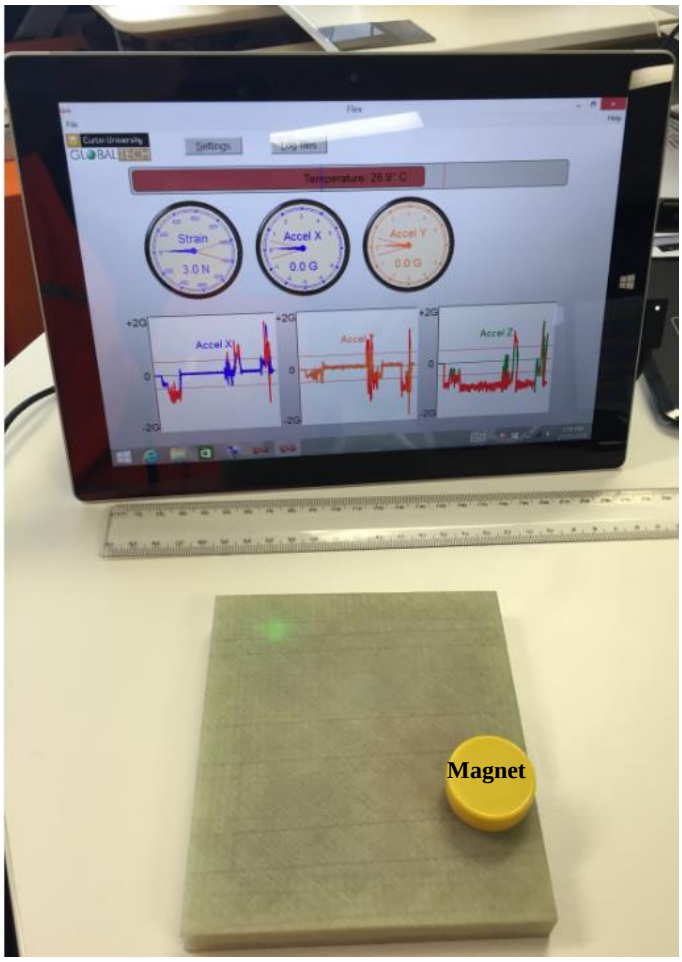

Figure B- 25: The CMP is communicating with the tablet by RF

Figure B- 26: The CMP transmitting data

Figure B-27 shows that when the CMP was placed on the wireless charger the blue LED on the charger lit-up, which indicates the battery and charger were connected.

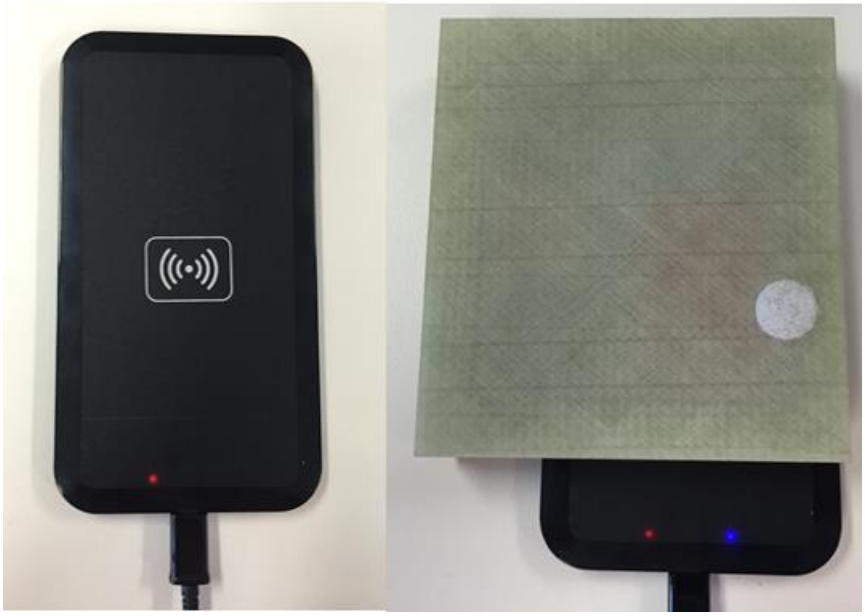

Figure B- 27: Wireless charger is charging the CMP